Risks of Secondary Space Debris Generation from Net Capturing in Active Space Debris Removal Missions

MSc Thesis
Michal Cuadrat-Grzybowski
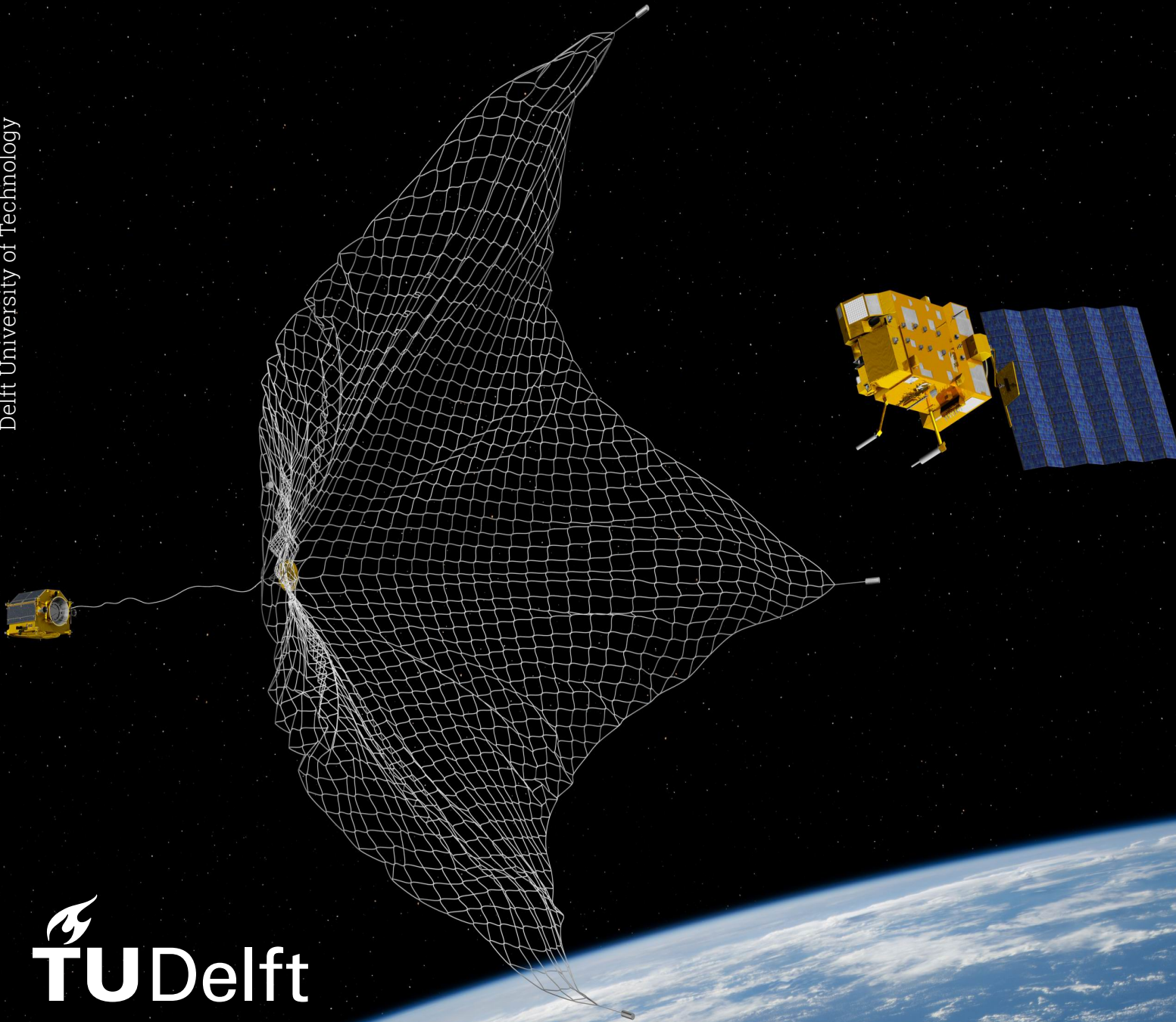
TUDelft

Risks of Secondary Space Debris Generation from Net Capturing in Active Space Debris Removal Missions

by

Michal Cuadrat-Grzybowski

to obtain the degree of Master of Science at the Delft University of Technology,
to be defended publicly on Thursday November 16, 2023 at 13:30.

TU Delft

Acknowledgements

Slightly more than two years after I started my Master's, I can finally see that there is a promising new beginning afterwards. In fact, when I started my Thesis, I unfortunately needed to have surgery which delayed the whole process by about two months. During that time, it was certainly a highly unpleasant experience and I am very happy to see that I lived through it and somehow managed to finalise my Thesis with little delay. This would have surely not been the case without my fiancée Marianna, who I must say has been a rock during during all of those difficult times and actually during my entire five and a half years of study.

First and foremost, I most certainly want to thank my Thesis supervisor Prof. Eberhard Gill, for his invaluable guidance, expertise, and patience during our weekly meetings. Even abroad in the USA, his mentorship and insightful feedback have been instrumental in shaping the quality of this work. Due to the openness of the subject matter and due to my perfectionist nature, I wanted to tackle too many things, which sometimes led me to be lost and confused after finalising major tasks. He was always available to provide much needed guidance, but also calming advice, especially near the end. These weekly meetings were surely an essential part of why my Thesis is finalised and it was always a pleasure to discuss other topics.

It was also through my supervisor's advice, that I met Dr. John-Allan Pascoe, who has helped me with only a few meetings to grasp the complexity of breaking structures. Around the middle of my Thesis, I then had the pleasure to start an informal co-supervision with Dr. Sergio Turteltaub, with whom we delved deep into (dynamic) structural modelling, rigid-body dynamics and a few philosophical/phenomenological conversations on various subjects.

I am also grateful to Martin Kroon and Sjoerd de Bekker, from Airbus Netherlands B.V., who have provided me with lots of essential information, and advice on the Envisat structures and how these could break under net loadings.

Lastly, I would like to thank my family with my three younger siblings and my friend Max for their support, encouragement and much needed fun times, especially when I needed a break from my studies.

I believe that I can say without any doubt, that this thesis does in fact represent the beginning of my academic journey, as I am now looking forward to start my PhD studies. I also think that this work is also a collective and clear effort from many people, other than me. It is thanks to them, that I am truly fortunate and I am certainly more than thankful for the opportunities that this work will open for me later on.

Michal Cuadrat-Grzybowski
Delft, October 2023

Summary

Present and future operational spacecraft have an increasing risk to collide with defunct satellites, which is becoming one of the key problems of today's space domain. Thus, mitigation strategies which eliminate existing debris, such as with Active Space Debris Removal (ASDR) missions, are more important than ever. One of the considered ASDR approaches uses a net as a capturing strategy. This net is deployed from a chaser spacecraft and connected to it by a tether. The benefits of such strategy are to allow for a large capturing distance, high compatibility for different space debris sizes and reduced accuracy requirements. It can be deduced that a key requirement of ASDR missions is that while capturing existing debris, no new space debris is to be generated during the process. However, when simulating net capturing, usually assumptions are made with respect to the physical properties and shape of the defunct objects, neglecting any potential of breaking-off of vulnerable structures, like antennas, solar arrays or other flexible appendages. With an enhanced risk of failure, especially if these are already damaged, these could lead to even more space debris.

Thus, this Thesis assesses what are the **Risks of Secondary Space Debris Generation from Net Capturing in Active Space Debris Removal Missions**. Given the problem statement, several Research Questions (**RQ**) were defined:

RQ1) How can the risks of secondary space debris generation for net capturing ASDR missions be modelled?

> **RQ1.1)** How can secondary space debris generation be defined?
>
> **RQ1.2)** Which simulation scenarios and mission phases are adequate to model secondary space debris generation using net capturing?
>
> **RQ1.3)** What are the main factors which contribute to the risk increase related to the physical and dynamical interactions between the tether-net, chaser and space debris?
>
> **RQ1.4)** What are the relevant results from **RQ1.2** and **RQ1.3** that can be used to characterise the generation of space debris?

RQ2) What preliminary mitigation techniques can be formulated to reduce the risks of secondary space debris generation in ASDR missions using nets?

> **RQ2.1)** How sensitive is the risk model w.r.t. the physical and dynamical properties of the interactions between the tether-net, chaser and space debris?
>
> **RQ2.2)** Which mitigation techniques could be used to reduce the risks?

Given the openness of these questions, this study is performed in the form of a risk investigation. As an initial step to define and identify which risks could occur (**RQ1.1**), the potential of material surface fracture due to impact was preliminarily checked and excluded. Due to the low velocities of net deployment and impact, only risks related to structural breaking of flexible appendages, during capture and towing were found to be the most plausible. Specifically, these are related to the appendages connections and interfaces (due to their lack of resistance and intrinsic design against large stresses). In fact, in a preliminary system analysis, **four** main weak structural locations were identified.

Recognising the aforementioned risks, adequate simulation scenarios were defined for **RQ1.2**. The main case study for this work is ESA's Envisat, a 25 m-long satellite which has been dysfunctional since 2012, selected due to its threat and its multiple flexible appendages, most notably a 10 m-long Advanced Synthetic Aperture Radar (ASAR) antenna, a 2 m-long Ka-band antenna and a 16 m-long solar array. Given this target, a nominal simulation scenario of capture was required as the main focus of

this investigation. A discrete Multi-Spring-Damper (MSD) net model was used to simulate the 20 m/s-deployment of a 30 m x 30 m net onto an Envisat mock-up. Contact dynamics between the net and mock-up were computed using the so-called penalty-based method. The forces and moments, experienced by the satellite as modelled by the method, were then retrieved by post-processing. These were finally fed to two dynamical models, both representative of the Envisat system, assuming, first a single-rigid body, and secondly two rigid bodies connected by a Single-Degree-of-Freedom hinge connection. Lastly, another simulation scenario was then advised to be made related to the towing phase of the mission. For this phase, the net was approximated as a simple Spring-Damper connector with the chaser being a point-mass, and the motion being restricted to be two-dimensional.

First, for the nominal simulation scenario, several dynamic and structural risks had a high likelihood to occur. The independent motion of the spacecraft's solar array, combined with **its large size** and **fragile structure** (10 mm-thick) showed to be detrimental in the capturing process (**RQ1.3**). Excessive torque loadings were computed at two of the solar array identified weak locations which could indicate breaking. These were mainly due to **the propelling bullets**, leading to significant tension forces and thus large contact loads. Additionally, the 2 m-long Ka-band antenna was found to have a high likelihood of structural breaking. This was specifically due to **its length** inducing buckling and **thin connections** creating excessive shear loading at its dish-beam interface. Thus reflecting on **RQ1.4**, structural breaking could occur at the hinge-solar array interface and at the antenna beam-dish interface, leading to the generation of a 5 m x 14.3 m debris and a 0.9 m x 1 m antenna dish, respectively. Furthermore, to answer **RQ1.3** and **RQ1.4**, the towing phase shows also a potential risk. The **chaser mass**, **tether stiffness** and **propulsion force** were found to be critical design parameters that could affect solar array and tether coupling resonance phenomenon. This resonance could lead to significant solar array vibrations, consequently leading to structural breaking at the solar array root.

Secondly, having identified the structural and dynamical risks, three sensitivity analysis were implemented to aid in designing preliminary mitigation measures (**RQ2**). The first mitigation sensitivity analysis focused on the analytic effect of the net deployment characteristics: deployment velocity (V_e) and shooting angle (θ_e), the net contact material properties (α, E_i and ν_i) and space debris rotation rate ω_d. Due to the small ω_d, V_e is found to be the most significant indicator of structural breaking risk. By investigating **RQ2.1** and **RQ2.2**, V_e was found to affect the normal contact force by two to three orders of magnitude. Given this, the structural breaking indicators discussed for **RQ1**, required the impact velocity to be limited to **2.0 m/s**. Furthermore, the numerical sensitivity analysis made on the bullet-mass-to-net ratio (m_b/m_{net}) has found that even though a certain minimum value is required for proper net wrapping around the object, a maximum value must also be set to avoid internal net structural and solar array breaking. These considerations resulted in a net design space as follows:

$$\frac{4\,m_b}{(m_{net} + 4\,m_b)} \cdot V_e \cdot \cos(\theta_e) \leq 2.0 \text{ m/s, for } 0.25 \leq \frac{m_b}{m_{net}} \leq 1.25.$$

From all input parameters, the bullet mass (m_b) and initial deployment lateral deviation ($\Delta x_{CM,0}$) were chosen for the second numerical sensitivity analysis. As for m_b, $\Delta x_{CM,0}$ also greatly affects the risk indicators. Therefore, it was suggested to only capture the Envisat's main body. Last but not least. the final sensitivity study was performed on the simplified towing dynamical model. It was shown that a chaser mass of **850 kg**, a tether stiffness of **3622.7 N/m** and a propulsion force of **440 N** allowed the damping of the detrimental tether-solar array resonance phenomenon.

With secondary space debris being potentially generated, net capturing is found to be riskier than originally thought. This work's **innovation** lies in the literature gaps separated in four main categories. First, this Thesis analysed the effect of the net loads on a satellite with a large solar array two-body dynamics. This is essential to accurately model complex and flexible satellite systems, which in the literature are only modelled as rigid bodies. Secondly, a simple structural analysis was implemented to identify locations of failure. Thirdly, this work was the first in the literature which evaluated if structural

failure occurs due to net capturing. Lastly, these aforementioned considerations are used as the basis for design recommendations for net capturing missions.

Finally, confirm the results of this investigation, it was recommended to first verify the loadings on the Envisat's main body, as small antennae, cables and the thermal blanket were neglected. Furthermore, the MSD net model only assumed tensile stresses. This is not a conservative approach as in reality those stresses would be greater due to lateral loading. Lastly, it was suggested to perform an integrated net-spacecraft dynamic model analysis without sequential modelling. This would also entail the need of performing a numerical structural analysis of stresses in the identified weak locations and a numerical simulation of the possibility of material impact fracture due to impacting bullet interactions with the solar array and the ASAR antenna.

Contents

List of Figures

List of Tables

Nomenclature

Abbreviations

Abbreviation	Definition
ASAR	Advanced Synthetic Aperture Radar
ASDR	Active Space Debris Removal
ANCF	Absolute Nodal Coordinates Formulation
CFRP	Carbon Fiber-Reinforced Polymer
CG or cg	Center of Gravity
CM	Center-of-Mass
ECM	Elastic Continuum Model
EOL	End-of-Life
EoM	Equation of Motion
EMR	Energy-to-mass Ratio
Envisat	ENVIronmental SATellite
FAD	Failure Assessment Diagram
FE	Forward Euler (integrator)
FEM	Finite Element Method
GEO	Geostationary Earth Orbit
GT	General Theme
LEO	Low Earth Orbit
LVLH	Local-Vertical-Local-Horizontal
MDOF	Multiple Degree of Freedom
MEO	Medium Earth Orbit
MMOI	Mass Moment of Inertia
MSD	Mass-spring-damper model
MRB	Multi-rigid-body model
PDM	Primary Deployment Mechanism
PIP	PDM Interface Plate
RK4	Runge-Kutta 4 (integrator)
ROGER	Robotic Geostationary Orbit Restorer
RQ	Thesis Research Question
RT	Technical Risk
SDOF	Single Degree of Freedom
TSR	Tethered Space Robot

Symbols

Symbol	Definition	Unit
a	Crack primary dimension	[m]
a	Orbit semi-major axis	[m]
A	Cross-sectional area	[m^2]
c	Damping coefficient	[N/(m/s)]
d_n	Normal damping coefficient due to impact	[N/(m/s)]
C_V	Wave speed	[m/s]
d	Diameter	[m]
d_p	Deployment distance	[m]
e	Coefficient of restitution	[-]
E	Elastic Young's Modulus	[GPa]
$E\,I$	Flexural Rigidity	[Nm^2]
$\boldsymbol{F}$	Force vector	[N]
$\boldsymbol{F}_{c_i}$	Contact force vector of the ith node	[N]
G	Torsional elastic modulus	[MPa]
h	Altitude	[m]
I_{ii}	Area moment of inertia	[m^4]
$\mathbf{I}_d$	Debris MMOI matrix	[kgm^2]
j	Impulse	[N/s]
J	Mass moment of inertia	[kg m^2]
J_T	Torsional area moment of inertia	[m^4]
K	Stress intensity factor	[-]
K_{IC}	Fracture toughness	[-]
k	Axial stiffness	[N/m]
k_n	Contact stiffness	[N/m]
l_0	Unstretched length	[m]
l_{0_q}	Net mesh size	[m]
L	Length	[m]
m	(Point) mass	[kg]
m_b	Bullet mass	[kg]
n	Material constant	[-]
q_{ij}	Modal coordinates	[-]
r_{ij}	Relative distance between node i and j	[m]
$\boldsymbol{r}$	Absolute position	[m]
R_i	Contact radius	[m]
$\mathbb{R}$	Rotation matrix	n.a.
S	Reference area	[m^2]
t	Time	[s]
$\boldsymbol{T}_{ij}$	Tension force vector between node i and j	[N]
M/M_T	Moment/torque	[Nm]
V	Velocity	[m/s]

Symbol	Definition	Unit
Y	Fracture geometry function	[-]
$\mathcal{B}$	Body-fixed reference frame	n.a.
$\tilde{\mathcal{B}}$	Local beam reference frame	n.a.
$\mathcal{L}$	LVLH reference frame	n.a.
$\mathcal{N}$	Inertial (Earth-centered) reference frame	n.a.
α	Contact material constant	[s/m]
δ	Penetration depth	[m]
$\dot{\delta}$	Penetration depth rate	[m/s]
ϵ	Strain	[-]
η	Flexible appendage deformation	[m]
η_{net}	Net packing initial condition	[-]
η_V	Net body latency ratio	[-]
θ_e	Deployment angle	[deg]
θ_s	Solar panel angle deflection	[rad]
θ_X	Pitch angle	[rad]
θ_Y	Roll angle	[rad]
θ_Z	Yaw angle	[rad]
$\dot{\theta}_X$	Pitch rotation rate	[rad/s]
$\dot{\theta}_Y$	Roll rotation rate	[rad/s]
$\dot{\theta}_Z$	Yaw rotation rate	[rad/s]
κ	Solar array spring stiffness	[Nm/rad]
λ_i	(Non-dimensional) fundamental frequency	[1/s]
μ	Celestial parameter	[m^3/s^2]
μ_k	Coulomb's friction coefficient (dynamic)	[-]
μ_s	Coulomb's friction coefficient (static)	[-]
ν	Poisson's ratio	[-]
ξ	Non-dimensional length	[-]
ρ	Density	[kg/m^3]
σ	Normal stress	[MPa]
τ	Shear stress	[MPa]
ω	Angular frequency	[rad/s]
$\boldsymbol{\omega}_d$	Debris angular velocity	[rad/s]
ω_n	Orbital mean motion	[rad/s]
ζ	Damping ratio	[-]

Introduction

1.1. Space Debris Problem and Relevance

One of the key problems of today's space domain is the increasing risk of impacts of debris objects at hyper-velocities with operational satellites. This is due to the space debris population, which has been increasing nearly at an exponential rate as can be seen in Figure 1.1.
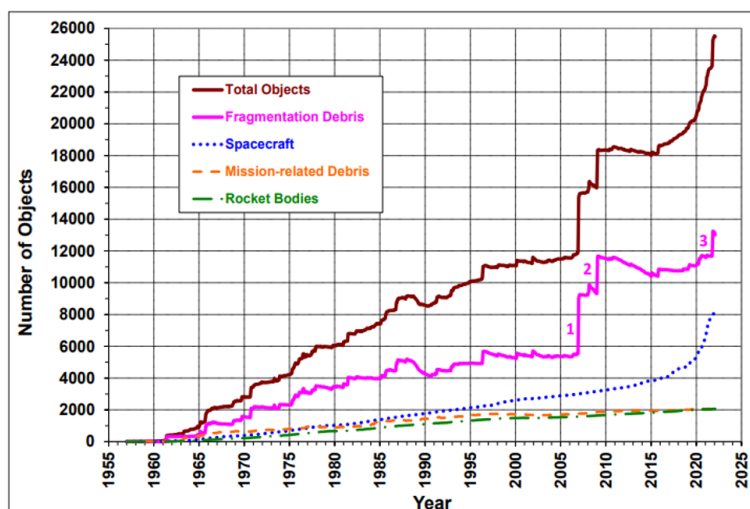
Figure 1.1: Categorised space debris population, from 1955 to 2022, with the abrupt increases due to the Chinese ASAT test in 2007 (1), the Iridium and Cosmos impact in 2009 (2) and another ASAT Russian test done in 2021 (3) [57].

This development was already anticipated by Kessler and Cours-Palais in [42], with the so-called the Kessler syndrome. This is a scenario in which after passing a certain critical mass or number of space debris, a rapidly increasing chain reaction of impact collisions will lead to the destruction of many operational satellites. Most of these satellites are an essential component of today's space infrastructure essential for the present globalised and interdependent world. Furthermore, space exploration, which in the near future could be crucial for humankind survival, will also be endangered. In fact, the creation of several space debris orbital belts will limit the possibility of sending next-generation satellites, spacecraft and probes to low-Earth Orbit (LEO). Added to that, the entire key space infrastructure related to Earth Observation activities, but also the global monitoring of food production, water management and climate, not even counting communication and navigation, are all found to be exposed and in critical danger [79]. Thankfully, the UN, at an international level, and the Federal Communications Commission or FCC, at the USA national level, have both provided their own rules related to how long a satellite/spacecraft can stay in orbit. The UN has proposed a "25 year rule", which ESA follows, rec-

ommending satellites re-entry to the atmosphere after 25 years from the mission's completion [28]. The FCC itself has recently shown to be more strict by limiting this number to 5 years, for all USA-licensed space missions and this rule even applies for other nations which also want to enter the USA space market [96]. Lastly, it has been estimated in [48], that 5 to 10 space debris objects must be removed per year, to stabilise the space debris population increase. The urgency of this ever growing problem is clear and most surely requires future space missions to take responsibility and act accordingly.

With the space debris problem not only being a threat for future space missions and the space infrastructure, it is also a threat on the ability of governing agencies to regulate the orbital space environment. It is thus essential for the increasing space debris population trend to be stopped. The latter can be done through various mitigation techniques and strategies, which have the goal to reduce the creation of additional space debris, when new spacecraft are launched. Other than that, passive removal techniques are also implemented. These take advantage of the space environment, leading to re-entry and burning of the space debris into the atmosphere. However, these cannot be applied to all satellite debris. Active Space Debris Removal methods (ASDR) hold the key to an efficient management and elimination process of the existing space debris population.

1.2. Active Space Debris Removal- A State-of-the-Art Overview

ASDR Missions mainly consist of two major types. The first one is the capturing method and it is to ensure that the debris (target) is properly captured and connected to a chaser spacecraft. These can be classified into: flexible and stiff-connection capturing and electro-dynamic tethers. The second major type is removal methods. These consist on moving the debris from its original orbital path to another one, or to lead to re-entry. Whereas sometimes these are combined together, for e.g. the removal method is implemented after properly capturing the target and then removed, there are removal methods which ensure that no capture is even necessary in the first place. Several removal methods have already been proposed, from using drag-inducing devices (such as inflated balloons, foams or even heat expanding fibers), contact-based slingshot or adhesive removal to even contactless removal methods which limit contact between the chaser and target as well as using lasers or ion beams [74]. The focus of this overview is mainly on capturing methods, specifically focused on the net capturing tool.

1.2.1. Capture-based methods

A capture-based space debris removal mission usually follows several mission phases, from launch and orbital injection of a chaser spacecraft, to rendez-vous with the target, which is then captured and later removed. Within this type of missions, there are various categories, divided by the capturing tool used.

Stiff-connection capturing and removal

Stiff-connection capturing strategies focus on creating a solid or stiff connection between the chaser and the target. This link can be made with one or multiple capturing arms using robotic arm technology, or via tentacles which encircle and close the target in its grip.

Robotic arm technology is similar to the Canadarm2 [55] or DARPA's Orbital express [88]. However, it is difficult to integrate this technology for space debris removal applications. In fact, this integration has been the focus of the DLR in its Deutsche Orbital Servicing Mission (DEOS), the European Proximity Operations Simulator (EPOS), the Front-End Robotics Enabling Near-Term Demonstration (FREND) by DARPA and for two-arm robotic capture there is the UK-based Advanced Tele-robotic Actuation System (ATLAS) [74]. With this type of method, multiple forms of docking connections, called mechanical end-effectors [74], have already been proposed. These range from using probes which enter thermal rocket engines [94] to simple grippers and hand mechanisms [95]. However as this method requires some elaborate form of docking, ensuring that the connection is locked and stiff, a high level of tailoring is needed.

The tentacles capturing method does not require such special docking end-effector, to be tailored

in the same manner as the robotic arm(s) require it. Within this type of stiff capture, the "capturing before touching" strategy is seen to be the safest as it ensures that the debris is first encircled, and then locked, limiting any recoil and thus any problematic de-tumbling issues [74]. Such a strategy has been proposed for the e.Deorbit project in [12] and with the project CADET [20] by Aviospace. Both projects are visualised in Figure 1.2.

(a) CADET visualisation of the tentacles concept [20].

(b) e.Deorbit version of the tentacles concept [12].
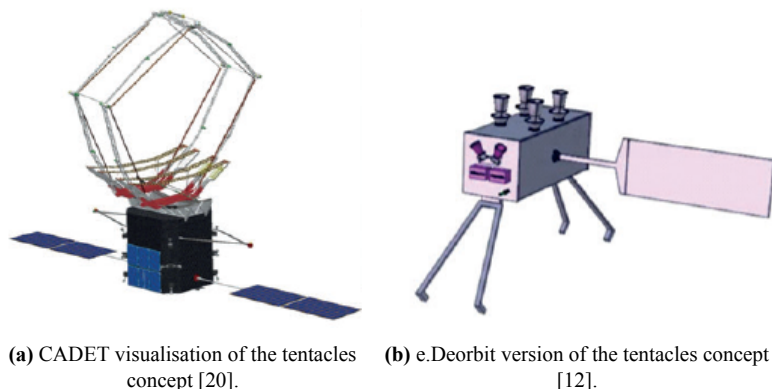
Figure 1.2: Two examples of tentacles-based capturing methods.

Flexible connection capturing and removal

The second type of capturing strategy is based on creating a flexible connection between the chaser and the target. In contrast with the aforementioned type, this method allows to reduce the cost, mass and complexity resulting from the requirement of stiff connection [74]. A flexible point connection can be implemented instead by using a tether-gripper mechanism, a harpoon or even a net.

First, the tether-gripper has been proposed in the Robotic Geostationary Orbit Restorer (ROGER) project [13] (see Figure 1.3a) and by Huang et al. in [39] with the Tethered Space Robot (TSR). This method consists of using an end-effector gripper, similar to the stiff-connections, which is shot at the target. This however lowers the flexibility of the method, as in order to appropriately grip onto the target, a specific part of the debris must be targeted [74]. The latter translates to high accuracy requirements and can also lead to the generation of additional debris in the case of large impact velocities or if the specific part of the target is missed.

Second, the harpoon method consists on deploying a barb-tipped harpoon or bullet onto the target debris and sticking to it through perforation. As it is very simple to test on ground [74], the method has been already proposed by ESA in [63] (see Figure 1.3b). However, due to the need of penetrating the target, micro-fragments of various size are created, which result in secondary space debris and can be detrimental for neighbouring or future satellites.

Finally, the net capturing method consists of sending or deploying a net with four or more weights (called bullets) from the chaser satellite. This net then encircles the target and through simple inertia or thanks to a closing mechanism, fully wraps around it. With the fully wrapped target, the chaser can then de-orbit via the slingshot method or by re-entry into the atmosphere [74]. This method has also been presented in the ESA sponsored ROGER project [13] to retrieve a debris in Geostationary Earth Orbit (GEO) and place it into a higher graveyard orbit. Another ESA sponsored mission, e.Deorbit, as can be seen in Figure 1.3c, the net capturing strategy was thought to be a promising candidate [12]. Lastly, multiple universities, from the Boulder University of Colorado (with the REsearch and Development for the Capture and Removal of Orbital Clutter) [100] to the Politecnico di Milano (with Debris Collecting Net) in Italy [47] have long standing projects in which the main focus is to model, simulate, analyse and validate the dynamic characteristics and the efficiency of the net capturing method.

(a) Tethered-gripper debris removal strategy [13].

(b) e.Deorbit version of the harpoon concept [63].

(c) e.Deorbit version of the net capturing concept [12].
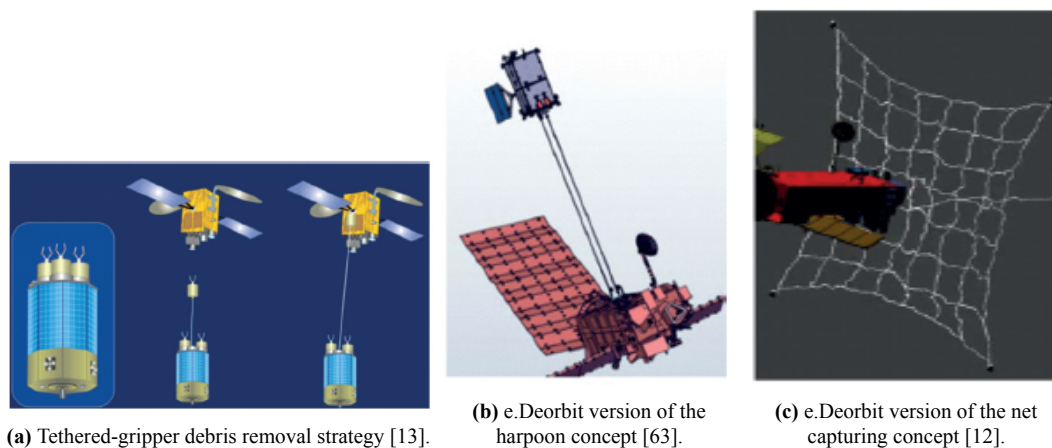
Figure 1.3: Three main types of flexible capturing methods.

Advantages of net capturing

When choosing the type and capturing strategy tool, it is essential to verify that it can be tailored to the space removal mission needs and requirements. In the case of using nets as a capturing strategy, it has been shown to have multiple advantages which can be used in the design process to outweigh its drawbacks [74].

These advantages are as follows: a lowering of positioning and deployment accuracy requirements, allowing for a large capturing distance and an expected high compatibility for different space debris sizes [74, 92]. Furthermore, by avoiding close contact rendez-vous, docking, rigid connections and target penetration with an enhanced risk of collision and structural breaking, the method's flexibility, low mass and cost seems to be the most encouraging type of ASDR strategy.

1.2.2. Net capturing modelling state-of-the-art

An essential part of analysing and evaluating if a method is adequate or feasible for capturing, is its correct modelling and simulation. The net capturing method requires two major types of models for a complete simulation. First, the net internal and deployment dynamics have to be modelled, and the second fundamental part is to correctly simulate the contact dynamics between the net and space debris.

Net deployment modelling

An indispensable goal when modelling the net dynamics, is to find the most optimal net model which shows good accuracy and is not computationally expensive. Various different models have been thoroughly presented and analysed in the literature [68]. These are the Multi-Spring-Damper Model (MSD) (also called lumped-mass model) developed in [10, 69], a net discretisation cubic B-spline model [32], the Absolute Nodal Coordinate Formulation (ANCF) described in [50, 68], an elastic structural/continuum model (ECM) [51] and the Multi-Rigid Body model (MRB) [92]. Several of these relevant concepts are visualised in Figure 1.4.

First, with regards to the cubic-B spline method proposed in [32], a fishing net has been discretised with more than 3 million point nodes (as can be seen in Figure 1.4d). This very high number is needed to accurately model the net's bridle, surface smoothness and continuity [68]. Due to the complexity and computational expensiveness of this discretisation, this model has mostly been used in marine fishery applications and rarely for ASDR.

The second modelling strategy is related is the discretisation of the net threads as solid or rigid bodies in MRB modelling [92] (see Figure 1.4c). However, this model lacks elasticity implementation which is an essential aspect of the dynamic behaviour of nets [68].

The third ECM net modelling method has been described in [51]. In contrast with the aforementioned MRB model, it allows the adequate modelling of large elastic displacements. The model has

already been applied to elastic orbital tethered systems [51] and has been validated for large displacements in [45]. However, due to the high complexity of the system equations and the low computational efficiency, the model can be seen to have too many disadvantages compared to other more recently improved methods [68].

Lastly, both the ANCF (Figure 1.4b) and lumped mass MSD (Figure 1.4a) models have been the most widely used in ASDR net dynamic studies [10, 68, 15, 76]. The ANCF-based model, first proposed by Liu et al. [50], then further analysed, characterised and validated by Shan et al. [76], consists of computing the absolute positions with their position gradients resulting in a elastic-flexible description of net thread elements. Furthermore, it is mainly used for high precision net tracking. The MSD model discretises the net into point masses which are all linked by linear-elastic spring-damper connectors. Whereas the ANCF is the most precise and realistic model, it is computationally expensive [68]. It was concluded in [68], that even though the MSD model showed a slightly larger difference compared to the ANCF-based model, it was still validated with a parabolic net deployment experiment (with an average relative error below 15%) and seemed to be more efficient as it was found to be 15 times faster than the ANCF model [68].

(a) Advanced net lumped mass modelling [68].

(b) ANCF net modelling [68, 76].

(c) Multi-Rigid Body net modelling concept [92].

(d) Fishing net modelled with the cubic B-splines [32].
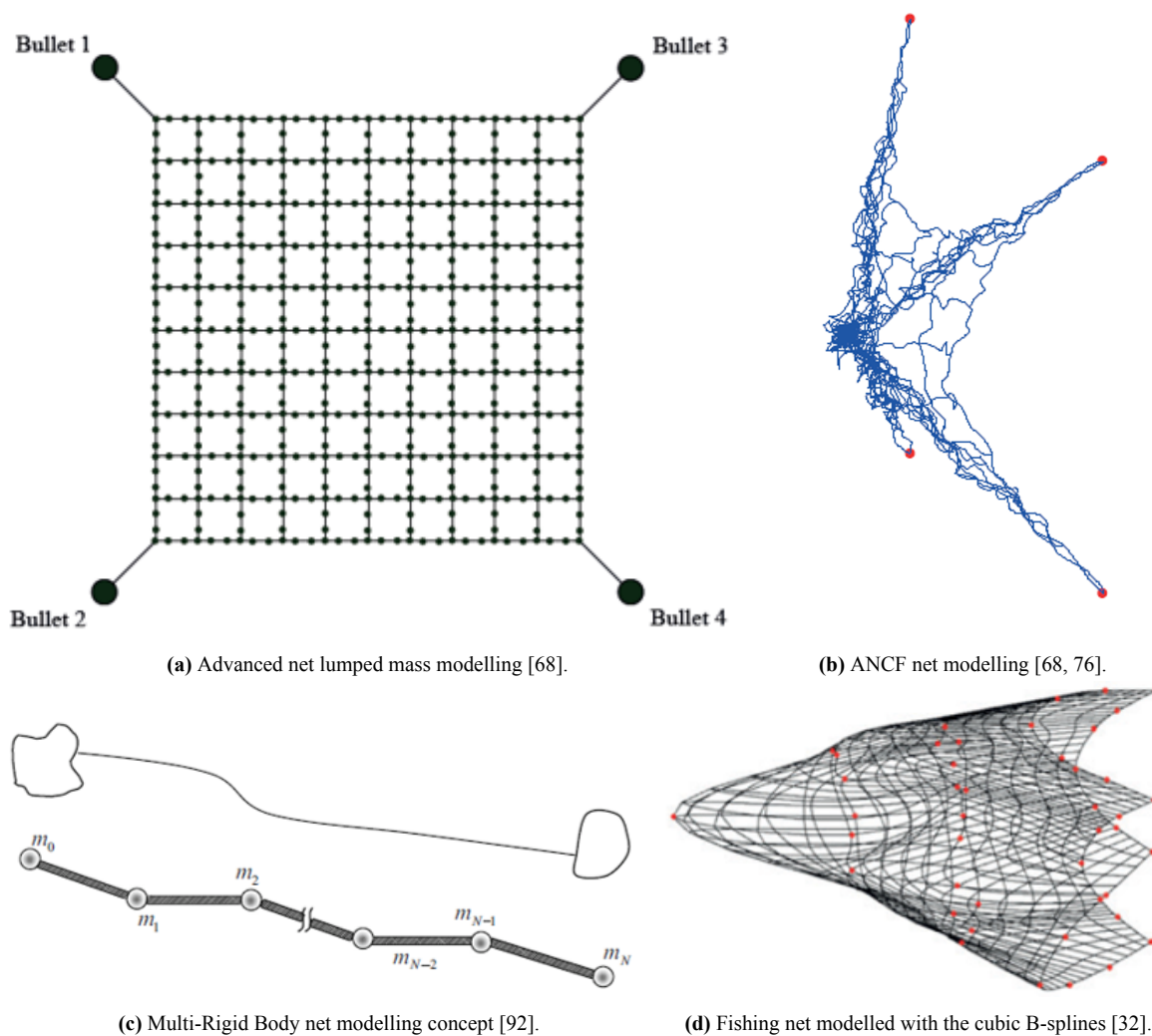
Figure 1.4: Four net modelling methods.

Net-target contact modelling

The second most important step in net capturing simulations is to accurately and efficiently model the contact between the net and its target. Recently, two major methods for net contact dynamics modelling

have been prominent in the literature [10, 15, 68]. The Penalty-Based Method, which results in a response force, and the Impulse-Base Method which computes the impulse.

The first method focuses on computing a time-continuous force which results from the penetration of one object w.r.t the other. All force-contact based methods have been thoroughly described in [33]. The net's discretised point masses are assumed to be small spheres with radii similar to the net cable elements [10]. Contact between the target and the net is thus an accumulation of N impact penetrations between net spherical nodes and the target wall, using Hertzian elastic theory. The penalty method computes the virtual penetration of one object w.r.t the other and feeds it directly into a force model. From the literature, the focus of using the linear damping model [8, 10, 69] has shifted to using a non-linear damping contact force model [16, 71], which better describes the real behaviour of normal contact forces and energy dissipation [33]. However, as it was found in [68], this method is highly sensitive to the contact stiffness and penetration values. The second method, which was first fully described and applied by Shan Minghe [68], avoids the need to define such parameters (which must be obtained through experimentation and highly vary depending on material and shape properties) and focuses on impulse and kinematic relations. Therefore, the impulse-based method computes the contact impulse, which is then fed to the linear and angular velocities of the net nodes and target dynamics.

1.2.3. An essential requirement lacking in the literature
What can be observed throughout the literature is that an essential and key aspect of these ASDR missions which is also a crucial requirement, is lacking. During the capturing and removal of the debris, no additional space debris should be generated. However, as found in the literature when simulating net deployment and capturing, too often unrealistically simplified assumptions are made with respect to the space debris. These range from the physical properties and shape of the defunct objects, to its material and structural properties of its integrated structures.

It is actually common to neglect vulnerable structures, like antennas, solar arrays or other exposed instruments, and assume that they are indestructible (part of the rigid-body assumption). When analysing such elements, there is an enhanced risk of critical breaking or structural failure, especially if these are already weakened by existing damage. Given this possibility of breaking, there is an undermined risk, that ASDR missions could contribute to even more space debris.

1.3. Research Objective
From the overview of existing literature, several gaps in the body of knwoledge were clearly identified and characterised. Due to the importance of actively eliminating space debris, whilst not creating more, a research objective has been formulated. Thus, the objective of this Thesis is:

To predict if secondary space debris could be generated during net capturing by numerically modelling the dynamics and material response of the debris during the capturing and towing phase of the Active Space Debris Removal mission.

1.4. Research Questions
Considering the specific gaps in the knowledge present in the literature, the relevance of this problem statement and the aforementioned objective of this Thesis, several Research Questions (**RQ**) are formulated.

These are listed below with their associated sub-questions:

RQ1) How can the risks of secondary space debris generation for net capturing ASDR missions be modelled?

    RQ1.1) How can secondary space debris generation be defined?

    RQ1.2) Which simulation scenarios and mission phases are adequate to model secondary space debris generation using net capturing?

RQ1.3) What are the main factors which contribute to the risk increase related to the physical and dynamical interactions between the tether-net, chaser and space debris?

RQ1.4) What are the relevant results from **RQ1.2** and **RQ1.3** that can be used to characterise the generation of space debris?

RQ2) What preliminary mitigation techniques can be formulated to reduce the risks of secondary space debris generation in ASDR missions using nets?

RQ2.1) How sensitive is the risk model w.r.t. the physical and dynamical properties of the interactions between the tether-net, chaser and space debris?

RQ2.2) Which mitigation techniques could be used to reduce the risks?

Therefore, the first part of this study, associated to **RQ1**, focuses on defining secondary space debris generation and creating simulation scenarios which can be used as a basis for a numerical simulation. With these two aspects given, the net dynamics and spacecraft interactions will be analysed both in a nominal simulation and secondly in a sensitivity analysis. Specific factors and failure risk indicators should also be found. These must then be described and verified, in the case that secondary space debris is an actual possibility.

Later, as a response to **RQ2**, this study wishes to show the sensitivity of the proposed numerical simulation models and the aforementioned risks. From this sensitivity study, further information can be obtained and used to see how to mitigate these risks.

1.5. Thesis Outline

Given the Research Questions presented above, it is now essential to mention how these will be answered and discussed. From a first reading, it could be suggested to perform a basic experimental set-up in which a physical net is deployed and impacts a dummy spacecraft model. With the latter, one could try to identify multiple aspects related to the structure experienced stresses and perform a structural analysis. This however would be limited by the premise itself, in which the dummy design (size, shape and material) would dominate the work of this Thesis resulting still in unrealistic and too specific conclusions. These would in fact not be particularly helpful to have a larger overview of the aforementioned problem.

In this Thesis, it is decided to focus both on the spacecraft dynamics caused by the net capturing process and on simple analytical structural models which would seem to verify if, in fact, the structures would break under those loading scenarios.

The Thesis will therefore be structured in the following manner. First, the Mission and Simulation Scenario will be presented in Chapter 2, followed by a general overview of the modelling strategy in Chapter 3. The presentation of the different dynamical and structural models will follow, first with the net dynamics in Chapter 4, secondly the contact dynamics Chapter 5 and thirdly the spacecraft dynamics in Chapter 6. These will then be investigated for their potential risks in Chapter 7. A secondary investigatory study based on a sensitivity analysis can be found in Chapter 8. Lastly, a tertiary study related to the towing phase dynamics and mitigation strategy can be found in Appendix C. Before presenting any conclusive remarks on the subject of this Thesis, the models can be found to be verified and validated in Chapter 9, with the conclusions and future recommendations made in Chapter 10.

2

Mission and Simulation Scenarios

2.1. General Mission Definitions

The different actors or systems involved in a net capturing ASDR mission are the following:

1. **Target** spacecraft: this refers to any space debris object ranging from an entire satellite and upper-stage rocket body to parts of a satellite or rocket (for e.g. solar panels, antennas and others).
2. **Chaser** spacecraft: this is the spacecraft, able to reach the target debris, eject the net, capture the debris and facilitate its removal (by towing or storage).
3. **Tether-Net**: this refers to the capturing tool and its connection (tether) to the chaser.

Given these definitions, a general representation of a net capturing scenario of a satellite-like debris can be seen represented in Figure 2.1.
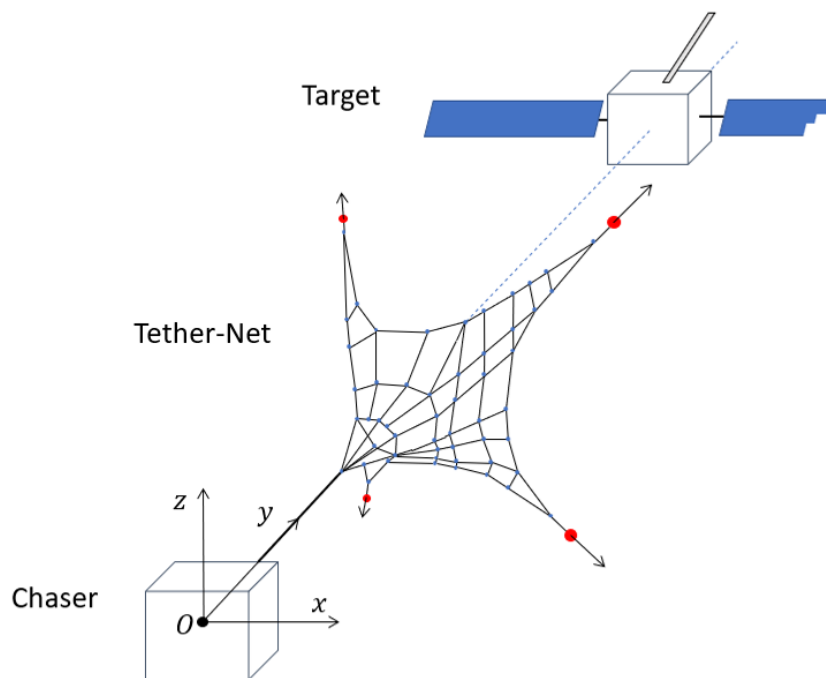
Figure 2.1: Generic mission representation with coordinate system origin O (chaser), target space debris, $y-$direction representing the direction of flight, the radial coordinate as $x-$direction and the $z-$direction completes the frame. The red dots represent the bullets of the net.

2.2. Mission Phases

Any net capturing ASDR mission can be divided into the following mission phases [19]:

1. Pre-orbital activities and Orbital Phasing
2. Rendez-vous (with orbital corrections)
3. Net deployment
4. Impact and Momentum Transfer
5. Net wrapping and closing
6. De-Tumbling
7. Towing
8. Re-entry or Debris storage.

In this Thesis, only phases 3 to 7 will be discussed in order to reduce the scope of the study. With this, it is assumed that phases 1 and 2 are completed successfully and do not result in any uncertainties which could propagate into the subsequent phases. Lastly, due to the complexity of the re-entry aerodynamics and spacecraft disintegration characterisation, phase 8 is also omitted. This is also justified by the fact that any secondary space debris would be directly disintegrated or safely stored during the process. Hence, it is assumed that any potential risks of creating additional orbiting debris is minimal and thus phase 8 can be ignored.

2.3. Secondary Space Debris Generation

Secondary space debris should first be clearly defined and secondly, its sources should be classified.

2.3.1. Defining debris generation

As a preliminary understanding, the generation of secondary space debris is understood as the breaking of flexible appendages of the target, the connecting tether, the capturing net, or even the chaser. The ejecta from target-debris collisions are also considered as secondary space debris. Furthermore, any unsuccessful capture caused by a miss or slipping of the target from the net would have a high future potential of causing secondary space debris due to their associated uncertainty. However, in this study, secondary space debris generation is limited to structural failure and break-off.

2.3.2. Identifying sources of Risk

Given this definition, the various causes and origins need to be investigated. A discovery tree in Figure 2.2 presents the various risks of generating additional debris, separated in two categories, the first is the space debris object, and the second, is the net-tether denoted by SCD and NET, respectively.

The space debris object is seen to have many potential risks, such as propellant sloshing-based explosion (SCD-FUEL), appendage breaking (SCD-APP), surface fragmentation (SCD-SUR) with the inclusion of already existing damage (SCD-DAM) increasing the likelihood of these events to happen. On the other hand, the tether-net related events are more limited to tensile (NET-TEN) or friction failure (NET-FRI). These mostly occur if the maximum tensile force is reached or in the case of small to large surface discontinuities, these could lead to net deterioration and facilitate tensile breaking. Collisions (COLL) between the chaser and target could also occur, both due to the net and space debris object dynamics, leading to partial/total fracture. Within the appendage category, the different types of loadings are also identified, from torsion (TOR), bending (BEN), shear (SHE) to structural vibrations (VIB).

Lastly, all these risks can also be categorised by the means of how these can occur. In fact, propellant sloshing, appendage and net breaking are the result of the overall capture dynamics and structural characteristics, whereas total or partial fragmentation is only a function of initial impact conditions and material characteristics. Pre-existing damage follows as an intermediary category as it affects both the dynamical aspect of capture and the potential of structures to break due a solid impact. Within this Thesis, all these considerations will be evaluated based on their likelihood and consequence.
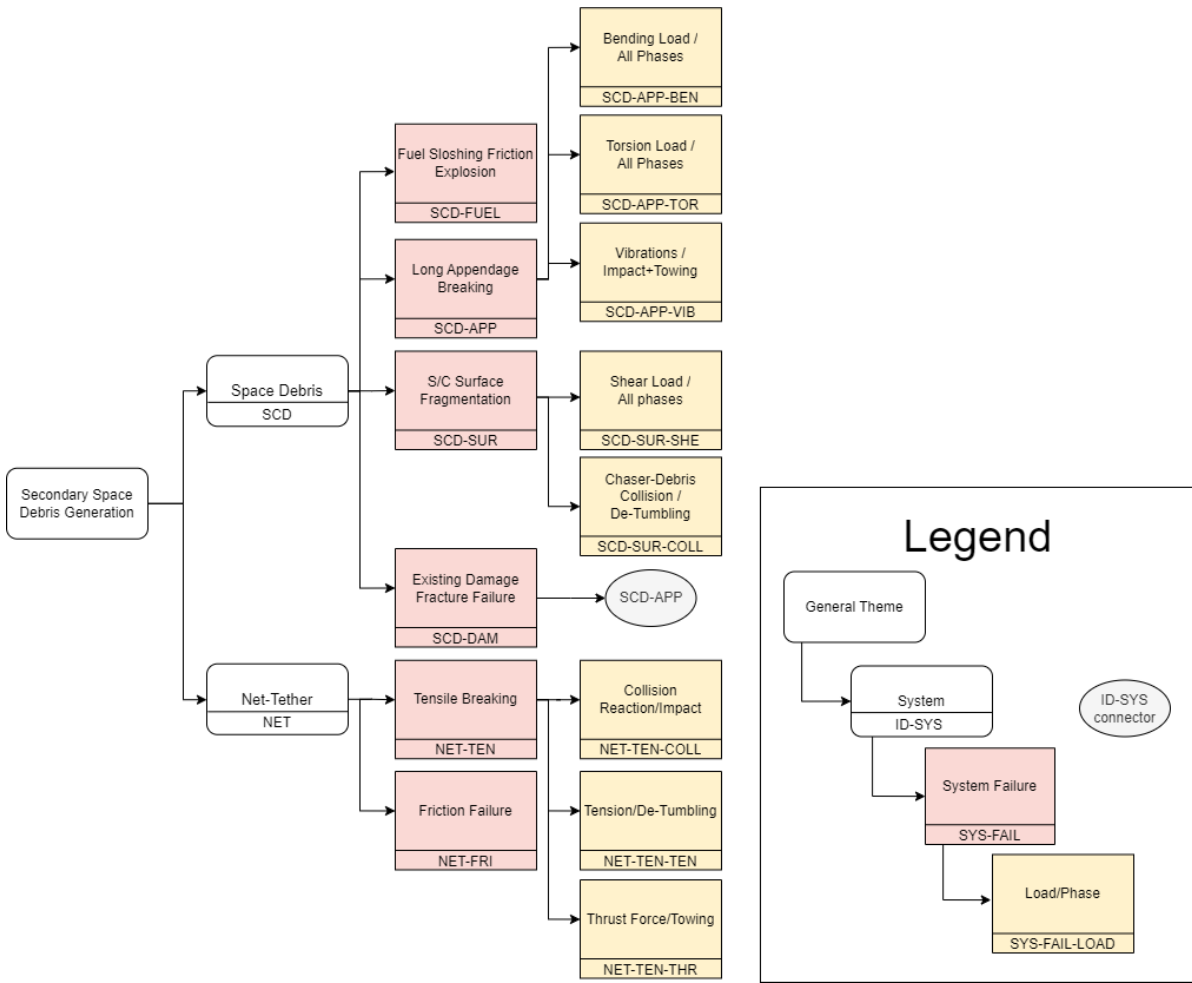
Figure 2.2: Risk Discovery Tree Diagram for the space debris object (SCD) and net-tether (NET), with sub-categories related to failure (FAIL) and the load (LOAD).

2.4. Main Systems Characteristics

2.4.1. Net-tether physical characteristics

Throughout all the different potential materials that could be used for a net, Kevlar is typically chosen from the other potential candidates being Dyneema, Zylon and Vectran [74]. Being simultaneously strong, tough and light, it has been shown to be able to carry 1000 kg without any failure with a 1 mm-tether [8]. In this Thesis, the net material will thus be assumed to be Kevlar. The relevant properties of Kevlar can be found in Table 2.1.

Table 2.1: Kevlar material properties [15]

Property	Symbol [unit]	Value
Ultimate Strength	σ_{ult} [GPa]	2.8
Elastic Tensile Modulus	E [GPa]	70
Maximum elongation	ϵ_{max} [%]	4.0
Density	ρ_{net} [kg/m^3]	1440

The main body of the net is chosen to be of a square shape as it has been found to be the most efficient for mass and capture efficiency [74]. Four outer bullets are then connected to the main body

to provide the necessary forward momentum for deployment and wrapping around the target. As a rule of thumb, the total mass of the bullets must be chosen to be higher than the net's mass [7], such that the net is stable enough for the capture process.

2.4.2. Targets

Two LEO-target spacecraft will be presented in this section, one used as this study main focus, with the second used for verification. Given, the high risk that ESA's Envisat presents, it is decided that the latter will be the basis of this study, whilst the Jason series satellites will be used for verification.

Envisat

This Thesis focuses mainly on the net capturing process of the Envisat (ENVIronmental SATellite), which is a deactivated Earth-observing satellite, launched in 2002 by the ESA (European Space Agency). Due to unexpected loss of contact, the mission officially ended in 2012.

This inoperative satellite, which is currently in a polar LEO at an altitude of 772 km, is considered as one of the highest hazards of collision risk. This is due to its mass-to-area ratio, as its orbital path will require 150 years to completely decay [66]. With a large EOL mass of 7892 kg and size of $26 \times 10 \times 5$ m, this large-sized satellite could start a hazardous chain reaction (Kessler syndrome) if it collides with an object of only 10 kg [34]. The satellite has three main characteristic appendages: a large 14.3 m-long solar array (of 338 kg), a 10 m-long ASAR (Advanced Synthetic Aperture Radar) antenna and lastly a 2 m-long Ka-band antenna of approximately 10 kg, as visualised in Figure 2.3. All of these have a potential to break during the net capturing process, especially due to the high uncertainty in their precise structural health status.
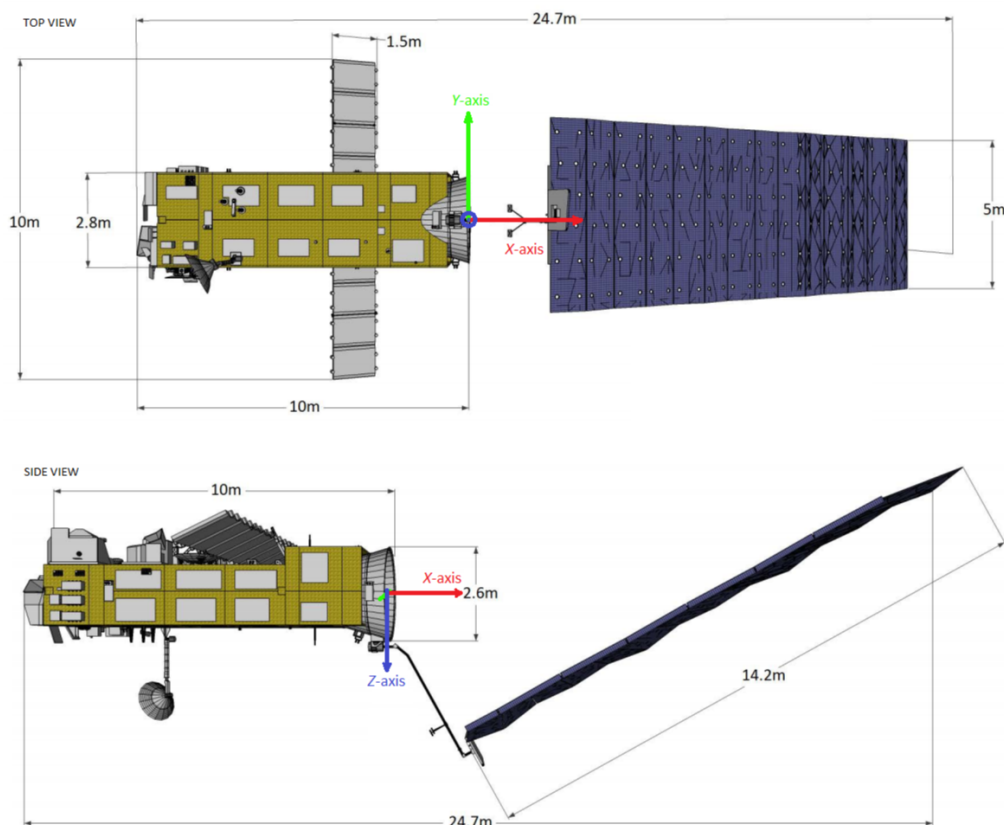
Figure 2.3: Top and side view of Envisat, with associated body-fixed reference frame (ESA) [11, 25]

Jason satellites

Spacecraft from the Jason series are satellites which are in high LEO, at an altitude of 1336 km and inclination of 66 degrees [61]. These have been the first successful missions after the TOPEX/Poseidon mission in terms of measuring the ocean surface topography. In this study, they are chosen due to the fact that Jason-1 and Jason-2 have been deactivated in 2013 and 2019, respectively, and are still in orbit, with Jason-3 (with the same shape and layout as Jason-2) having its End-of-Life (EOL) planned around 2024. Furthermore, they constitute optimal targets, due to their generic shapes and their presence in high LEO.

The spacecraft dimensions are approximately $1 \times 2 \times 3.7$ m when the solar panels are undeployed, with a total wet mass of 600 kg [61], making them medium-sized satellites. The solar panels are composed of four elementary panels of 0.8×1.5 m and a yoke of approximately 0.85 m [61]. The Jason-2 spacecraft can be seen in Figure 2.4, with its simplified mock-up model in Figure 2.5.

Figure 2.4: Jason-2 spacecraft in orbit [NASA].
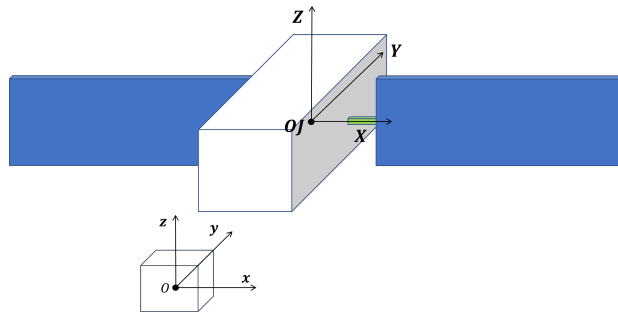
Figure 2.5: Jason spacecraft equivalent mock-up model with body-fixed reference frame.

Choosing the main case study

Last but not least, it is essential to mention that Envisat shows a much higher risk as a colliding body compared to the Jason satellites. This is due to the fact that the Envisat is in a much lower and more crowded orbit. Additionally, its large size makes it a higher hazard of collision with other satellites and space debris, hence increasing the probability of initiating Kessler's chain reaction. Due to the higher urgency to capture the Envisat, this Thesis study will focus mainly on the latter and uses the Jason satellites as a verification tool for the net capturing process. The classical satellite shape of a Jason spacecraft means that the capacity to capture it can be transferred to any other satellite with a similar layout, making it the optimal candidate for a net dynamics model verification study.

2.5. Target Structures

This section presents a brief description of the three flexible appendages of the Envisat spacecraft.

2.5.1. Ka-band antenna

First, this study will investigate briefly the characteristics of the Ka-band antenna. Being the shortest appendage of the Envisat spacecraft, the Ka-band antenna can be visualised in Figure 2.6 and Figure 2.7 with its approximate dimensions summarised in Table 2.2.

Lastly, it should be noted that the antenna has a total mass of 13 kg and the boom is connected to a pointing mechanism, placed at the root of the beam, which drives the boom to its deployed position and locks it, for a pointing accuracy of 0.070 deg [67]. The primary and secondary materials of this pointing mechanism are Ti6A14V (titanium alloy) and the aluminum alloy 7075 [67].
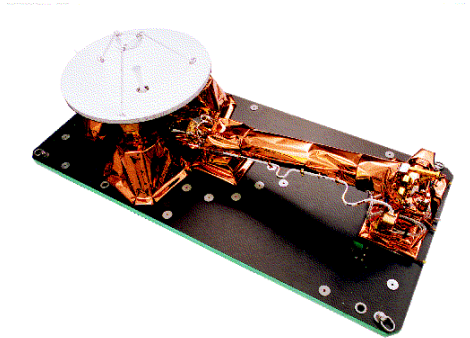
Figure 2.6: Ka-band Envisat antenna (ESA). [52]
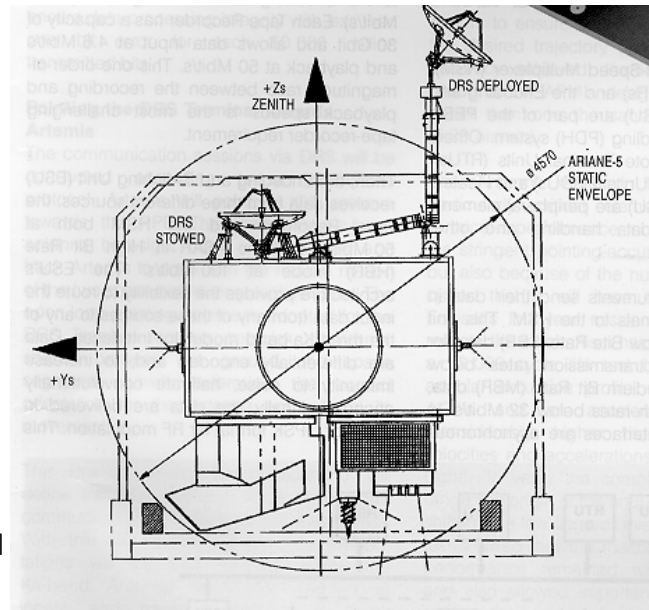
Figure 2.7: Technical drawing of Ka-band Envisat antenna within the Ariane 5 rocket static envelope (ESA). [52]

Table 2.2: Ka-band antenna dimensions.

Characteristic dimension	Symbol	Value
Antenna dish diameter	d_{Ka}	0.90 m
Boom length	l_b	1.97 m
Boom max. and min. diameter	$(d_b)_{max}$ & $(d_b)_{min}$	0.146 m & 0.0486 m

2.5.2. ASAR antenna

The second structure is the 10 m-long ASAR antenna placed on the main body which can be seen both in Figure 2.8 and Figure 2.9. This is the largest of the 10 instruments on board (see Figure 2.9) and had, at the time, highly advanced capabilities to cover large areas of oceans, land and icy terrain [24].
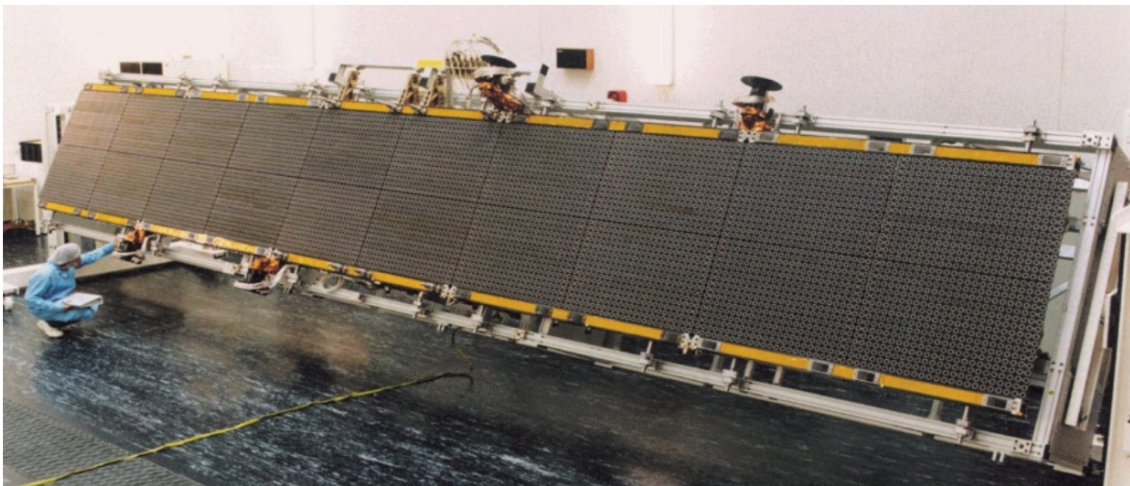
Figure 2.8: ASAR antenna flight model from Matra Marconi Space, UK. [24]
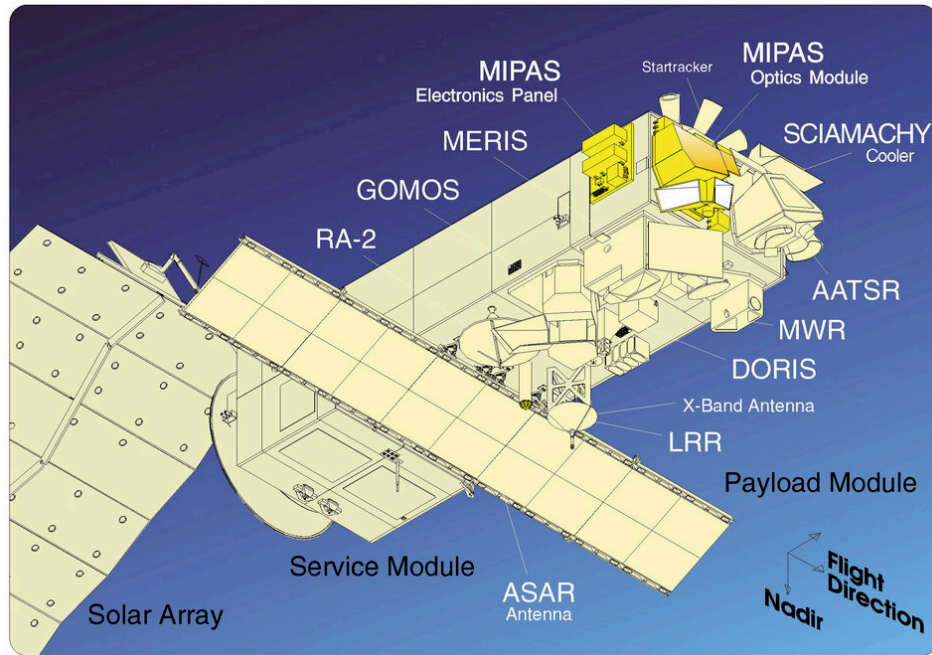
Figure 2.9: ASAR antenna location on the Envisat with other instruments (ESA). [3]

The structure itself is separated into five rigid frames made out of CFRP (Carbon Fibre Reinforced Polymer) and connected in parallel with two Radio-Frequency distribution networks [24]. The ASAR is inclined w.r.t the main body by an angle of 26.19 deg. The dimensions of the entire structure can be found summarised in Table 2.3.

Table 2.3: ASAR antenna dimensions [3].

Characteristic dimension	Symbol	Value
Length	L_{ASAR}	10 m
Width	w_{ASAR}	1.5 m
Approx. thickness	t_{ASAR}	0.156 m

2.5.3. Solar array

The last and most prominent feature of the Envisat is its 14.3 m-long solar array, connected to a 3.1 m-long yoke as seen in Figure 2.3. In terms of the solar array platform itself, it is composed of 14 rigidly connected panels of size $1 \text{ m} \times 5 \text{ m}$. Furthermore, the solar array is attached rigidly to a beam used for deployment with a PDM (Primary Deployment Mechanism) as can be observed from Figure 2.10. The solar array is also connected to the yoke beam via the PDM Interface Plate (PIP), which contains two of the most important hinges for the Envisat deployment phase. The PIP is hence the primary interface between the secondary hinge, connected to the solar array yoke, and the 10-mm thick panel.

(a) Supportive beam under the solar array [27].   **(b)** Fully deployed solar array [26].

Figure 2.10: Envisat solar array and deployment beam. (courtesy of Airbus Netherlands B.V.)

In order to fully characterise this large structure, the deployment sequence Figure 2.11, can be used to identify its main elements. From Figure 2.11, the solar array deployment yoke has three main hinges which are located at the yoke root and the two other near the solar array PIP. As these have not been designed for strength but only for stiffness, these hinges constitute potential locations of failure during the capturing process.
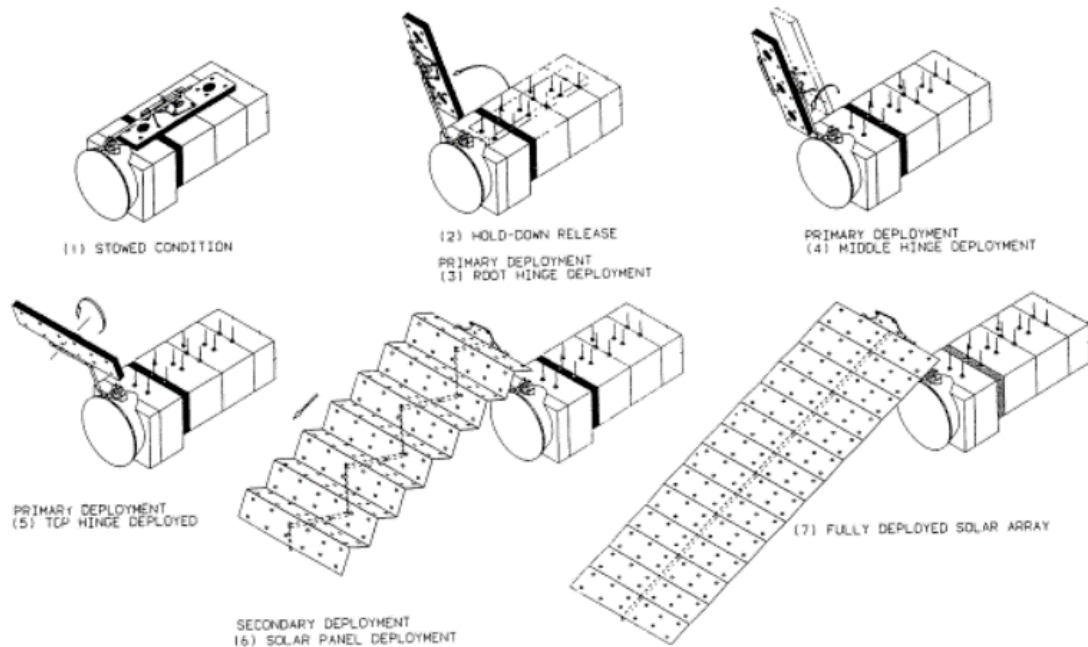
Figure 2.11: Envisat solar array deployment sequence. [101]

Furthermore, the PIP is a 50 mm-thick honeycomb structure which connects the yoke to the solar array and can be seen at the far right of Figure 2.10b. Its skins are made of CFRP and a small beam

spans the three hinge connections. Due to its size and thickness, this interface is a structurally weak location and thus it is seen as a potential sight of failure during the capturing process.

Finally, the entire solar array system stiffness needs to be presented. These vibrational properties have been obtained during a vibration qualification tests, in which Zwanenburg [101] has found two main vibrational modes with frequencies of 0.05 and 0.06 Hz.

2.6. Preliminary Evaluation of Impact Fracture Risk
This section makes a preliminary assessment of the fragmentation and critical perforation risks.

2.6.1. Catastrophic fracture condition
A potential risk that could be caused by net capturing is that the net knots or/and bullets could potentially break themselves or break parts of the space debris at impact. A rough order approximation of the collision risk of breaking can be done using the Energy-to-Mass Ratio (EMR) [21]:

$$EMR = \frac{\frac{1}{2}m_p V_p^2}{m_t},\tag{2.1}$$

where m_p and m_t are the projectile and target masses and V_p is the relative impact velocity. According to the standard model, if $EMR > 40$ J/g, a total fragmentation or catastrophic event will happen. IMPACT, another impact model [21], refers to a value of 10 J/g, as a transition between highly energetic and low energetic impacts. Assuming the lower estimate, the model then predicts a catastrophic event in which larger fragments are created. Below these two thresholds, only cratering or partial break-up events can occur. To verify the latter values, simple ballistic theory will be used. The ballistic impact velocity for breaking to occur is adapted from [90] to include a non-zero post-impact velocity as:

$$(V_p)_{lim} = \sqrt{\frac{2\pi r_p^2 \sigma_t t_w}{(1 - a_V^2)m_p}},\tag{2.2}$$

where r_p is the projectile radius, σ_t is a measure of the target's structural strength, t_w is the target wall thickness and a_V is an additional factor assuming that the end velocity is a factor a_V of the initial impact velocity ($(V_p)_f = a_V (V_p)_0$). Interestingly, by combining Equation 2.2 to Equation 2.1, the projectile mass seems to not have an effect on the failure EMR threshold. Thus, from this simple analysis, it could be understood that the threshold of EMR for a catastrophic event to occur, is mainly a function of the target geometry (t_w), material strength (σ_t) properties and total mass (m_t), and the impactor characteristic size (r_p).

Therefore, for a catastrophic event, $a_V \sim [0-0.5]$, and by assuming an average target mass $m_t \sim$ 1720 kg [38], $r_p \sim 10$ cm, $t_w \sim [0.1, 10]$ cm and $\sigma_t \sim 10^9$ Pa, an average $\overline{EMR}$ in the range $18 - 2435$ J/g is obtained by applying Equation 2.2. This computed range contains the nominal values of 10 J/g and 40 J/g and is in agreement with [62].

Thus, a first order analysis considers the following input ranges: the impact mass m_p is referred here as the mass of the net bullets $m_b = [0.5 - 4]$ kg (associated net mass: $m_{net} = [2.0 - 14]$ kg), impact velocities $V_p = [0.5 - 50]$ m/s and $m_t = [0.1 - 8000]$ kg. A summarising plot of differently sized satellites (represented by coloured regions) and catastrophic events curves for the Envisat system a function of impact velocity and bullet mass can be found in Figure 2.12.
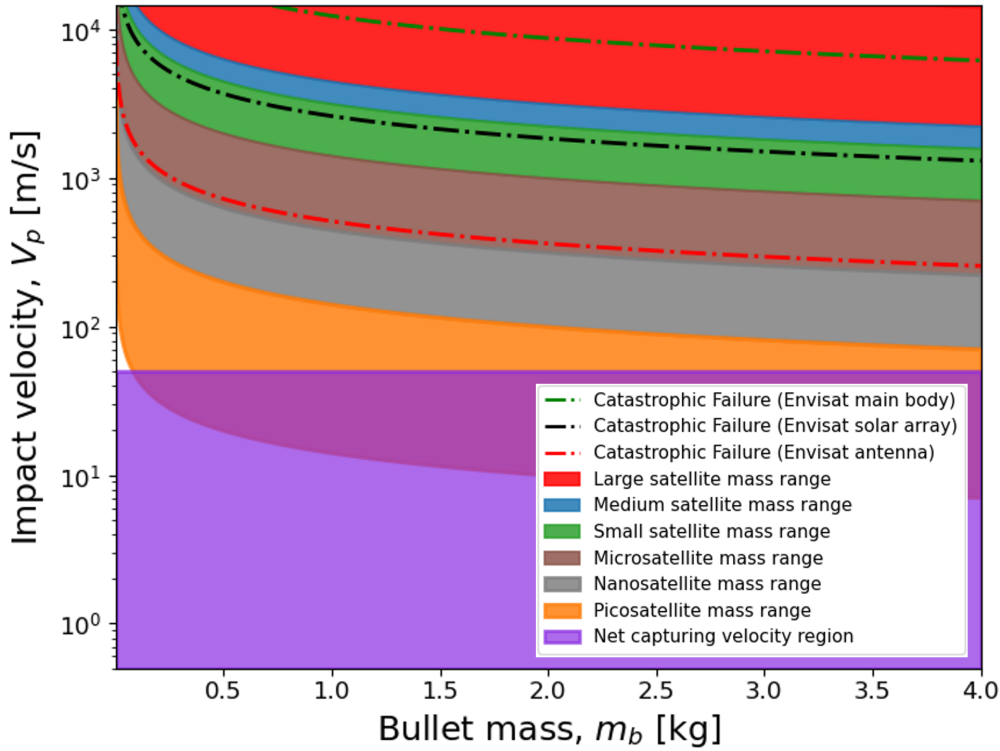
Figure 2.12: Energetic impact analysis: catastrophic event regions for different satellite masses with sub-system inclusion of the Envisat satellite.

From Figure 2.12, one can see that the risk of total fragmentation with net capturing is a possibility only to nano-satellite targets in the case of high velocities (50 m/s). Additionally, using the example of the Envisat, one can observe that whereas it is considered to be a large satellite (above 1000 kg), its sub-elements behave in the same manner as lower satellite categories. This means that when analysing satellite impacts, it is recommended to evaluate what would happen to an impact relating not only to the entirety of the system but also of its sub-elements (solar arrays, instruments and long appendages).

Therefore, even though the largest consequence event of total fragmentation is highly unlikely for small to large satellites (most problematic space debris objects are in this range), their sub-structures could still be at risk for masses $m_t \leq 1$ kg. However, usually bullets will hit the spacecraft structures with a fraction of the total impacting velocity (from conservation of impulse and momentum). Thus, the probability of the bullets impacting these sub-structures with the maximum velocity of 50 m/s is itself very low. Given the latter, it is concluded that this type of event is highly unlikely, and hence will not be discussed more in detail in this Thesis. It is still recommended for future research to evaluate the potential damages made on sub-structures of nano-satellites at low velocities ($V_p \leq 25$ m/s).

2.6.2. Impact characteristics

Given this first-order estimate, a secondary analysis taking into account material properties can be made. Impact events can be divided into two categories: soft and hard impact. Soft impact refers to an impact in which the projectile breaks, whereas hard impact results in target penetration. A limit criterion can be defined in terms of the projectile density ρ_p, stress threshold σ_p and velocity V_p, compared to the target's ultimate compressive strength σ_t [44]:

$$\frac{\sigma_p}{\sigma_t} + \frac{\rho_p V_p^2}{\sigma_t} = 1. \tag{2.3}$$

Due to the low velocity of net capturing (< 100 m/s), the impact is considered to only perforate the material without shattering or even melting it. Thus, defining the type of impact is usually not enough.

Its physical characteristics (depth, diameter and ejecta) can provide a better overview of the potential that net capturing has in breaking structures. This can be done by using a semi-empirical model which provides the penetration depth, δ_p, and crater diameter d_{Ct} of an impacting object with diameter d_p obtained with [84]:

$$\delta_p = K_1 \cdot d_p^{a_4} \cdot V_p^{a_2} \cdot (\cos(\theta_{imp}))^{a_5} \cdot \rho_p^{a_1} \cdot \rho_t^{a_3}, \tag{2.4}$$

$$d_{Ct} = 2 \cdot K_c \cdot \delta_p, \tag{2.5}$$

where ρ_t is the target density, θ_{imp} is the incidence angle, $K_1 = 5.24 \cdot BHN^{-1/4} \cdot C_s^{-2/3}$ (with Brinell hardness and speed of sound, $BHN = 93$ and $C_s = 5.3$ km/s, respectively) and the constants $a_1 = 0.5$, $a_2 = 2/3$, $a_3 = -0.5$, $a_4 = 19/18$, $a_5 = 2/3$ and K_c with a range of 1-10.

One can then obtain the critical projectile diameter, d_c, threshold for significant damage to occur when the penetration is approximately equal to the target wall [84]:

$$d_c = \left[\frac{t_w}{K_f \cdot K_1 \cdot V_p^{a_2} \cdot (\cos(\theta_{imp}))^{a_5} \cdot \rho_p^{a_1} \cdot \rho_t^{a_3}} \right]^{1/a_4}, \tag{2.6}$$

where $K_f = 1.8,\ 2.2,\ 3.0$ and t_w is the target wall in cm. Given this, the required bullet mass diameter to break the solar panel can be seen in Figure 2.13. The evaluation of this model for lower velocities than 3 km/s is allowed as the net capturing scenario is situated only in the perforating damage regime [37].
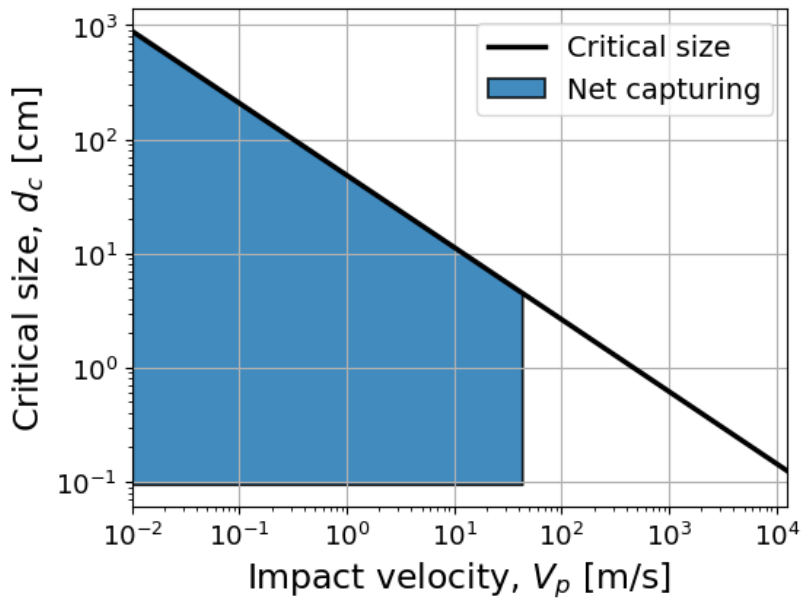
Figure 2.13: Critical net bullet diameter as a function of impact velocity.

It can be concluded that as the net impact velocity regime results in a minimum critical bullet size of 6 cm at 50 m/s, the risk of breaking is very low, but still not zero as typical bullet sizes are from 0.1 to 5 cm [15, 68]. Additionally, with more realistic impact velocities ranging from 1-20 m/s, these would require bullets of diameter ranging from 10 to 60 cm, which are much higher than presented in literature. Due to this, fracture breaking can be assumed to be highly **improbable** and is not to be discussed further in this study.

As a final note, with a 10 mm-thick solar array, a certain fragility is still present and for future work it is suggested to perform an impact-material numerical simulation, to completely rule out the possibility of fracture in the case of bullet-appendage impact.

2.6.3. Low-velocity impact risk considerations

From the above sub-sections, total fragmentation events have been deemed to be extremely unlikely and critical perforating events have also been seen to be improbable, and hence a reduced priority. However, whereas this eliminates the aforementioned risks, low-velocity impacts are not without consequences. Indeed, impact ejecta of around 50 mg can occur from spacecraft body surfaces for $V_p \sim 100$ m/s [37, 93]. Paint, thin or less massive sub-systems and upper layers of thermal blankets could be at risk. These small-sized secondary space debris objects could lead to hyper-velocity micro-impacts on other operational satellites, potentially limiting their functionality.

Thankfully, the probability of impact of these objects with other satellites is very limited and with the order of potential micro-sized secondary space debris of 10^{-3} kg, the dynamics-related risks described in section 2.3 seem to be more significant and need to be prioritised.

2.7. Simulation Scenarios

Due to the limited penetration capability of a net, especially at the typical speeds of 0.5-50 m/s [15, 68], damage caused by the net on the main space debris body at the moment of impact has been deemed highly improbable with low risk in section 2.6.

Additionally, large and long-period oscillations would be required for propellant sloshing (see subsection 2.3.2) to generate sufficient friction which could potentially cause an explosion. Due to the limited time-frame of the towing phase in which the space debris experiences the highest oscillations, propellant sloshing explosion is deemed as highly unlikely. Thus, the focus of this study is placed on the breaking of flexible appendages, the tensile failure of the net itself and finally the accounting of existing damage in the aforementioned appendages. The latter is seen as highly likely due to the high probability of impact of the solar panel or ASAR antenna with micro-debris, creating holes and cracks in the structure.

With these considerations in mind, it is now possible to design two specific simulations scenarios which allow an investigation of these dynamics-related risks. The first simulation scenario, which will dominate the Thesis, will be related to the net dynamics and impact phase with the Envisat spacecraft. The following aspects of the simulation scenario will be investigated:

1. net deployment,
2. satellite appendages - net impact,
3. wrapping net around the satellite.

The second simulation scenario will focus on the towing phase and how to safely perform the final removal process by limiting any risk of breaking of the satellite's long flexible appendages.

2.8. Target Orientation and Modelling

As the Envisat is considered to be the highest priority space debris and the target of interest of this Thesis study, it is essential to know its orientation defined w.r.t its Local-Vertical-Local-Horizontal (LVLH) coordinate system and to model it appropriately.

2.8.1. Target attitude and orientation

As can be understood from Figure 2.14, the Envisat constantly rotates around a spinning axis (S) with a rate estimated from 0.4 to even a maximum of 3.5 deg/s (estimated in January 2013) [85]. This rate seems to be decreasing with time, from January 2013, as found by Koshkin et al. [46] and Sommer et al. [80]. This would lead to a rotation rate in May 2023 of 0.9-1.1 deg/s.
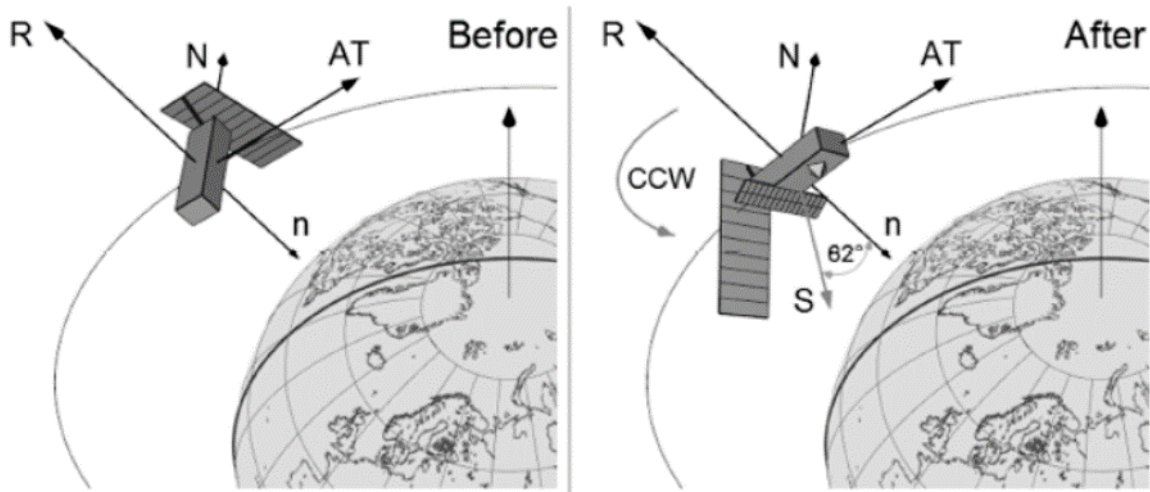
Figure 2.14: Envisat attitude orientation before and after mission end, from which it spins around the spin axis S, with coordinate vectors R (radial), N (along angular momentum) and AT (along-track). [43]

The Envisat's attitude can be assumed to be fixed during the entirety of the capturing phase. The latter is a reasonable assumption as typical net capturing ejection durations are between 0.5 to 5 s [15, 68]. Within this time, the Envisat would rotate 0.1 deg to a maximum of 5 deg which can be considered to be negligible due to the versatility and flexibility of the net capturing method. This is further confirmed by Shan et al. [76, 72], which showed that below a rotational rate of 0.7-1.5 rad/s, the net is still able to properly wrap around the debris without a closing mechanism. For the Envisat specifically, a more conservative maximum value of 5 deg/s is proposed by Benvenuto et al. [9] due to the large capturing distance and low velocity of 5 m/s. Thus, due to the small rotational rate of the Envisat and the high versatility of the capturing net, the Envisat's rotational rate around its spinning axis can be neglected for net capturing simulations.

2.8.2. Target modelling

Given these details, an assumed attitude needs to be selected for the reminder of this work in order to initiate the multi-disciplinary analysis. It is decided to fix the orientation of the Envisat to two attitude configurations or scenarios, visualised in Figure 2.15, with configuration (**B**) being implemented in the work of Shan et al. [76, 72] and orientation (**A**) being mostly related to other ASDR missions presented in [11, 25].

It can also be observed from Figure 2.15, that the Envisat is simplified to its main body, the ASAR, Ka-band antenna and the prominent single solar array. The antenna dish is modelled as a sphere with the same diameter, as it can be seen in Figure 2.7 that the Z_S-dimension is approximately equal to the dish diameter. The ASAR antenna is modelled with a null inclination angle, simplifying the contact detection algorithm. This choice is assumed to have no particular effect on the dynamic and structural analysis, as the main loading will be in compression.
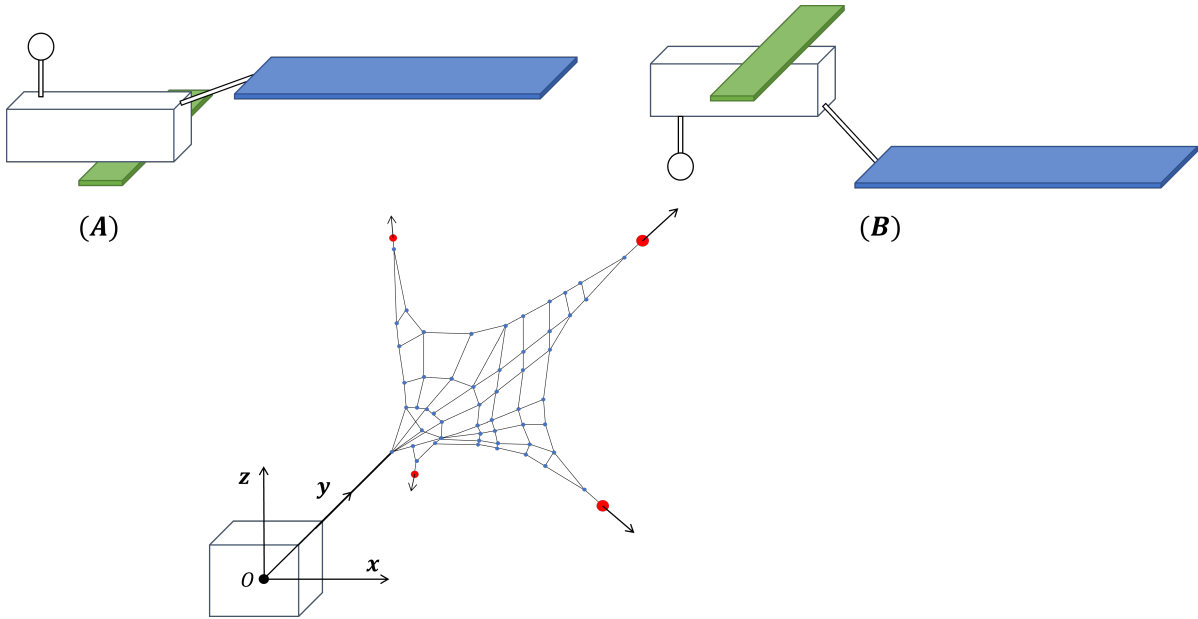
Figure 2.15: Envisat mock-up model with its both orientations, denoted as (**A**) and (**B**), within the net capturing context with origin O (chaser), $y-$direction representing the direction of flight, the radial coordinate as $x-$direction and the $z-$direction completes the frame.

For the solar panel, its sub-elements are modelled as straight to simplify the analysis, but also due to their very small relative angle of ± 3.18 deg (see Figure 2.3). Furthermore, the entire solar array is modelled without a slanted angle (see Figure 2.3). The latter conservative choice is made to simplify the contact detection and dynamics modelling, whilst also providing the worst case scenario both in terms of net capturing and the potentially highest solar array experienced forces and moments.

Finally, the dimensions and other specifications of the simplified Envisat model can be found in Table 2.4. Lastly, the mock-up can be chosen to be scaled by a factor f_{Env} ($0 \leq f_{Env} \leq 1$), scaling all the dimensions presented in Table 2.4. This last specification can be used to alleviate the contact detection algorithm by allowing for lower computational time.

Table 2.4: Envisat mock-up model parts and dimensions (based on [25, 85]) with $f_{Env} = 1$.

Envisat Part	Characteristic Dimensions (and angles)
Main body	10.0 [m] $\times$ 2.8 [m] $\times$ 2.6 [m]
Solar array connection	$l_c = 3.15$ m, $\alpha_c = 40$ deg
Solar array	14.3 [m] $\times$ 5.0 [m] $\times$ 0.30 [m]
SAR antenna	1.50 [m] $\times$ 10.0 [m] $\times$ 0.010 [m]
Ka ant. boom (length, diameter) and dish diameter	$l_b = 2.0$ m, $d_b = 0.146$ m, $d_{Ka} = 1.0$ m

3

Overview of the Dynamics Modelling & Implementation

In this chapter, the overview of the dynamical modelling strategy involved in an net capturing ASDR mission is presented. First, the general modelling strategy in section 3.1 will be presented, followed by the main system dynamics assumptions in section 3.2, and lastly the integration methods will be presented in section 3.3.

3.1. General Modelling Strategy and Assumptions

Given the fact that there are four different models in this study, an efficient modelling strategy is required. Indeed, there are three (to four) different models that have to be presented. The first model is associated to the net deployment and contact dynamics, for which the space debris object is assumed to behave as a rigid wall. The latter means that the space debris is unaffected by the net contact dynamics. From this, contact and quasi-static forces are obtained as outputs, which are then directly fed to the space debris dynamic model. This model is composed of two system dynamics models, a vibrational or dynamic sub-model which shows the displacements that occur at the various spacecraft connectors, and a structural sub-model that provides stress estimations resulting from the various loading configurations. With these final outputs a simplified failure model checks in a binary manner if failure occurs, and if yes, where and what is the size of the newly created secondary space debris.

Thus, due to the complexity of the problem and the interactions of the aforementioned models, it is decided to decouple the various models present in this study in order to simplify the implementation of the simulation whilst still providing a vast preliminary investigation on the subject. The sequential nature of the strategy can be visualised in Figure 3.1. Thus, it is essential to mention that even though the space debris is not directly affected by the net contact dynamics, a post-processing simulation of its translational and rotational dynamics is implemented. The aforementioned would allow, in a preliminary manner, to see what are the effects and potential risks that net contact and wrapping can cause.

3.2. Main System Dynamics Assumptions

Given the multitude of models to be used, it is essential to simplify the system modelling process.

3.2.1. Chaser system modelling assumptions

First, in this study, the chaser is the spacecraft that ejects and deploys the net for it to capture the debris object. For all the discussed mission phases, it is assumed to be a point mass, as it was discussed that its potential risks in generating more space debris are very low during net deployment and contact.

3.2.2. Space debris system dynamics assumptions

Secondly, when considering the dynamics as a potential source of generating additional debris, all space-craft debris are assumed to be single or two-rigid body systems. With this definition, multiple dynamic scenarios are envisaged with the purpose to identify if secondary space debris would be generated during the mission. Simple rigid-body shaped space debris are used as a verification and validation tool, whereas the Envisat (main case study) is modelled as a composite cuboid with a spherical antenna (see subsection 2.8.2). System failure is verified by post-processing normal and shear stress values.

3.2.3. Net system dynamics assumptions

Thirdly, the net system is modelled differently depending on the phase of the mission. For the deployment and impact phases, the net is modelled as a Multi-Spring-Damper mass system. The entire mass of the net body is assumed to be equally distributed over its nodes, with the connecting threads being **massless**. Their tensile behaviour is modelled using the Kelvin-Voigt linear spring-damper connector and thus any lateral component of the tension force is **neglected**. The self-interaction between the net nodes **is also ignored**, as the effect of net entanglement is assumed to have a small dynamic effect. Lastly, during the towing phase, the net is modelled as a bridle connected to the debris in one point.

3.2.4. Net-debris contact assumptions

Finally, a contact dynamics model will be established using a hybrid contact-force method. For the contact definition, Hertzian theory is used assuming that an elastic collision occurs at the intersection between a sphere and a plane. A virtual inter-penetration is computed, which results in a normal and tangential response force. These are then used to compute the final nodal velocity and position, as a kinematic constraint, fed back to the net dynamic model.

3.3. Integration Methods

A large number of differential equations will be used, resulting from the relevant dynamical problems. Thus, integration methods are required. Depending on the problem in question, two time fixed methods will be used with the addition of *odeint* (python module) [1]. These are symplectic Forward Euler (**FE**) and a 4th order Runge-Kutta (**RK4**).

First, it is essential to mention that any generic differential equation can be written of the form:

$$\dot{\boldsymbol{y}}(t) = \boldsymbol{f}(t, \boldsymbol{y}(t)), \tag{3.1}$$

where $\dot{\boldsymbol{y}}(t)$ is the time derivative of the system state $\boldsymbol{y}(t)$ and can be written as a function of the latter.

Thus, to solve such a differential equation, a time integrator is required which approximates the state $\boldsymbol{y}(t)$ and propagates it forward in time. The symplectic **FE** integrator estimates the state $\boldsymbol{y}(t)$ as:

$$\boldsymbol{y}(t_i + \Delta t) = \boldsymbol{y}(t_i) + \Delta t \cdot \boldsymbol{f}(t_i, [\boldsymbol{x}(t_i), \dot{\boldsymbol{x}}(t_i + \Delta t)]^T) + O(\Delta t^2), \tag{3.2}$$

where Δt is the time-step, $\boldsymbol{x}(t_i)$ is the state position component and $\dot{\boldsymbol{x}}(t_i + \Delta t)$ is the velocity at the next step. This method is simple with a Δt^2-order local error, but can be unstable for specific Δt values.

Secondly, a multi-step time integration method known as **RK4**, provides a more precise estimate of the propagated state. Due to its multi-step nature, there are intermediate integration steps:

$$\boldsymbol{k}_1 = h \cdot \boldsymbol{f}(t_i, \boldsymbol{y}_i), \tag{3.3} \qquad \boldsymbol{k}_2 = h \cdot \boldsymbol{f}(t_i + h/2, \boldsymbol{y}_i + \boldsymbol{k}_1/2), \tag{3.4}$$

$$\boldsymbol{k}_3 = h \cdot \boldsymbol{f}(t_i + h/2, \boldsymbol{y}_i + \boldsymbol{k}_2/2), \tag{3.5} \qquad \boldsymbol{k}_4 = h \cdot \boldsymbol{f}(t_i + h, \boldsymbol{y}_i + \boldsymbol{k}_3), \tag{3.6}$$

with the final update of the state as:

$$\boldsymbol{y}(t + h) = \boldsymbol{y}_{i+1} = \boldsymbol{y}_i + \frac{1}{6} \cdot (\boldsymbol{k}_1 + 2\boldsymbol{k}_2 + 2\boldsymbol{k}_3 + \boldsymbol{k}_4) + O(h^5). \tag{3.7}$$

Here h is used as the time step for simplicity, and the local error of this method can be seen to be of order h^5. Thus, **RK4** can be a more efficient algorithm, requiring a larger h than **FE** for similar accuracy.

---

[1] https://docs.scipy.org/doc/scipy/reference/generated/scipy.integrate.odeint.html
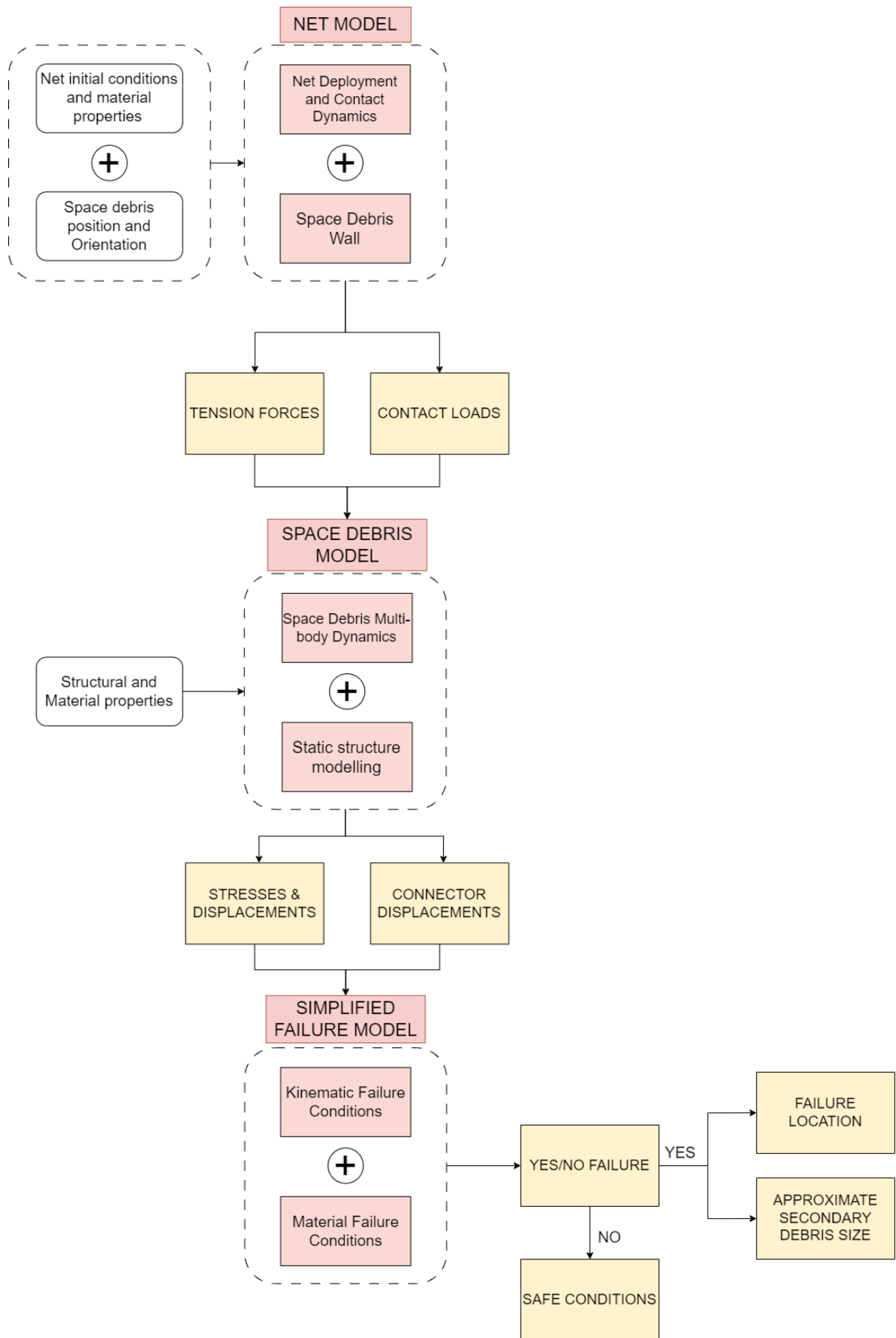
Figure 3.1: Thesis Sequential Modelling Strategy decoupling the three main models used.

<div style="text-align: right">

4

</div>

Net Dynamics Modelling

4.1. Reference System

A rotating Local-Vertical-Local-Horizontal (LVLH) coordinate system will be used, as it is the typical choice for in-orbit servicing operations. The chaser spacecraft is chosen as the origin, O, of the reference system. In this thesis, the following notations for the axis will be used:

- x: Radial.
- y: Along-track or flight direction.
- z: Cross-track.

In this work, the net deployment direction is assumed to be in the flight-direction. All of this can be found visualised in Figure 4.1.
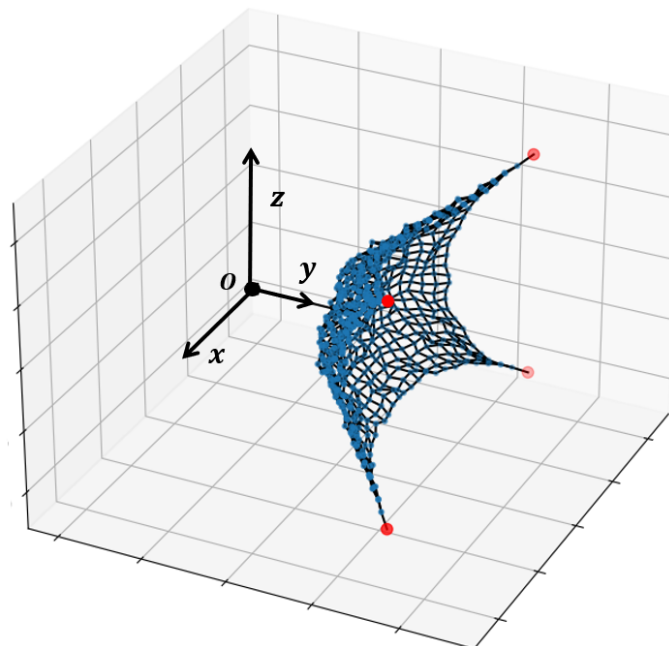
Figure 4.1: Representation of the coordinate system with origin O, $y-$direction representing the direction of flight, the radial coordinate as $x-$direction and the $z-$direction completes the frame.

4.2. Net Modelling for deployment and impact phases

For the contact and capture phases, the net model must now deal with the impact and wrapping around the target. This requires the modelling of the flexibility behaviour of the net. By taking the previous

final state as the initial conditions for this phase, the net is modelled using a Multi-Spring-Damper Model (**MSD**) [10, 15, 69].

4.2.1. Net characteristics and mesh generation

The **MSD** model discretises the net into N_i^2 node masses all connected with each other by spring-damper systems, where N_i is the number of nodes on one side of the net. In this thesis, the net has the following characteristics:

1. The net is of square shape with side length L_{net}.
2. The net mass is distributed over point masses, m_i, called nodes (for $i \in 0, ..., N_i^2$).
3. Four equal bullet masses, m_b, are externally attached to the corners.
4. All the threads have the same unstretched length, l_{0_q} and diameter d_q.
5. The threads can only stretch in the longitudinal direction.
6. The elasticity behaviour of all threads is purely characterised by the axial stiffness, k_q, and damping coefficient, c_q.

   Given these characteristics, the mesh of the main internal net can be created using the same strategy as proposed by E. Botta [15]. The ith and j^{th} nodes of the qth thread are generated as follows [15]:

$$(j = i + 1 \wedge i \mod N_i \neq 0) \vee (j = i + N_i) \tag{4.1}$$

for all $i = 1, 2, ..., N_i^2$ and $j = i + 1, ..., N_i^2$. With the four additional bullet masses, the total number of nodes is $N = N_i^2 + 4$ with N_c internal corner cable elements as $N_c = 2N_i \cdot (N_i - 1)$.

4.2.2. Tether-net modelling

To connect the net to the chaser spacecraft a tether is used with a methodology created in this work. For odd values of N_i, the connection is simply the middle node $i_t = (N_i^2 + 1)/2$. However, in the case that N_i is even, an additional middle node is required. The node index is then $i_t = N_i^2 + 1$, with the four other connections related to nodes:

$$j_{t_{1,3}} = N_i^2 - \left(\frac{N_i \pm 1}{2} \right) \cdot N_i, \tag{4.2}$$

$$j_{t_{2,4}} = j_{t_{1,2}} + 1. \tag{4.3}$$

A visual representation of the net mesh nodes and added threads for even N_i can be found in Figure 4.2.
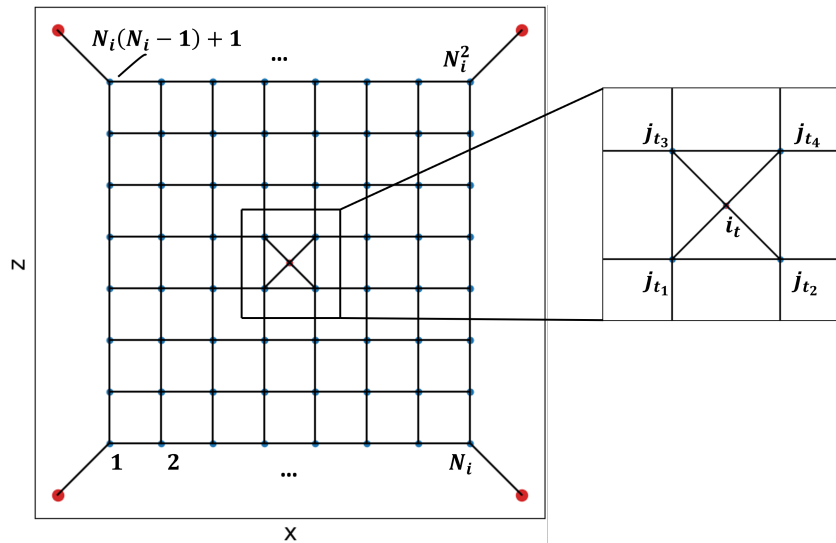
Figure 4.2: Mesh generation for the net system (xz plane) and zoomed net-tether connection indices for even N_i.

4.2.3. Multi-Spring-Damper force modelling

Having accurately defined the basic assumptions of net modelling and the generation of its nodes, their interactions must now be modelled.

To avoid for the possibility that the cable elements would compress, the linear Kevin-Voigt model [69] is used. The tension vector, $\boldsymbol{T}_{ij}$, on node i due to j within the thread q is as [73]:

$$\boldsymbol{T}_{ij} = \begin{cases} (-k_q \cdot (r_{ij} - l_0) - c_q \cdot \dot{r}_{ij})\frac{\boldsymbol{r}_{ij}}{r_{ij}} \text{ for } r_{ij} > l_{0_q} \\ 0 \cdot \frac{\boldsymbol{r}_{ij}}{r_{ij}} \text{ for } r_{ij} \leq l_0 \end{cases} \tag{4.4}$$

where k_q and c_q are the spring and damping coefficient of the mass-spring-damper model which describe the cable material, $\boldsymbol{r}_{ij}$ is the relative position vector with norm r_{ij} between the ith and j^{th} nodes and $\dot{r}_{ij}$ is relative velocity.

The first constant to be computed is the spring constant or axial stiffness, k_q, of the qth thread:

$$k_q = \frac{E_q \cdot A_q}{l_{0_q}}, \tag{4.5}$$

where E_q is the thread material elastic Young's Modulus and A_q is the cable cross-sectional area. A major assumption for this equation is that the net is made of a **homogenous isotropic linear material** and thus as mentioned above assumes no lateral loading.

The damping coefficient c_q can be estimated experimentally such as in [81] using:

$$c_q = 2\zeta\sqrt{\rho_{net} \cdot l_{0_q} \cdot A_q \cdot k_q}, \tag{4.6}$$

where ζ is the damping ratio and ρ_{net} is the density of the material.

A simplified representation of the net with its point masses and spring-damper elements can be seen in Figure 4.3.
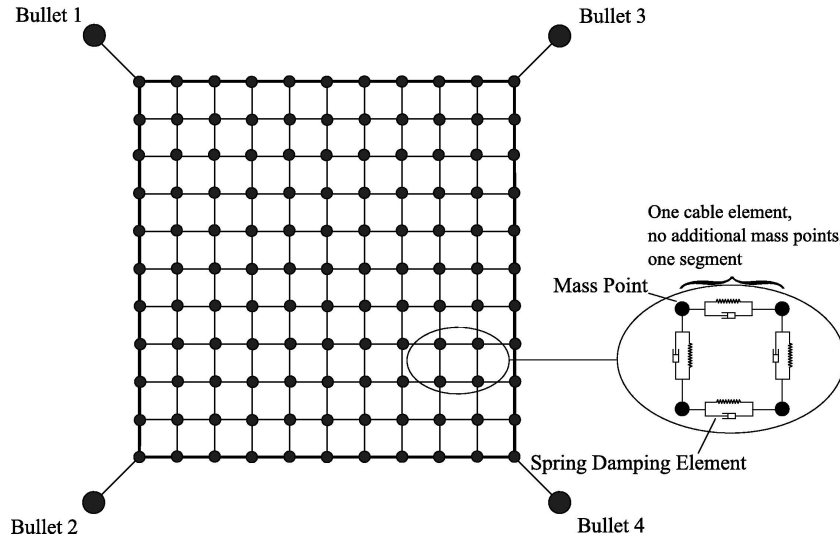
Figure 4.3: Multi-Spring-Damper mass model for flexibility modelling (obtained from [70]).

The same tension model is used for the connecting tether. The latter, however, is modelled as a double-mass-spring-damper with properties k_t, c_t and l_{0_t} computed using Equation 4.5 and Equation 4.6, with its design process described in Appendix C.

4.2.4. Equations of motion for net systems

The equations of motion (EoM) which govern each net lumped point mass, m_i, can be obtained using Newton's second law in the inertial reference frame of the chaser:

$$m_i \ddot{\boldsymbol{r}}_i = \sum_{j=1}^{N_t} \boldsymbol{T}_{ij} + \sum_{p=1}^{P} \boldsymbol{F}_{ext,i_p}, \tag{4.7}$$

where N_t is the number of adjacent cables connected to the ith mass and $\boldsymbol{F}_{ext,i_p}$ any external force contribution and disturbances that are present in the space environment such as solar radiation, aerodynamic drag and the contact forces.

In order to integrate the aforementioned EoMs, the state $\boldsymbol{s} = [\mathbf{X}^T, \ \mathbf{V}^T]^T$, is defined, where $\mathbf{X}$ and $\mathbf{V}$ are the stacked net nodes position ($\boldsymbol{r}_i$) and velocity vectors ($\dot{\boldsymbol{r}}_i$). The state derivative, $\dot{\boldsymbol{s}}$ can hence be obtained as [15]:

$$\dot{\boldsymbol{s}} = \begin{pmatrix} \mathbf{V} \\ \mathbf{M}^{-1}\mathbf{F}_{sys} \end{pmatrix} \tag{4.8}$$

where $\mathbf{M}$ is the diagonal mass matrix of all net and bullet nodes masses, and $\mathbf{F}_{sys} = \mathbf{T}_{sys} + \mathbf{F}_{ext}$ is the stacked, internal ($\mathbf{T}_{sys}$) and external ($\mathbf{F}_{ext}$) forces exerted on the net. These are stacked as follows:

$$\mathbf{T}_{sys} = \left(\sum_{j=1}^{N_t} \boldsymbol{T}_{0j}^T \ \cdots \ \sum_{j=1}^{N_t} \boldsymbol{T}_{Nj}^T \right)^T, \tag{4.9}$$

$$\mathbf{F}_{ext} = \left(\sum_{p=1}^{P} \boldsymbol{F}_{ext,0_p}^T \ \cdots \ \sum_{p=1}^{P} \boldsymbol{F}_{ext,N_p}^T \right)^T. \tag{4.10}$$

4.2.5. Impact of orbital dynamics

As the net is in orbit around the Earth, it is necessary to correct Equation 4.7 by including the influence of relative orbital dynamics between the target and the chaser. Knowing that the reference frame used is a relative one (w.r.t the chaser), Clohessy-Wiltshire equations [22] can be used. These equations assume that (1) the chaser-target distance is small compared to the orbital radius, (2) the chaser orbit is circular, and (3) that the orbital angular rate is constant. This leads to the following:

$$\ddot{\boldsymbol{r}}_i = \omega_n^2 \begin{pmatrix} 3 \cdot x_i \\ 0 \\ -z_i \end{pmatrix} + 2 \cdot \omega_n \begin{pmatrix} \dot{y}_i \\ -\dot{x}_i \\ 0 \end{pmatrix} + \frac{1}{m_i} \cdot \sum_{j=1}^{N_t} \boldsymbol{T}_{ij} + \frac{1}{m_i} \cdot \sum_{p=1}^{P} \boldsymbol{F}_{ext,p} \tag{4.11}$$

where one can identify the gravitational corrections of the frame of references with the mean motion $\omega_n = \sqrt{\mu/a^3}$. Therefore, depending on the orbital semi-major axis, a, the correction terms highly vary. In the case of net capturing, relative distances are of the order of 10 m, whereas relative orbital speeds vary from 1 to 25 m/s [15, 68].

Given that the main case study is the Envisat, one can assume an altitude of 772 km. The mean motion is then $\omega_n = 1.044 \cdot 10^{-3}$ rad/s. With the aforementioned range of relative distances and velocities, the two correction terms would be of order 10^{-5} m/s² and 10^{-2} m/s². Due to the usually small capture time of around 1 to 50 s [16, 17, 69, 71, 72], and the magnitude of the tensile forces ranging from 1 to 1000 N, these corrections can be neglected. These linear orbital dynamic corrections would further decrease in the case of the Jason satellites (high LEO), to even net capturing in MEO (Medium Earth Orbit) to GEO (Geostationary Earth Orbit) as ω_n would significantly decrease.

4.3. Initial and Nominal Conditions

Two sets of initial conditions can be defined. These will be discussed in this section.

4.3.1. Deployment phase

The simulation of the net deployment is initiated by assuming that the entire net is packed by a factor η_{net}, where $0 < \eta_{net} < 1$ as done in [15]. The bullets are symmetrically ejected with velocity V_e and shooting angle θ_e, whereas the main body of the net has a purely horizontal (along y-direction) velocity $V_{net} = \eta_V V_e$. The η_V factor represents the latency that the net body has w.r.t to the bullets and has been shown to improve the accuracy of the deployment phase simulation [15].

4.3.2. Nominal impact conditions

Ideally, the moment that the net hits the spacecraft, a certain set of conditions would need to be met for optimal capture. Therefore, the simulation would start from the following ideal initial conditions (**IID**):

1. The maximum net mouth area, S_{max}, is 100% the maximum capacity (L_{net}^2).
2. The net mouth area and bullet threads are perpendicular to the direction of motion ($y-$direction).
3. The Center-of-Mass (CM) of the net is centered for $x = z = 0$.
4. All threads are unstretched.

4.3.3. Non-nominal impact conditions

In order to attain such conditions, it is assumed that the net is fully deployed without ejection or is controlled by a net robot unit system (TSNR) [98]. For the non-nominal initial conditions before impact, these would be set from deployment with the space debris positioned such that the net would have similar impact optimal conditions as in the nominal case. The target for the impact net mouth area (**IID1**) would be changed to $S_{max} \geq 0.85 L_{net}^2$ and **IID2** would be removed. Thus, to position the chaser accordingly, certain capture mission properties will be discussed in the next section.

4.4. Capture Mission Net Dynamic Properties

The final dynamic net characteristics that need be presented relate to the mission itself. These are the capture distance, and deployment and capture time.

The distance at which the net will impact the space debris is chosen to correspond to the distance when the net fully deploys. This is found to be a geometrical property as suggested in [65] and can be computed as follows:

$$d_{capt} \approx \frac{\sqrt{2}L_{tot}/2}{\tan(\theta_e)}, \tag{4.12}$$

where L_{tot} corresponds to the total size of the size ($L_{tot} = L_{net} + 2l_{0_q}$) and θ_e is the bullet shooting angle. Following the capture distance, the deployment time can be computed using the net center-of-mass velocity V_{CM} and the principle of impulse and momentum [65]:

$$V_{CM} = \frac{4m_b}{(m_{net})_{tot}} \cdot V_c \cdot \cos(\theta_e) + V_{net}, \tag{4.13}$$

from which the time is then simply $t_{dep} = d_{capt}/V_{CM}$. However, as the target wrapping would also be of interest, the simulation end time must be larger. A relationship for the wrapping time, which assumes a cubic target shape, can be found in [65]. By adapting the latter relationship [65] to a more generic space debris geometry, the following is obtained:

$$t_{wrap} = 1.5\frac{0.5\pi \cdot (L_{tot} - s)}{2 \cdot V_{CM}}, \tag{4.14}$$

where s corresponds to the smallest front dimension of the target. Finally, the factor 1.5 is added to correct for the underestimating analytical nature of the equation [65], providing also an additional buffer.

<div style="text-align: right; font-size: 3em;">5</div>

Contact Dynamics Modelling

In this chapter, the methodology for contact dynamics (section 5.1) and detection (section 5.3) modelling is presented. Lastly, the model's limitations are shown in section 5.2.

5.1. Penalty-based Method

The penalty-based contact method is presented in this section from its basic principles to the application on the net dynamics.

5.1.1. Basic principles

The basic principle of the penalty-based contact dynamics method, is that the contact is based on the response contact force $\boldsymbol{F}_c$:

$$\boldsymbol{F}_c = F_n\hat{\boldsymbol{n}} - F_t\hat{\boldsymbol{t}}, \tag{5.1}$$

where F_n and F_t are the normal and tangential force components with unit vectors $\hat{\boldsymbol{n}}$ and $\hat{\boldsymbol{t}}$, respectively.

Computing these two forces results in the time-dependent continuous force estimate experienced by the colliding bodies. The estimation method for both is laid down in the following subsections.

5.1.2. Normal force

The normal force is computed assuming that the impact between two bodies is equivalent to the compression phase of a mass-spring-damper system as can be seen in Figure 5.1.
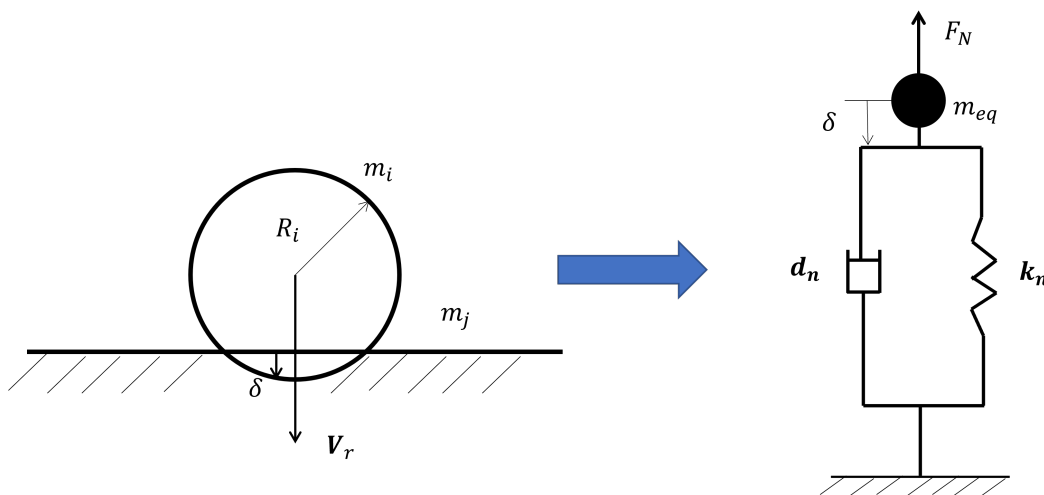
Figure 5.1: Collision impact equivalence modelling between sphere with mass m_i and infinite plane m_j, with (non-)linear spring-damper system (k_n and d_n) connected to an equivalent mass m_{eq} and virtual deflection δ.

Furthermore, there are three essential characteristics which are required to have a consistent impact model:

1. The normal force should be zero at zero penetration.
2. The normal force should always be positive.
3. The normal force should accurately model damping effects.

There exists three varying models for this contact force which are thoroughly described by Gilardi and Sharf [33], with a summary in Table 5.1.

Table 5.1: All Contact Dynamic Force Models with typical use comparison, augmented table from [68, 23]

Contact Models	Expression	Typical Use
Spring-dashpot model	$F_n = k_n \cdot \delta + d_n \cdot \dot{\delta}$	Fast and simple (low accuracy)
Hertz's model	$F_n = k_n \cdot \delta^n$	Low impact speeds (hard materials) [33]
Non-linear damping model	$F_n = k_n \cdot \delta^n + d_n \cdot \dot{\delta} \cdot \delta^n$	High accuracy required

In the expressions described in Table 5.1, d_n and k_n are the damping and spring coefficients, δ and $\dot{\delta}$ are the penetration depth and rate, and n is the material exponent dependent on the object's geometry and material (usually chosen as 1.5 [77]). The dynamic behaviour of these forces can be seen in Figure 5.2.
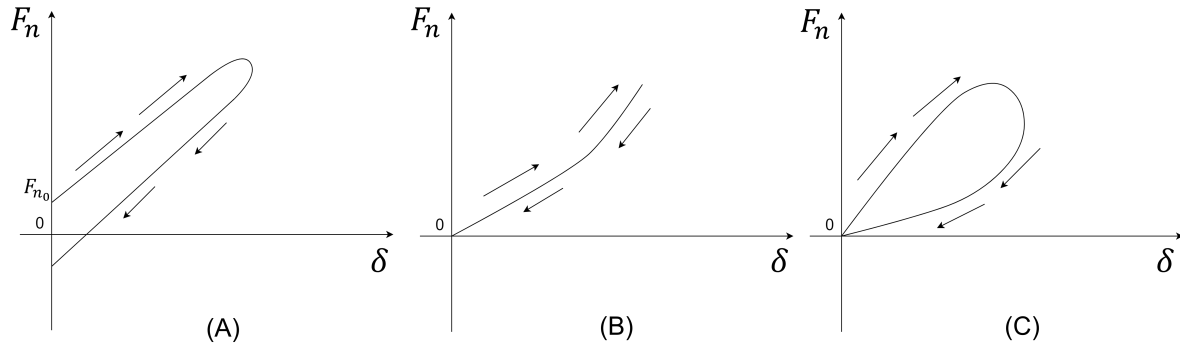
Figure 5.2: Contact dynamics force models; (A) Spring-dashpot model. (B) Hertz's model. (C) Non-linear damping model. (taken from [23] and modified from [68])

In this Thesis, the non-linear damping model is chosen due to its various advantages compared to the linear and Hertz models [33]. In fact, as can be directly seen in Figure 5.2, the linear model results in a non-zero force at zero penetration depth, which is unrealistic. Additionally, the model assumes that the coefficient of restitution is independent of the pre-impact velocity, which was proven to be false by Goldsmith in [35]. Lastly, the Hertzian model assumes no energy dissipation (no damping included) which is also unrealistic and confirms the aforementioned choice. The normal force model is hence:

$$F_n = k_n \cdot \delta^n + d_n \cdot \dot{\delta} \cdot \delta^n. \tag{5.2}$$

As an initial modelling step of the net node impact, each net node is assumed to be a sphere with radius R_i, taken as the thread radius ($R_i = d_q/2$, see section 4.2). The virtual deflection, in the normal direction, is thus given by:

$$\delta = |\boldsymbol{r}_{i/s} \cdot \hat{\boldsymbol{n}} - R_i|\eta_i, \quad \text{with } \eta_i = \begin{cases} 1 \text{ for } (\boldsymbol{r}_{i/s} \cdot \hat{\boldsymbol{n}} - R_i) \leq 0 \\ 0 \text{ for } (\boldsymbol{r}_{i/s} \cdot \hat{\boldsymbol{n}} - R_i) > 0 \end{cases} \tag{5.3}$$

where $\boldsymbol{r}_{i/s}$ is the net position w.r.t the debris surface.

Given the non-linear spring-damper contact force model, one can finally write the associated equation of motion related to the virtual deflection δ:

$$m_{eq}\ddot{\delta} = -F_n, \tag{5.4}$$

where m_{eq} is the equivalent mass of impact of masses m_i and m_j and can be computed as

$$m_{eq} = \frac{m_i m_j}{m_i + m_j}. \tag{5.5}$$

In the case of net capturing, the mass of one net node i, is much smaller than the target's mass (m_j) or $m_i << m_j$ which results in $m_{eq} \approx m_i$.

The last step, is to estimate the equivalent constant parameters of F_n. Due to the size difference between a net node and the target's surface, the collision is modelled as a sphere-plane impact (see Figure 5.1). With Hertzian contact theory [71, 87], the stiffness (spring) constant is:

$$k_n = \frac{4\sqrt{R_q}}{3\pi \cdot (h_1 + h_2)}, \tag{5.6}$$

where R_q is the net node radius and with h_k as follows:

$$h_k = \frac{1 - \nu_k^2}{\pi E_k}, \text{ with } k = 1, 2 \tag{5.7}$$

for which E_k and ν_k are the elastic Young's modulus and the Poisson's ratio material properties of the net node ($k = 1$) and target ($k = 2$) surface.

The last force coefficient is the damping coefficient, which can be estimated using the Hunt and Crossley method as follows [68]:

$$d_n = \frac{3\alpha k_n}{2}, \tag{5.8}$$

where α is an experimental variable varying in the range $[0.08, \ 0.32]$ s/m [9]. For this equation to be correct, low velocities are assumed for which the coefficient of restitution e can be written as:

$$e = 1 - \alpha V_n \tag{5.9}$$

with $V_n = (\boldsymbol{V} \cdot \hat{\boldsymbol{n}})$ being the normal component of the velocity vector before impact.

Lastly, the initial conditions at the moment of impact, δ_0 and $\dot{\delta}_0$, are chosen using Equation 5.3 and the normal component V_n, respectively. These are the initial parameters used to solve the system of equations of Equation 5.4 with the state $\boldsymbol{\delta} = [\delta, \dot{\delta}]^T$.

5.1.3. Friction force

Secondly, given the normal force and tangential velocity, the friction force $\boldsymbol{F}_t$ can be directly computed using Hollar's model [68]:

$$F_t = \begin{cases} \left[\mu_k + \dfrac{2(\mu_s - \mu_k)}{1 + \left(\frac{V_t}{V_{t,0}}\right)^2}\right] F_n, & \text{for } V_t \geq V_{t,0} \\[4em] \left(\dfrac{V_t}{V_{t,0}}\right) \cdot \left[\mu_k + \dfrac{2(\mu_s - \mu_k)}{1 + \left(\frac{V_t}{V_{t,0}}\right)^2}\right] F_n, & \text{for } V_t < V_{t,0} \end{cases} \tag{5.10}$$

$$\boldsymbol{F}_t = -F_t \hat{\boldsymbol{t}}, \tag{5.11}$$

where μ_s and μ_k are the static and kinetic friction coefficients, $\hat{\boldsymbol{t}}$ is tangential unit vector, $V_{t,0}$ is the break-away or transition velocity between static and dynamic friction and V_t is the tangential velocity. The latter velocity component, $\boldsymbol{V}_t$, is computed as:

$$\boldsymbol{V}_t = \boldsymbol{V}_r - V_n \hat{\boldsymbol{n}} \tag{5.12}$$

where $\boldsymbol{V}_r$ is the relative velocity between the net and the space debris. Lastly, the tangential unit vector is computed using a sign relaxation method at speeds below $V_{t,0}$ to avoid numerical errors [65]:

$$\hat{\boldsymbol{t}} = \begin{cases} \frac{\boldsymbol{V}_t}{V_t}, & \text{for } V_t \geq V_{Coul} \\ \frac{\boldsymbol{V}_t}{V_{Coul}} \left(\frac{3}{2} \frac{V_t}{V_{Coul}} - \frac{1}{2} \left(\frac{V_t}{V_{Coul}} \right)^3 \right), & \text{for } V_t < V_{Coul} \end{cases} \tag{5.13}$$

where V_{Coul} is the Coulomb velocity threshold obtained using the approximation of the Stribeck curve $V_{Coul} = \sqrt{2} V_{t,0}/10$.

With both normal and tangential forces presented, the reaction force on the space debris can be computed as $-\boldsymbol{F}_c$.

5.2. Model Limitations

Having described the penalty-based method, it should be noted that the method has limitations and further issues. It seems to have strong instabilities and high dependence on the initial virtual deflection (at the moment of contact). Due to these issues, the method seems to present different results depending on the configuration of the problem in question.

This problem is thoroughly described in [68], in which the differential equations of motion are defined as stiff, therefore requiring a highly fine tuned initial deflection. Shan Minghe [68] presents a solution by removing the need of the virtual deflection and modelling the collision using the principle of impulse and momentum. The impulse-based method simply describes the change in velocity, due to the impulse $\boldsymbol{j}_i = j_i \hat{\boldsymbol{n}}$ (see details in section 6.2). This is then added to the node velocity ($\boldsymbol{V}_i$) and debris linear and angular velocities ($\boldsymbol{V}_d$ and $\boldsymbol{\omega}_d$) at the impact position $\boldsymbol{r}_{i/d}$ as [68]:

$$\boldsymbol{V}_i^+ = \boldsymbol{V}_i^- + \frac{j_i}{m_i} \hat{\boldsymbol{n}}, \tag{5.14}$$

$$\boldsymbol{V}_d^+ = \boldsymbol{V}_d^- - \frac{j_i}{m_d} \hat{\boldsymbol{n}}, \tag{5.15}$$

$$\boldsymbol{\omega}_d^+ = \boldsymbol{\omega}_d^- - \mathbf{I}_d^{-1} (\boldsymbol{r}_{i/d} \times j_i \hat{\boldsymbol{n}}), \tag{5.16}$$

where $\mathbf{I}_d$ is the debris mass moment of inertia matrix. However, this method yields the impulse caused by the impact, which would need to be translated back to a force for it to be useful in this study with $\boldsymbol{F}_c = \mathrm{d}\boldsymbol{j}/\mathrm{d}t$. Consequently, this would be highly dependent on the integration time step and for the impact assumed instantaneous, it would result in an averaged constant value.

Given this, a hybrid penalty-based method is chosen. In the latter, for the net's reaction only the velocity and final positions are retrieved from the internal integration procedure during contact with the spacecraft. These are then artificially applied to the net model for the ith node as:

$$(\boldsymbol{V}_i)_f = \dot{\delta}_f \hat{\boldsymbol{n}} + (\boldsymbol{V}_t)_f, \tag{5.17}$$

and for the net node position ($\boldsymbol{x}_i$) is set to:

$$(\boldsymbol{x}_i)_f = (\boldsymbol{x}_i)_0 + \hat{\boldsymbol{n}} \delta_0, \tag{5.18}$$

where the subscripts 0 and f denote, respectively, the initial and final conditions (before and after) the impact. This effectively makes it a discrete model similar to the impulse method for the net contact dynamics, with reaction velocities retrieved from the continuous model. The response force is then used as an input to the dynamic spacecraft model as the physical dynamic load experienced by the spacecraft.

5.3. Contact Detection

As the last part of contact dynamics modelling, it is essential to mention how a contact itself can be detected. For the latter, a modified version of the Axis-Aligned Bounding Box or AABB method presented in [68] will be used. For this method, the different systems are contained within their bounding boxes defined by their most extreme coordinates.

The contact detection strategy is divided in a hierarchical four-level step process. This starts with the "zeroth" level, in which the maximum $y-$coordinate of the net is verified to be lower than $0.75 \cdot y_{surf}$ (space debris surface). This is used to reduce the computational time by avoiding any unnecessary checks.

The first level of detection activates after that and verifies that there is no intersection between the bounding boxes of the net and space debris object. This is followed by the second level, which identifies that the bounding boxes do intersect. From this, the distance between the surface of the bounding sphere of one node and the body surface is checked to be positive (or above a threshold ϵ_d). A visualisation of level one to two can be found in Figure 5.3.
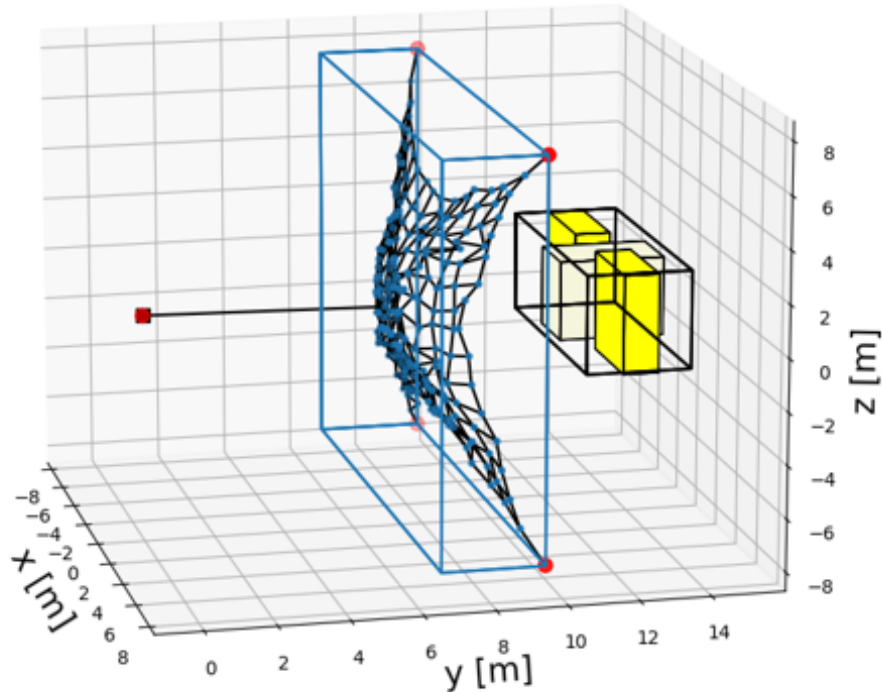
Figure 5.3: Simulation scenario example of contact boxes Level 1 to 2 for both net and target systems.

Lastly, the third-level results in the actual identification of detection in which the distance between surface of a net node and the debris surface is negative or zero (below the threshold ϵ_d). When that is the case, the contact surface and direction are retrieved and then the normal, $\hat{n}$, and tangential, $\hat{t}$ vectors are computed accordingly. If the space debris is shaped as a parallelepiped, the different faces of contact dictate the direction of $\hat{n}$. The direction of the face (positive or negative) is obtained from the maximum node-debris distance. For a sphere-sphere contact, the normal vector is obtained directly as the unit direction from the center of the target to the net node.

Given this information, the unit vectors can be defined and the contact force (see Equation 5.1) is then integrated (with Equation 4.7) to provide the velocity when the sphere stops intersecting the target. A summarising representation of the scheme can be found in Figure 5.4.
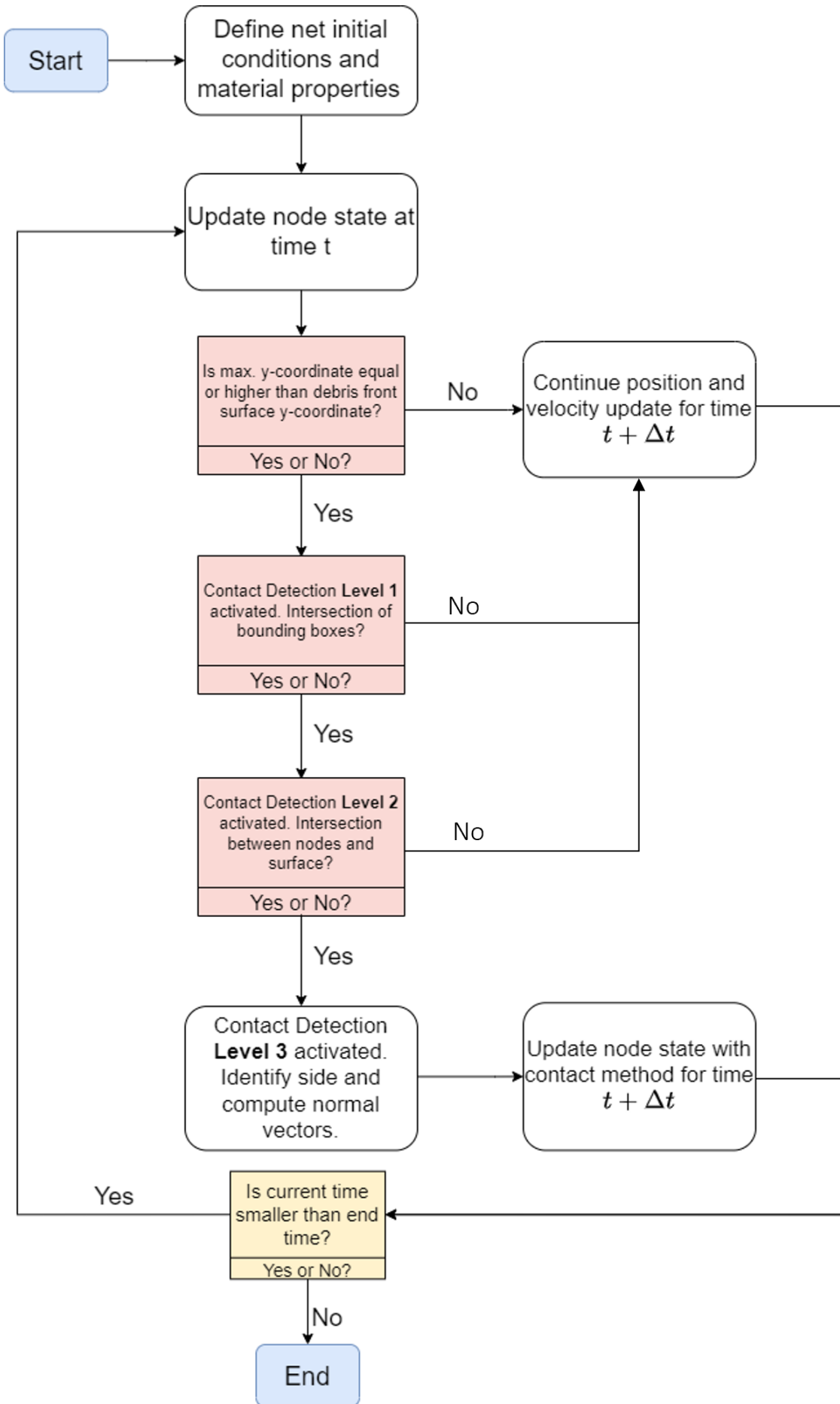
Figure 5.4: Contact Detection Scheme Diagram.

<div style="text-align: right; font-size: 4em;">6</div>

Spacecraft Dynamics Modelling

In this chapter, the space debris dynamics and all associated modelling strategies and assumptions will be presented.

6.1. Reference Frames

The net dynamics reference frame was already presented in Chapter 4 and was chosen to be a LVLH $O\text{-}xyz$ rotating frame attached on the chaser spacecraft (denoted as $\mathcal{L}$). For the target spacecraft, the assumption of ignoring the impact of orbital dynamics is no longer valid, thus requiring additional reference frames to write the system's EoMs.

All dynamics must be defined w.r.t an inertial reference frame $\mathcal{N}$ with origin N (placed at Earth's center) and its basis vectors $\{\hat{\boldsymbol{n}}_1, \hat{\boldsymbol{n}}_2, \hat{\boldsymbol{n}}_3\}$. The target spacecraft is assumed to orbit around the Earth in a circular orbit and is characterised by its body-fixed reference frame $\mathcal{B}$, origin B and basis vectors $\{\hat{\boldsymbol{b}}_1, \hat{\boldsymbol{b}}_2, \hat{\boldsymbol{b}}_3\}$. Furthermore, in the case of co-moving solar arrays, a reference frame $\mathcal{H}$ can be defined with origin H (at the solar array hinge) and basis vectors $\{\hat{\boldsymbol{h}}_1, \hat{\boldsymbol{h}}_2, \hat{\boldsymbol{h}}_3\}$. The basis vector $\hat{\boldsymbol{h}}_1$ follows the anti-parallel direction to the solar array cg (S_c), $\hat{\boldsymbol{h}}_2$ defines the rotation axis of the hinge (with angle θ_s) and $\hat{\boldsymbol{h}}_3$ completes the basis. Each body has its own center of gravity (CG). This can be seen depicted in Figure 6.1.
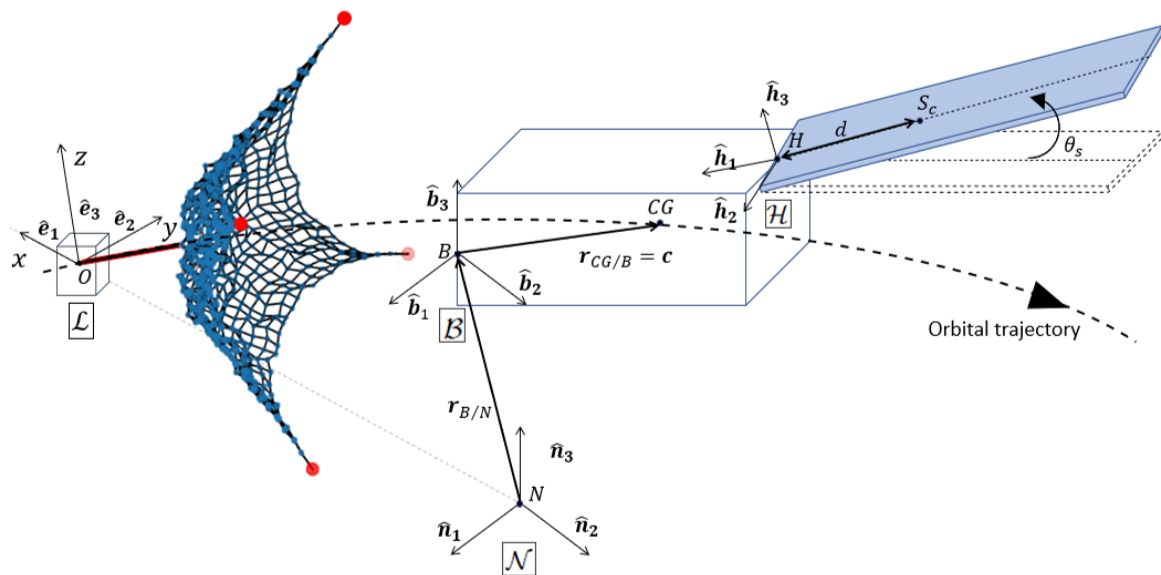
Figure 6.1: Visualisation of reference frames: the inertial frame $\mathcal{N}$, target body-fixed and hinge frames ($\mathcal{B}$ and $\mathcal{H}$) and chaser attached $O\text{-}xyz$ frame ($\mathcal{L}$). The main body, solar array and entire spacecraft centres of gravity are B_c, S_c and CG.

6.2. Impact of the Small Disturbance Assumption

The target's main body is assumed to not be influenced by the net. Its rigid body dynamics are therefore ignored in this study. This can be justified by using the principle of impulse and momentum [68]:

$$\sum_{i=1}^{N_i} m_i \boldsymbol{V}_i^- + m_d \boldsymbol{V}_d^- = \sum_{i=1}^{N_i} m_i \boldsymbol{V}_i^+ + m_d \boldsymbol{V}_d^+, \tag{6.1}$$

$$\mathbf{I}_d \boldsymbol{\omega}_d^+ = \mathbf{I}_d \boldsymbol{\omega}_d^- + \sum_{i=1}^{N_i} (\boldsymbol{r}_i \times j_i \hat{\boldsymbol{n}}_i), \tag{6.2}$$

where the superscripts "−" and "+" refer to pre- and post-impact conditions, $\hat{\boldsymbol{n}}_i$ is the normal unit vector of the ith contact plan, $\boldsymbol{V}_d$ and $\boldsymbol{\omega}_d$ are the debris linear and angular velocities, $\boldsymbol{V}_i$ and m_i are the ith node velocity and mass and lastly $\mathbf{I}_d$ and m_d are the debris inertia matrix and mass (MMOI), respectively.

As a first order estimate, one can approximate the net impact as a point mass where the impulse, j, is given by [68]:

$$j = \frac{-(e+1)V_r^-}{1/m_d + 1/m_{net} + \hat{\boldsymbol{n}} \cdot \left(\mathbf{I}_d^{-1}(\boldsymbol{r}_{i/d} \times \hat{\boldsymbol{n}}) \times \boldsymbol{r}_{i/d}\right)}, \tag{6.3}$$

where V_r^- is the net relative velocity, e is the coefficient of restitution and $\boldsymbol{r}_{i/d}$ is the net impact position.

By assuming a large and heavy space debris (large diagonal entries for $\mathbf{I}_d$ and m_d respectively):

$$j \approx -(e+1)V_r^- m_{net}. \tag{6.4}$$

Given this, with a typically high net mass and velocity range of $1-10$ kg and $0.5-25$ m/s, for a space debris, similar to the Jason series and Envisat (mass range of $500-8000$ kg), a high bound on the space debris post-impact relative speed would approximately be in the range $1.25 \cdot 10^{-4} - 0.5$ m/s. It is important to mention that this would be an overestimate due to the fact that, after the initial impact, the net would then wrap around the debris causing a recoil backwards (due to the bullets) lowering the gained speed. Additionally, if the impact is symmetric, the rotational impulse would be null (see Equation 6.2).

Thus, in this Thesis, the effect of the net impact on the target's overall dynamics can be initially neglected. This further confirmed as an assumption done in [15]. Given this, the effect of the net on the spacecraft dynamics should still be evaluated for the risk analysis. The latter will be done by a first order approximation in which the entire spacecraft system is assumed to be a rigid-body, with the second analysis including the relative dynamics of the large solar array.

6.3. Single Rigid-Body Dynamics

The rigid-body assumption itself consists on neglecting terms related to changes of mass and mass moment of inertia, and assuming that the body-fixed coordinate system has its origin at the center of mass. Given these assumptions, the translational and rotational motions are derived in this section in different reference frames to simplify the analysis.

6.3.1. Translation dynamics

Knowing that a net capturing scenario can be considered to be a typical rendez-vous between two spacecraft, the Clohessy-Wiltshire equations of relative motion can be used. These are defined w.r.t the LVLH O-xyz frame and are the linearisation of the general relative orbital motion of the target's EoMs w.r.t the chaser.

In order to present the dynamics it is essential to start from the general formulation of the EoMs in the $\mathcal{L}$ reference frame which are:

$$m_d \ddot{\boldsymbol{r}}_{\mathcal{L}}^d = \sum_{p=1}^{P} \boldsymbol{F}_{ext,p} - 2m_d \boldsymbol{\omega}_{\mathcal{L}/\mathcal{N}} \times \dot{\boldsymbol{r}}_{\mathcal{L}}^d - m_d \boldsymbol{\omega}_{\mathcal{L}/\mathcal{N}} \times (\boldsymbol{\omega}_{\mathcal{L}/\mathcal{N}} \times \boldsymbol{r}_{d/0}) - m_d \frac{\mathrm{d}}{\mathrm{dt}}(\boldsymbol{\omega}_{\mathcal{L}/\mathcal{N}}) \times \boldsymbol{r}_{d/0}. \tag{6.5}$$

where m_d is the space debris mass, $\boldsymbol{F}_{ext,p}$ refers to the pth orbital perturbation (aerodynamic, magnetic or net contact), $\boldsymbol{r}_{d/0}$ and $\dot{\boldsymbol{r}}_{\mathcal{L}}^{d}$ are the space debris (CG) relative position and velocity w.r.t the chaser (O) in the $\mathcal{L}$-frame. Lastly, $\boldsymbol{\omega}_{\mathcal{L}/\mathcal{N}}$ is the rotation rate of the $\mathcal{L}$-frame w.r.t $\mathcal{N}$, which by assuming a circular orbit is constant in time with magnitude ω_n. From Equation 6.5, one can identify the Coriolis, centrifugal and Euler inertial loads, in that order. In this case, as the orbit is assumed circular, the Euler term is null.

Thus, by eliminating the Euler term and linearising the EoMs (with the assumption that the relative distance both objects compared to the orbital radius is small) the translational EoMs in the $\mathcal{L}$-frame, the Clohessy-Wiltshire equations, can be written as follows:

$$\ddot{\boldsymbol{r}}_d = \omega_n^2 \begin{pmatrix} 3 \cdot x_d \\ 0 \\ -z_d \end{pmatrix} + 2 \cdot \omega_n \begin{pmatrix} \dot{y}_d \\ -\dot{x}_d \\ 0 \end{pmatrix} + \frac{1}{m_d} \cdot \sum_{i=1}^{N} \boldsymbol{F}_{c,i}, \tag{6.6}$$

where for simplicity the $\mathcal{L}$ subscript has been removed and x_d, y_d and z_d are the radial, along-track and cross-track components of $\boldsymbol{r}_{d/0}$.

6.3.2. Rotational dynamics and kinematics

For the rotational dynamics, it is essential to start from the definition of the space debris angular momentum $\boldsymbol{H}_d$ as:

$$\boldsymbol{H}_d = \mathbf{I}_d \boldsymbol{\omega}_d \tag{6.7}$$

where $\mathbf{I}_d$ is the debris inertia matrix and $\boldsymbol{\omega}_d$ is the the rotation of the body $\mathcal{B}$-frame w.r.t the inertial $\mathcal{N}$-frame (or $\boldsymbol{\omega}_{\mathcal{B}/\mathcal{N}}$). By taking the time derivative of Equation 6.7, one can obtain the rotational EoMs:

$$\frac{\mathrm{d}}{\mathrm{d}t}(\boldsymbol{H}_d) \mid_{\mathcal{N}} = \sum_{i=1}^{N} \boldsymbol{M}_{\mathrm{CG},i} \tag{6.8}$$

where $\boldsymbol{M}_{\mathrm{CG},i}$ refer to all the applied moments around the space debris center of gravity (CG).

In order to take the time derivative, the transport theorem is used:

$$\frac{\mathrm{d}}{\mathrm{d}t}() \mid_{\mathcal{N}} = \frac{\mathrm{d}}{\mathrm{d}t}() \mid_{\mathcal{B}} + \boldsymbol{\omega}_{\mathcal{B}/\mathcal{N}} \times (). \tag{6.9}$$

Combining the latter with Equation 6.8, results for a **rigid-body** spacecraft ($\mathrm{d}\mathbf{I}_d/\mathrm{d}t \mid_{\mathcal{B}} = 0$) in:

$$\mathbf{I}_d \dot{\boldsymbol{\omega}}_d + \boldsymbol{\omega}_d \times \mathbf{I}_d \boldsymbol{\omega}_d = \sum_i \boldsymbol{M}_{\mathrm{CG},i}, \tag{6.10}$$

As this study focuses on the net influence, all other disturbances (orbital, aerodynamic and solar radiation) are neglected. Given this, $\boldsymbol{M}_{\mathrm{CG},i}$ can be computed as:

$$\boldsymbol{M}_{\mathrm{CG},i} = \boldsymbol{r}_{i/\mathrm{CG}} \times \boldsymbol{F}_{c,i}, \tag{6.11}$$

where $\boldsymbol{F}_{c,i}$ and $\boldsymbol{r}_{i/\mathrm{CG}}$ are the ith net node contact force (see Chapter 5) and relative position w.r.t CG.

Lastly, a kinematic equation is required to relate the dynamic Euler equation and the physical orientation of the $\mathcal{B}$-frame with angles θ_X, θ_Y and θ_Z. Thus, the body rotation rate $\dot{\boldsymbol{\theta}}_d$ can be computed using $\boldsymbol{\omega}_d$ as:

$$\dot{\boldsymbol{\theta}}_d = \frac{1}{\cos(\theta_Y)} \begin{pmatrix} \cos(\theta_Y) & \sin(\theta_X)\sin(\theta_Y) & \cos(\theta_X)\sin(\theta_Y) \\ 0 & \cos(\theta_X)\cos(\theta_Y) & -\sin(\theta_X)\cos(\theta_Y) \\ 0 & \sin(\theta_X) & \cos(\theta_X) \end{pmatrix} \boldsymbol{\omega}_d + \frac{\omega_n}{\cos(\theta_Y)} \begin{pmatrix} \sin(\theta_Z) \\ \cos(\theta_Y)\cos(\theta_Z) \\ \sin(\theta_Y)\sin(\theta_Z) \end{pmatrix} \tag{6.12}$$

where $\dot{\boldsymbol{\theta}}_d$ is the derivative of the Euler angles θ_X to θ_Z (summarised as the $\boldsymbol{\theta}$-state) and hence correspond to the pitch ($\dot{\theta}_X$), roll ($\dot{\theta}_Y$) and yaw ($\dot{\theta}_Z$) rates.

6.4. Two Rigid-Body Dynamics

With the first order approximation done, the space debris object is now divided in two parts: main body and solar array(s), each assumed to be rigid bodies themselves connected by a hinge connection. As in reality the solar array will rotate and add to the angular momentum of the overall system, there exists therefore a coupling between the rotational motion of the satellite and its large solar array(s). The goal of this section is to briefly present the new EoMs which describe this two-body system in order to later see the effect of the net contact dynamics on the solar array.

6.4.1. Equations of Motion for two rigid-body systems

The two bodies are assumed to be joined by a joint connection, here modelled as torsional-damping system, which allows the solar array to rotate only in one direction by an angle θ_s (see Figure 6.1). This can be confirmed by literature [36, 78], in which the solar array Primary Deployment Mechanism (PDM) has been assumed to be functional. In order to model the dynamics of the solar array, a similar methodology as presented in [2] is used, in which the EoMs of the main body and solar array are coupled to each other.

The combined body system dynamics are described by [2]:

$$
\begin{pmatrix} [\mathbf{A}] & [\mathbf{B}] \\ [\mathbf{C}] & [\mathbf{D}] \end{pmatrix} \begin{pmatrix} \ddot{\boldsymbol{r}}_{B/N} \\ \dot{\boldsymbol{\omega}}_d \end{pmatrix} = \begin{pmatrix} \dot{\boldsymbol{v}}_{Trans} \\ \dot{\boldsymbol{v}}_{Rot} \end{pmatrix},
\tag{6.13}
$$

where one can identify that the first row mainly relates to the translational dynamics with the relative body acceleration $\ddot{\boldsymbol{r}}_{B/N}$ and the inertial forces, $\dot{\boldsymbol{v}}_{Trans}$, experienced by the satellite. The second row mainly focuses on the satellite's rotational dynamics expressed by the rotational acceleration $\dot{\boldsymbol{\omega}}_d$ and the inertial torque load $\dot{\boldsymbol{v}}_{Rot}$. The expression of matrices $[\mathbf{A}]$, $[\mathbf{B}]$, $[\mathbf{C}]$ and $[\mathbf{D}]$, as well as the inertial acceleration $\dot{\boldsymbol{v}}_{Trans}$ and $\dot{\boldsymbol{v}}_{Rot}$ can all be found in Appendix A.

In this work, the coupling between the rotational and translational dynamics is removed by using the CG instead of the origin of the body-fixed frame $\mathcal{B}$. This still results in a coupling between the solar array and spacecraft rotational dynamics, however it removes the added and unnecessary complexity related to the translational motion.

By performing the aforementioned transformation, the main body rotational dynamics can be written in the same manner as Equation 6.10, leading to [2]:

$$
\mathbf{I}_d \dot{\boldsymbol{\omega}}_d + \boldsymbol{\omega}_d \times \mathbf{I}_d \boldsymbol{\omega}_d + \frac{\mathrm{d}}{\mathrm{d}t}(\mathbf{I}_d)|_{\mathcal{B}} \boldsymbol{\omega}_d + (I_{h_2} \hat{\boldsymbol{h}}_2 + m_{SA}\, d \cdot \boldsymbol{r}_{S_c/C} \times \hat{\boldsymbol{h}}_3) \ddot{\theta}_s +
$$
$$
\dot{\theta}_s \boldsymbol{\omega}_d \times (I_{h_2} \hat{\boldsymbol{h}}_2 + m_{SA}\, d \cdot \boldsymbol{r}_{S_c/C} \times \hat{\boldsymbol{h}}_3) + \dot{\theta}_s^2\, m_{SA}\, d \cdot \boldsymbol{r}_{S_c/C} \times \hat{\boldsymbol{h}}_1 = \sum_i \boldsymbol{M}_{\mathrm{CG},i}, \tag{6.14}
$$

where I_{h_j} is the solar array MMOI around $\hat{\boldsymbol{h}}_j$, m_{SA} is the solar array mass, d is the solar array moment arm, $\boldsymbol{r}_{S_c/C}$ is the relative position of the solar array cg w.r.t the spacecraft cg and last but not least, $\dot{\theta}_s$ and $\ddot{\theta}_s$ are the solar array angular velocity and acceleration. Additionally, one can observe that the previously assumed null term $\mathrm{d}(\mathbf{I}_d)|_{\mathcal{B}}/\mathrm{d}t$ is present and refers to the MMOI local derivative caused by the solar array relative motion.

Having presented the main body dynamics, it is now essential to show the solar array EoM. The solar array angular motion (represented by θ_s) can be found by solving [2]:

$$
\ddot{\theta}_s = \boldsymbol{b}_{\theta_s} \cdot \dot{\boldsymbol{\omega}}_d + \frac{1}{(I_{h_2} + m_{SA}\, d^2)} \left[-\kappa\, \theta_s - d_\theta\, \dot{\theta}_s + \sum_i \boldsymbol{M}_{H,i} \cdot \hat{\boldsymbol{h}}_2 \right.
$$
$$
\left. + (I_{h_3} - I_{h_1} + m_{SA}\, d^2)\omega_{h_3}\omega_{h_1} - m_{SA}\, d\, \hat{\boldsymbol{h}}_3 \cdot \left(\boldsymbol{\omega}_d \times (\boldsymbol{\omega}_d \times \boldsymbol{r}_{H/C}) \right) \right], \tag{6.15}
$$

where $\boldsymbol{b}_{\theta_s}$ is the coupling term (see Appendix A), κ and d_θ are the hinge stiffness and damping, ω_{h_j} is the projection of $\boldsymbol{\omega}_d$ on the $\hat{\boldsymbol{h}}_j$-direction and $\sum_i \boldsymbol{M}_{H,i}$ is the total dynamic moment around the hinge point H experienced by the solar array.

6.4.2. Hinge dynamic loading

Lastly, given that the solar array is assumed to be fixed around the other two directions, the hinge will experience two loading torques (L_{H_1} and L_{H_3}) in the direction of basis vectors $\hat{\boldsymbol{h}}_1$ and $\hat{\boldsymbol{h}}_3$. These can be computed using the torques around the solar array (denoted here as L_{s_i}) as [2]:

$$L_{s_1} = I_{h_1}(\dot{\boldsymbol{\omega}}_d \cdot \hat{\boldsymbol{h}}_1) + (I_{h_3} - I_{h_2})(\omega_{h_2} + \dot{\theta}_s)\omega_{h_3}, \tag{6.16}$$

$$L_{s_3} = I_{h_3}(\dot{\boldsymbol{\omega}}_d \cdot \hat{\boldsymbol{h}}_3) + (I_{h_2} - I_{h_1})(\omega_{h_2} + \dot{\theta}_s)\omega_{h_1}. \tag{6.17}$$

Using (6.16), (6.17) and back-solving (6.15) for L_{s_2}, the net load around the hinge point, $\boldsymbol{L}_H$ can be computed using the torque of solar array around its cg, $\boldsymbol{L}_S$ [2]:

$$\boldsymbol{L}_H = \boldsymbol{L}_S + \boldsymbol{r}_{S/H} \times (m_{SA}\ddot{\boldsymbol{r}}_{S_c/N}), \tag{6.18}$$

where $\ddot{\boldsymbol{r}}_{S_c/N}$ is the inertial acceleration experienced by the solar array around its point S.

Finally, these loads can be used to investigate if the maximum loads of the specific hinge in question have been exceeded and hence if failure at the connection point has occurred. The maximum moment, $M_{spr_{max}}$, related to the torsional spring can be computed as [1]:

$$M_{spr_{max}} \sim K_R \frac{\pi d_{spr}^3 \sigma_{all}}{32K_0}, \tag{6.19}$$

with $\sigma_{all} = 1.206$ GPa [1] being the structural strength of the spring, the diameter of the spring d_{spr} can be assumed to be around 4 mm [1], K_0 is the spring correction factor around 1.444 [1] and $K_R \sim 3 \cdot 10^5 - 6 \cdot 10^5$ is the added factor that takes into account the real size of the solar array (compared to the design performed in [1]). This results in a range $M_{spr_{max}} \sim 1.7 - 3.4$ kNm. The hinge will also be loaded with out-of-plane bending moments. As there is little to nearly no literature on the latter, it will be assumed that $M_{h_{max}}$ is a quarter of the maximum spring torque. This is due to the fact that the spacecraft hinge was not designed to withstand large loads in those directions as discussed in (M. Kroon, Priv. Comms.), seen in [86] and as confirmed by the deployment sequence shown in Figure 2.11.

6.5. Antenna Vibrational Dynamics

The third largest flexible appendage of Envisat is its Ka-band antenna. Whereas, it is still essential to see if the latter breaks during its loading due to impact vibrations, the two-rigid-body dynamics model is not necessary. A simple impact-vibrational model can be used for the Ka-band antenna in order to see if the latter breaks during contact.

The simplest possible dynamical model is the SDOF (Single Degree of Freedom) spring-damper-mass model. The entire mass of the beam is assumed to be concentrated at its end, and the flexural behaviour is simulated with a spring and damper connector. This beam simplification process can be visualised in Figure 6.2.
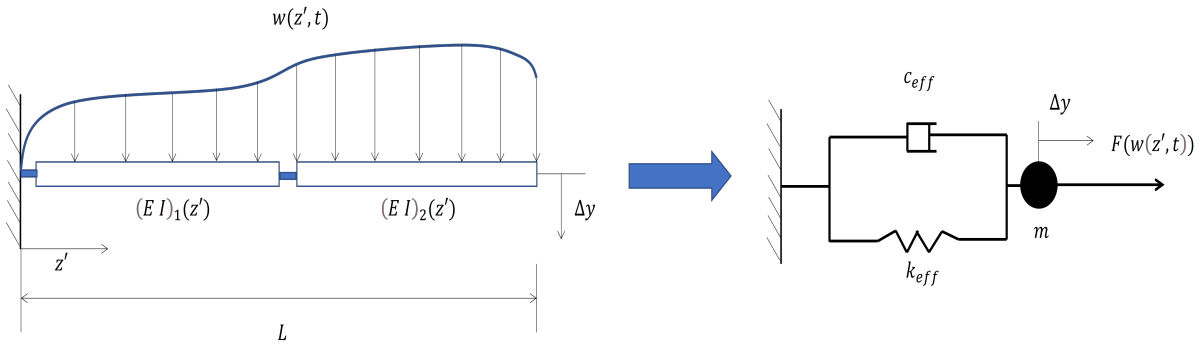
Figure 6.2: Simplified scheme showing approximation process from already simplified representation of a composite beam with loads $w(z', t)$ to a SDOF spring-damper-mass system with effective stiffness, damping and equivalent force $F(w(z', t))$.

6.5.1. Basic principles

Any loading configuration, creating a small displacement Δy can be written using Newton's second law as:

$$\Delta \ddot{y} + \frac{c_{eff}}{m} \Delta \dot{y} + \frac{k_{eff}}{m} \Delta y = \frac{F(t)}{m} \quad (6.20)$$

where c_{eff} and k_{eff} are the effective damping coefficient and stiffness of the beam, m is the mass of the beam and $F(t)$ is the load applied to the beam. In the specific case of net capturing, this load is the impulse forcing caused by the net-target momentum exchange. Lastly, Equation 6.20 assumes that the wall is at rest, which means that the relative speed of the target main body is not taken into account. This is assumed to be valid for the antenna case, as the net capturing impact is a small disturbance for the entire satellite which would not cause an excessive tumbling response (see section 6.2).

6.5.2. Spring and damping coefficients

Following the basic principles, a methodology to compute k_{eff} and c_{eff} is required. Using the first mode of the natural frequency (f_1) or the fundamental frequency, the spring constant is obtained using [49]:

$$k_{eff} = (2\pi f_1)^2 m. \quad (6.21)$$

Secondly, to compute c_{eff}, the relation is as follows:

$$c_{eff} = 2\zeta \sqrt{m k_{eff}}, \quad (6.22)$$

where ζ is the damping ratio of the beam. This ratio is usually obtained experimentally using the half-bandwidth method [4]. However, for the purpose of this study, these will be chosen. For the solar panels themselves without any rigid connection, it can be assumed to be very small as shown to not be modelled in [49]. The latter is also confirmed by Wijker in [89], which mentions that typical spacecraft structures have low ratios of $2 - 10$ %. Wijker further mentions that structures to be connected to hinges (such as solar panels) should be designed with $\zeta = 2 - 3$ %, whereas other appendages (such as antennas) have on average $\zeta = 0.2 - 0.3$ %. Given these recommendations, it is decided to choose **2.5**% and **0.25**% for the solar panels and antennas, respectively.

6.5.3. Antenna modelling

Given the basics and the short-lived nature of the impact, the input force will be modelled as square pulse input with maximum F_{max} and duration Δt_{imp}. These two parameters will be discussed in Chapter 5. The scenario of interest can be found visualised in Figure 6.3.
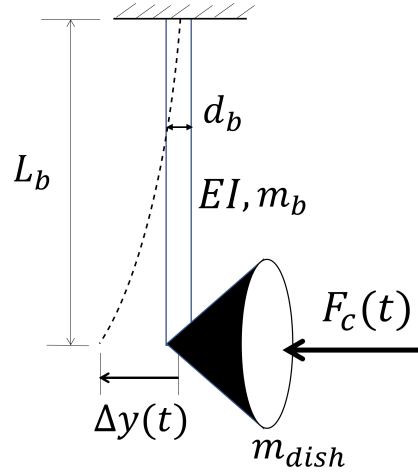
Figure 6.3: Scenario of impulse force input on L_b-long (Ka band-)antenna tip with beam and dish masses m_b and m_{dish}.

The antenna dish is assumed to be a point mass with the beam structure of the antenna assumed to have a circular cross-section with diameter d_b. Due to the lacking material knowledge in the literature, a material must be chosen as reference. Two potential candidates for the Ka-band antenna are: carbon reinforced polymer (CFRP) as done in industry [91], or a combination of a typical Aluminum alloy with a Titanium alloy (TiGAI4V) used for the antenna's deployment mechanism [67]. The properties for both materials are summarised in Table 6.1.

To determine k_{eff}, the structure can be assumed to be a clamped Euler beam of which the natural n^{th} mode frequency, f_n can be written as:

$$f_n = \frac{(\lambda_n L)^2}{2\pi}\sqrt{\frac{EI}{\rho\,A\,L^4}},\tag{6.23}$$

where I and A are the second moment of inertia and area of the cross-section, ρ is the density and λ_n is the eigenvalue natural frequency computed as the roots of $\cosh(\lambda_n L)\cos(\lambda_n L) = -1$.

Table 6.1: CFRP fiber and TiGAI4V material properties [54, 83]

Property	CFRP	TiGAI4V
Ultimate tensile Strength (fibre direction), σ_{ult} [GPa]	3.5	0.95
Ultimate Strength (perpendicular direction), $\sigma_{ult_\perp}$ [GPa]	0.20	0.95
Ultimate compression Strength, $\sigma_{c_{ult}}$ [GPa]	1.05	1.07
Ultimate shear strength, τ_{ult} [MPa]	$50 - 140$	550
Elastic Tensile Modulus, E [GPa]	250	113.8
Maximum elongation, ϵ_{ult} [%]	1.5	0.83
Density, ρ [kg/m^3]	1800	4420

In order to check if breaking-off occurs, the maximum allowable deflection that occurs at failure can be computed geometrically with the perpendicular-to-fibre-direction ultimate strength $\sigma_{ult_\perp}$:

$$\Delta y_{fail} \sim \frac{\sigma_{ult_\perp} L_b^2}{3E\,d_b/2}.\tag{6.24}$$

Lastly, to simulate the vibrational behaviour of the antenna, the mass and second moment of area are required. The total mass of the structure can then be computed as:

$$m = m_{dish} + \rho\cdot\pi\frac{d_b^2}{4}\cdot L_b,\tag{6.25}$$

with the second moment of inertia (in all directions) I being:

$$I = \pi \frac{d_b^4}{64}. \tag{6.26}$$

6.6. Structural Modelling

There is a range of different structural models, varying in complexity and implementation. Due to the multi-disciplinary nature of this Thesis, simple structural models will be chosen by first identifying the weakest locations of failure, computing the structural loads and lastly by comparing them with critical values.

6.6.1. Identifying weak locations

When identifying weak locations, it is important to seek for long, fragile or small sub-structures. As these were not designed to withstand considerable loads, any contact load from a capturing net could result in structural failure.

Solar panel structure

For the solar panel, two main locations are found using the solar panel layout represented in Figure B.1. These are mainly: the main deploying hinge found at the root of the entire solar panel, and the PIP interface between the secondary hinge and panel. The latter is considered to withstand approximately $200 - 1000$ Nm in out-of-plane bending (M. Kroon, Priv. Comms.), with the main hinge strength being already described in section 6.4 having an equivalent torsional spring constant of 5000 Nm/rad (M. Kroon, Priv. Comms.).

Antenna structure

For the antenna, when observing Figure 2.7, one can see that the dish-beam interface and the antenna hinge can be seen as potential sights of failure. The first location is identified as risky due to its thin structure (48.6 mm-radius) maintaining the dish in place. The second sight is justified due to the 2 m-long moment arm in which out-of-plane bending stresses could lead to hinge failure.

ASAR antenna structure

The second largest structure of the Envisat was identified to be the ASAR antenna in subsection 2.4.2. As one can observe from Figure 2.9, this antenna is rigidly connected to the satellite's main body with eight joints (four on each side). This means that the load will mainly be distributed over these joints.

For this study, it will be assumed that the external forces are equally distributed over the eight connections. However, due to the lack of literature on these joints, in terms of geometry, material and structural strength properties, and the fact that all these joints will share an eighth of the external forces, this structure is not expected to fail from the net impact and wrapping process. This hypothesis is emphasised by how critical the structural integrity is for the two other flexible appendages compared to this one. In fact, the ASAR antenna is 1.5 m wide by 0.156 m thick (see Table 2.3), compared to the minimum and maximum beam diameters of the Ka-band antenna (48.60 mm and 146.0 mm) and the fragility of the PIP interface and 44.0 mm-diameter of the solar array connecting beam. Given this, it is decided to focus on the solar array and Ka-band antenna structural analysis, with the ASAR antenna analysis being recommended as future work to confirm the choice made in this study.

6.6.2. Structure local reference system and major assumption

An important first step in modelling a structure is to define the reference systems and fully characterise it, such that the loads can be translated to stress in the most realistic manner.

First, it is essential to define the local coordinate system of the space debris structure which can be found visualised in Figure 6.4.
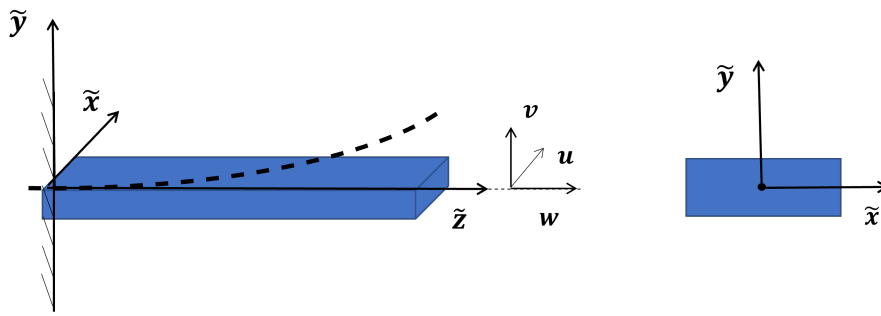
Figure 6.4: Beam element and local coordinate system, $\tilde{\mathcal{B}}$, used with positive deflections (u, v, w) directions and positive bending neutral axis. The left part represents the cross-section of the beam with its $\tilde{x}\tilde{y}$-coordinate system.

Secondly, as a preliminary step it is essential to make a few assumptions to simplify the analysis. The solar panels and antennas are assumed to be Bernoulli-Euler beams which assume that all perpendicular cross-sections are geometrically unaltered ("plane sections remain plane") and that all angular deformations are small. The latter assumptions work well when the beam length is higher than the cross-sectional dimensions, which is clearly the case of the solar array yoke and antenna beams. Having defined the aforementioned reference frame and stated the assumptions, the different types of structural loadings will be presented.

6.6.3. Structural forces and moments

In order to compute the stresses experienced by the structure, it is first essential to compute the structural loads. These can be computed by making a virtual "cut" in the structure and solve for the new unknown structural loads on the basis of the same system dynamics performed in the previous section. A visualisation of this process for the specific example of the solar array can be found below in Figure 6.5 with the identified weak locations (see subsection 6.6.1).
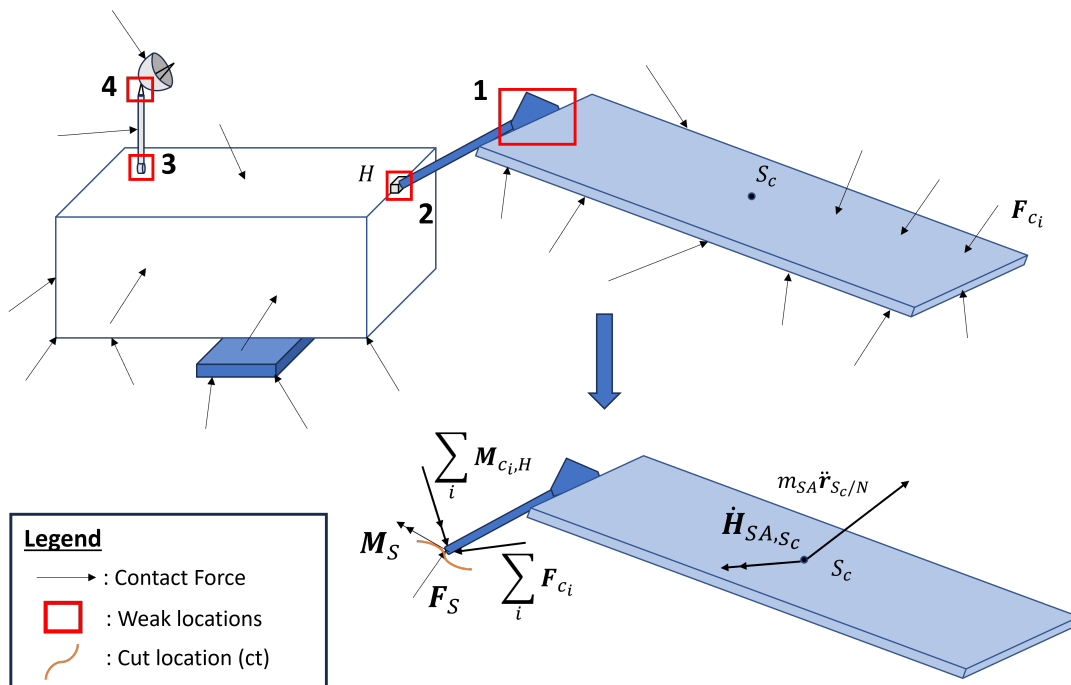
Figure 6.5: Overview of the identified weak locations of the Envisat satellite and visualisation of structural load computation strategy (with the solar array concrete example at weak location 2).

For the forces, one can obtain the two shear and normal loads, and in terms of moments, two bending

moments and one twisting torque can be found. By "adding" these unknowns, one can compute the structural force and moment $\boldsymbol{F}_S$ and $\boldsymbol{M}_S$ using:

$$\boldsymbol{F}_S = m_j \ddot{\boldsymbol{r}}_{j_c/N} - \sum_i \boldsymbol{F}_{c,i}, \tag{6.27}$$

$$\boldsymbol{M}_S = \dot{\boldsymbol{H}}_{j,ct} - \sum_i \boldsymbol{M}_{c_{i_{ct}}}, \tag{6.28}$$

where j refers to one of the single-rigid bodies (the satellite, the solar panel or the antenna), j_c is the cg of the latter, $\dot{\boldsymbol{H}}_{j,ct}$ is the derivative of the angular momentum of the j-system around the cut location ct, and lastly $\boldsymbol{M}_{c_{i_{ct}}}$ is the moment related to the contact force $\boldsymbol{F}_{c_i}$ around the cut location ct. In the case where the system can be assumed to be in static equilibrium, $\ddot{\boldsymbol{r}}_{j_c/N}$ and $\dot{\boldsymbol{H}}_{j,ct}$ are null, and the structural force and moment simply equal to the total contact forces and moments around that location.

6.6.4. From forces to stresses
Given the methodology to compute the structural loads experienced by the two flexible appendages and their weak locations, it is now possible to present stress loadings present in this capturing scenario.

Bending loading
The first and major type of loading all beams will experience is bending. This occurs from impact and then gradually decreases as the wrapping of the net progresses. However, as the net exerts forces onto the structure, these can be translated to bending moments and thus resulting in bending stresses σ_b. The relationship of σ_b within the $\tilde{\mathcal{B}}$-frame ($\tilde{x}$, $\tilde{y}$ and $\tilde{z}$ are denoted as x, y, and z to simplify heavy notation) is [53]:

$$\sigma_b(x, y, z) = \frac{(M_x I_{yy} - M_y I_{xy})y + (M_y I_{xx} - M_x I_{xy})x}{I_{xx}I_{yy} - I_{xy}^2}, \tag{6.29}$$

where M_x, M_y are the internal bending moments in the $x-$ and $y-$direction of the local coordinate system and I_{xx}, I_{yy} and I_{xy} are the area moments of inertia of the cross-section. Given a symmetric structure, such as a solar panel or the circular cross-sections of the antenna and yoke beams, $I_{xy} = 0$. This then simplifies the equation to:

$$\sigma_b = \frac{M_x}{I_{xx}}y + \frac{M_y}{I_{yy}}x \tag{6.30}$$

If the applied loading results in a bending stress above the ultimate stress, $\sigma_b \geq \sigma_{ult}$, then the structure is assumed to have failed at that cross-section location.

Combined shear loading
As the net starts wrapping around the space debris, the structure could also experience high torques and fail due to an excessive shear stress τ. The torque is the third component in the $z-$direction of the applied moment $\boldsymbol{M}_i$.

For solar panels, thin wall approximations can be applied to the solutions for a plate, resulting in a maximum shear stress as follows [53]:

$$(\tau_{max})_{plate} = \frac{3M_T}{st^2} \tag{6.31}$$

where M_T is the applied torque, s and t are the width and thickness of the plate.

The second vulnerable structure type is antennas. Simple antenna structures can be modelled as thin circular shafts. For these, the shear stress becomes:

$$(\tau)_{circ} = \frac{M_T \rho}{J_T} \tag{6.32}$$

where ρ and J_T are, respectively, the radial distance and torsional area moment of inertia of the shaft.

To torsion, one must not forget about simple shear stress due to shear forces, P_{xy}, in the $xy-$plane. Indeed, the structure is loaded with many different types of loads, which is known as "combined loading". Hence, imagining that the structure could survive all the loads on their own, it could fail when these are combined. Thus, the maximum shear stress can be computed using Equation 6.31 or Equation 6.32 with an added term P_{xy}/A. As for bending, if the maximum shear stress experienced by the structures is above the ultimate value, τ_{ult}, shear breaking occurs.

Compressive and buckling loading

During the aforementioned wrapping phase, the net can also cause high compressive forces, specifically onto the solar panel and SAR antenna. In fact, as the net fully wraps around the target with the bullets retracting backwards, the tension forces at the ends of the appendages orient in such a manner that the appendages are compressed. Due to the latter, the solar panel and/or SAR could fail due to compression or buckling.

The compression stress, σ_c, can be computed (with its constraint) as:

$$\sigma_c = \frac{P_z}{A} \leq \sigma_{c_{ult}}, \tag{6.33}$$

where P_z is the compression load and A is the cross-sectional area of the appendage. A specific phenomenon that occurs during compression is buckling which for a free-clamped appendage or plate happens for a critical stress, σ_{cr} as:

$$\sigma_{cr} = \frac{\pi^2 (EI)_{eff}}{L_e^2 \cdot A}, \tag{6.34}$$

with $(EI)_{eff}$ being the flexural rigidity of a beam or plate and L_e being the effective buckling length ($L_e = 2L$). This criterion can also be considered to predict failure due to the high instability of buckling. As the structure buckles, its structural strength is highly reduced and hence failure could occur thereafter.

6.6.5. Accounting for existing damage

Relevance

As space debris are usually damaged, partially destroyed or even fragmented spacecraft structures, it is important to account for existing damage. Even for complete non-operational satellites, such as the Envisat, there is an existing chance of micro-debris impact with its solar array or SAR antenna, resulting in cracks.

Damage itself comes in many forms, such as cracks, voids or discontinuities within the spacecraft structure. A typical example of cracks in spacecraft structures are the previously mentioned cracks on solar panels caused by micro-debris hyper-velocity impacts. As this probability of collision is high for objects with projectile diameters above 1 mm, for collisions with an impact velocity average in the range $10 - 12$ km/s [58], these can result in craters (see Equation 2.5) of around $0.007 - 2.0$ m. With these sizes, the diameter-to-width ratio for the Envisat can reach 40% and high reduction in structural strength.

Furthermore, if the crack failure condition is reached, the crack propagates with a velocity being a fraction of the elastic wave propagation speed $C_V = \sqrt{E/\rho}$ and can reach values from 1000 to 1400 m/s (for steel) [99]. Hence, the severity of fracture confirms the necessity to include this simplified consideration into the structural model.

Least but not last, this aspect has not been found included in the literature when analysing the impact of the capturing tool on a damaged structure in the context of ASDR missions.

Basics and Failure Modes

The effect of existing damage in a loaded structure can be modelled using the basic principle of fracture mechanics. A basic conceptualisation of the effect of cracks or voids can be found using a simplified

1D model for ductile materials [97]:

$$\sigma_{eff} = \frac{\sigma}{1 - D} \tag{6.35}$$

where the effective stress, σ_{eff} is higher than σ due to the presence of a reduced surface area, A, represented by the factor $D = A_{eff}/A$. For ductile materials, failure can therefore occur due to crack growth or by void coalescence in which connections between different voids occur. It is crack propagation which will be the main focus of this study.

For a damaged structure, there are three main modes of crack loading which are [31]:

Mode I: Crack propagation or opening due to tensile loading pulling damaged surfaces apart.

Mode II: Shear crack propagation due to crack surfaces sliding (in the main crack dimension direction).

Mode III: Out-of-plane shear crack propagation due to crack surface sliding (perpendicular to main crack dimension direction).

The most relevant crack propagation mode in engineering applications is Mode I [31]. This is due to the fact that it shows the highest level of severity during the breaking of a structure and that other modes re-orient themselves to become Mode I during crack propagation.

Residual strength

To translate the presence of cracks in this model, the concept of stress concentrations K and intensity K_σ is used. These occur at the crack ends which further reduce the structural strength of the object. If the failure condition $K_\sigma \geq K_{IC}$ is reached, where K_{IC} is the fracture toughness, fracture failure occurs. This can be translated to a critical stress threshold, called residual strength as:

$$\sigma_{cr_K} = \frac{K_{IC}}{Y\sqrt{\pi\tilde{a}}}, \tag{6.36}$$

where $\tilde{a}$ is the crack length and Y is the geometry function. The latter is a function of the geometry of the crack and also the loading applied. The relevant equations for Y, especially focused on bending, are found summarised in [82].

For sandwich composite structures, it is useful to model the crack as a hole (Equivalent Hole Model). The theoretical computation of stress concentrations is usually performed by evaluating the material's notch sensitivity [60]. Typical composite material behaviour exhibit partial notch sensitivity. Insensitive corresponds to perfectly ductile materials (for e.g. metals), whereas perfectly brittle materials are referred to notch sensitive. This means that composite residual strength is between $(\sigma_n/\sigma_{un})_{ins}$ and $(\sigma_n/\sigma_{un})_s$ [40, 64], computed as:

$$\left(\frac{\sigma_n}{\sigma_{un}}\right)_{ins} = 1 - \frac{d}{b} \tag{6.37}$$

$$\left(\frac{\sigma_n}{\sigma_{un}}\right)_s = \frac{1 - \frac{d}{b}}{2 + \left(1 - \frac{d}{b}\right)^3} \tag{6.38}$$

where σ_n and σ_{un} are the notched and unnotched strengths, d is the equivalent diameter hole associated to the crack and b is the plate width. An estimator of the residual strength is therefore taken as the simple average between the two limits, which matches results for CFRP plates from [40, 64]. This is visualised in Figure 6.6.
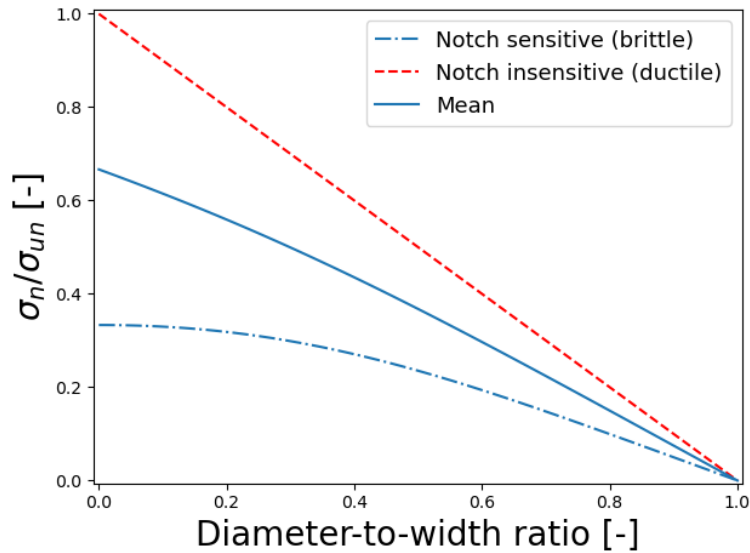
Figure 6.6: Perfectly brittle and ductile limits of the strength reduction, with the mean "estimator" of strength loss.

The aforementioned material would match the case of the Envisat solar panel and ASAR antenna [25]. Furthermore, as it is known that the thin sheets of fibre-reinforced polymers carry the majority of the stress, the aforementioned relations are found to be adequate to model the presence of a crack.

Finally, the following condition for failure, on the applied stress σ is added to the structural model:

$$\sigma(x_a, y_a, z_a) \geq \sigma_{ult_n}, \tag{6.39}$$

where σ_{ult_n} is the notched ultimate strength and (x_a, y_a, z_a) is the damage center location.

6.6.6. Secondary space debris size

Having defined the conditions for failure to occur, it is now essential to define a first order preliminary assessment of the potentially resulting secondary space debris. This will be done by taking the location (x_{br}, y_{br}, z_{br}) in which the stresses are higher or equal to the maximum allowable critical stresses. As this is a first order evaluation, it is assumed that the presence of a crack only locally affects the strength of the appendage and hence the maximum allowable stress will slightly vary throughout the structure.

With this computed location, the structure is assumed to fail in a straight line with a cross-section perpendicular to the stress principle direction. Two parts would then be created in which the separated piece from the spacecraft main body is defined as the secondary space debris with its associated dimensions being of interest. In the case of failure due to the presence of existing damage, it is assumed that the crack propagates in a straight line which corresponds to the direction of the principle stress axis.

7

Dynamic Investigation of Net Capturing - Results and Discussion

A specific capturing scenario of the Envisat with the capturing net has been simulated which will be presented and discussed in this chapter.

7.1. Simulation inputs

The simulation inputs of the capturing scenario with the Envisat (attitude configuration A, see subsection 2.8.2), can be found respectively in Table 7.1 and Table 7.2. The time step used is $5 \cdot 10^{-5}$ s and the initial net's CM deviations w.r.t the Envisat's geometric center are zero.

Table 7.1: Simulation inputs related to net dynamics.

Simulation input	Symbol	Value
Mesh length	l_{0_q}	0.8824 m
Net side length	L_{net}	30 m
Average thread stiffness	k_q	62308.25 N/m
Average thread damping	c_q	1.58 N/(m/s)
Bullet mass	m_b	1.786 kg
Ejection velocity	V_e	20 m/s
Mock-up Envisat reduction factor	f_{Env}	0.75

Table 7.2: Main simulation inputs related to contact detection and dynamics.

Simulation input	Symbol	Value
Thread radius	R_q	1 mm
Bullet radius	R_b	1 cm [68]
Static friction coefficient	μ_s	0.19 [15]
Dynamic friction coefficient	μ_k	0.152 [15]
Material constant	n	1.5 [15, 68]
Contact stiffness	k_n	$1.622 \cdot 10^8$ N/m$^{1.5}$
Experimental damping constant	α	0.05 [15]
Contact damping	d_n	$1.216 \cdot 10^7$ N/(m$^{2.5}$s)
Maximum penetration	δ_{max}	$1.74 \cdot 10^{-4}$ m

7.2. Net Capturing Process
In this section, the success of the capturing process itself will be checked.

7.2.1. Visualisation of the net impact and wrapping
The first step in analysing the net capturing process, the capturing sequence itself, projected in the xz-plane ($\mathcal{L}-$frame), can be visualised in Figure 7.1.
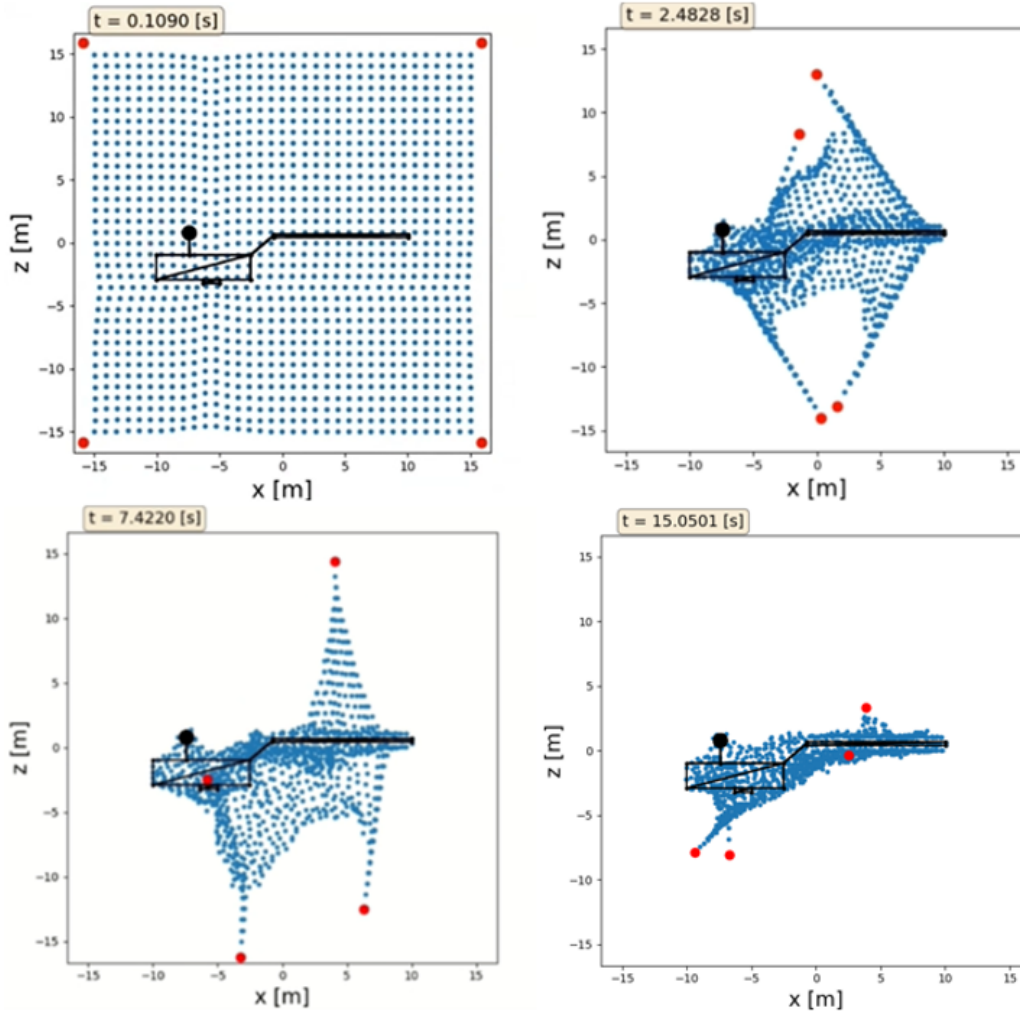
Figure 7.1: Mock-up Envisat net capturing sequence (with time references) with frontal impact of $V_{net} = 20$ m/s.

From Figure 7.1, one can observe that the impact occurs around $t \approx 0.1$ s at the ASAR antenna. The first cycle of the wrapping process finishes at $t \approx 2.4$ s with the entire Envisat wrapped around the net. The following cycle ends at $t \approx 5$ s, with the next cycle resulting in an impact between a bullet and the ASAR at $t = 7.422$ as can be observed in Figure 7.1. Lastly, the simulation ends at $t = 15.10$ s, with the Envisat mock-up being entirely wrapped with two bullets being nearly at rest.

7.2.2. Net dynamic properties
As performed throughout the existing literature on net capturing, one can verify the success of the capturing process using the net mouth index (Figure 7.2a), net depth (Figure 7.2b) and Center-of-Mass (CM) dynamic properties (Figure 7.3). The net mouth index is the ratio between the net mouth area, $S(t)$, w.r.t L_{net}^2. In the addition to these properties, it is suggested to also verify that no net breaking occurs. For the latter, the maximum tension experienced by the net will be checked in Figure 7.4.
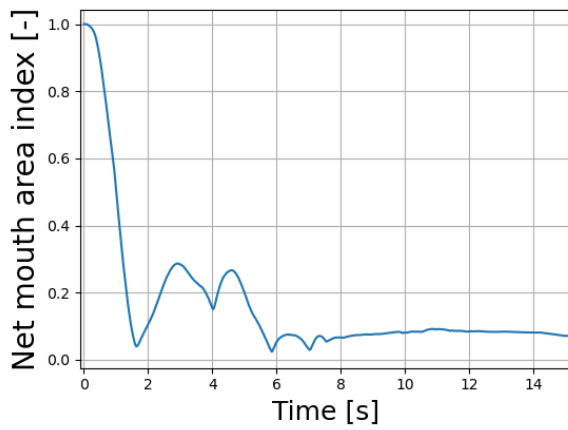
(a) Net mouth index $(S(t)/L_{net}^2)$ as a function of time for the capture of the mock-up Envisat satellite.
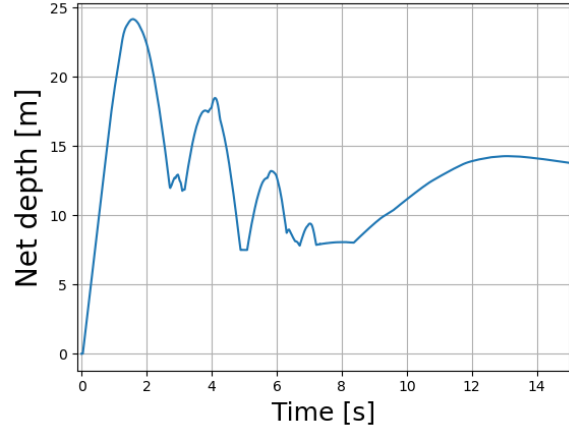
(b) Net depth as a function of time for the capture of the mock-up Envisat satellite.

Figure 7.2: Geometrical net dynamics from a frontal net impacting with $V_{net} = 20$ m/s.
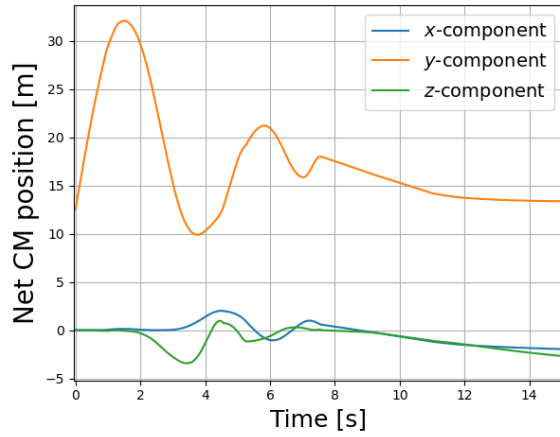
(a) Net CM position as a function of time for mock-up Envisat capture.
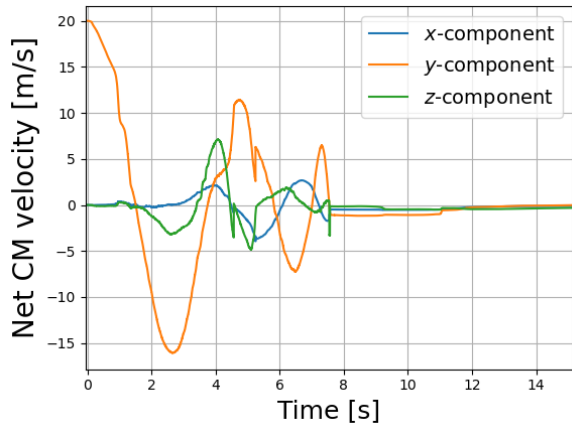
(b) Net CM velocity as a function of time for mock-up Envisat capture.

Figure 7.3: Net CM dynamics from a frontal net impacting with $V_{net} = 20$ m/s.
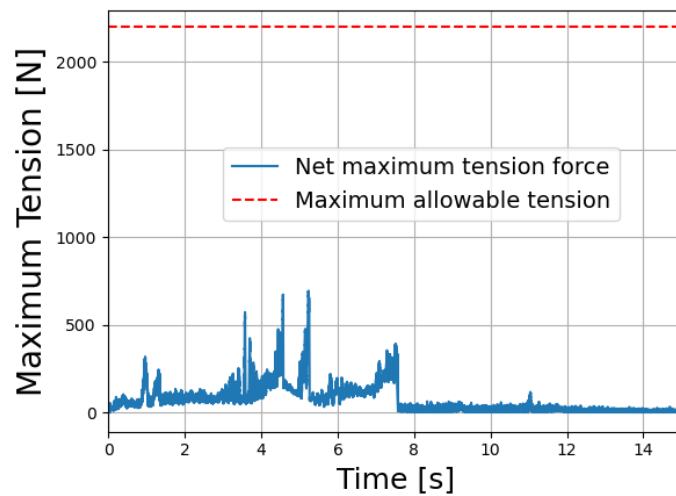
Figure 7.4: Maximum net experienced tension force from a frontal net impacting with $V_{net} = 20$ m/s.

To begin the net dynamics analysis, it can be observed in both Figure 7.2a and Figure 7.2b, that there are three main cycles of the wrapping process each lowering the net mouth and depth indices. In contrast however to the stabilising of the net mouth index, revealing the success of the wrapping process, the net depth shows to increase again from $t = 8.5$ s. This is due to the bullet impact with the ASAR at $t \approx 7.42$ s, which results in a bouncing effect which seems to damp out at the end of the simulation. This is confirmed and cross-verified by the dynamics results of the net CM. The identified abrupt change in velocity at $t \approx 7.42$ s, and position slope confirm the bullet impact event. Furthermore, the settling of the CM velocity can be observed to be near 0 m/s from $t = 12$ s (Figure 7.3b). This confirms that the driving bullets are loosing velocity and that the system is approaching a rest configuration. Last but not least, the successful wrapping of the Envisat is also observed in the settling of the net CM position components which seem to converge to the Envisat's $x-$, $y-$ and $z-$ CG position.

The last check needed to be made refers to the structural condition of the net. In fact, as observed in Figure 7.4, the net does not break during the capturing process as the maximum tension force never reaches the allowable 2100 N value. Thus, this means that an impact of $V_{net} = 20$ m/s is considered to be a safe deployment velocity for the net.

Thus it could be concluded using both these results and subsection 7.2.1, that on a pure net capturing basis, the mission would be successful with no risks of generating secondary space debris to be predicted. However, this brief analysis does not present the net-spacecraft contact characteristics and hence it is recommended to investigate further by starting with the net contact forces and moments.

7.3. Resulting Contact Forces and Moments from Net Impact

The resulting contact forces and moments can be found in Figure 7.5a and Figure 7.5b.
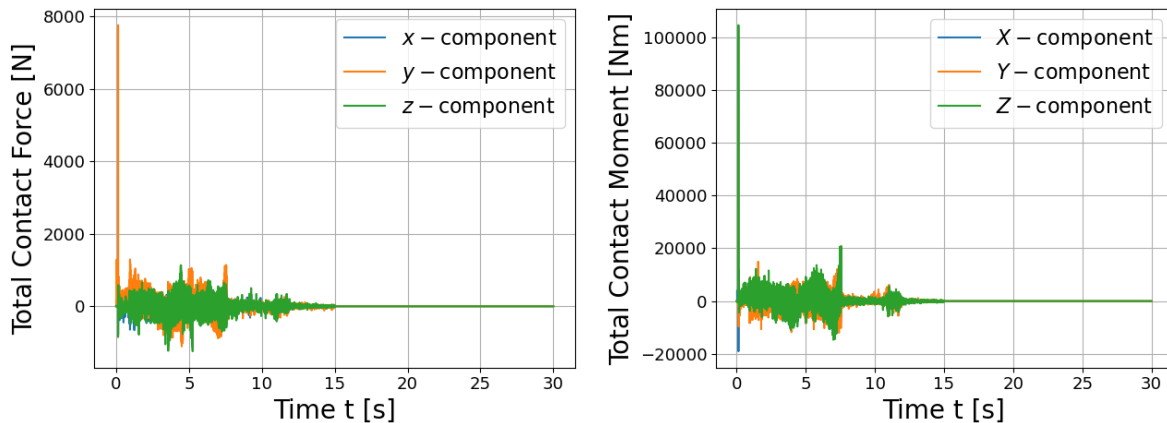
(a) Total contact force time series in the LVLH-frame $\mathcal{L}$.　　**(b)** Total contact moment time series in the body-fixed frame $\mathcal{B}$.

Figure 7.5: Resulting contact loads from a frontal net impacting with $V_{net} = 20$ m/s.

First, it must be noted that in order to artificially extend the simulation time and observe several dynamic phenomena, artificial dissipation was added to the contact loads doubling the simulation time. This is allowed as it can be seen in Figure 7.5a and Figure 7.5b that around the end of the simulation ($t \approx 15$ s), the contact loads start to decrease exponentially.

Secondly, one can observe from both Figure 7.5a and Figure 7.5b that the highest loads of 8 kN and 100 kNm, occur at the moment of impact (near $t \approx 0$ s). As expected, the highest force is in the along-track or $y-$direction with the contact moment being therefore mostly in the yaw or $Z-$direction.

Lastly, these then highly decrease and oscillate around -1.5 and 1.5 kN for forces and -20 and 20 kNm for moments. The latter is due to the main net wrapping which takes around 10 s, with then the contact dynamics starting to settle as the net has successfully wrapped around the target. A significant event is

however observed at $t \approx 7.5$ s (see Figure 7.5b) and is related to the contact between one of the bullets and the Envisat ASAR antenna. This impact of around 1 kN could result in impact breaking. For future work, it is suggested to simulate the latter event in detail using computational structural modelling to see the extent of the damage. In this Thesis, the focus is mainly placed on the effect of this loads on the system dynamics.

7.4. The Dynamical Risks

The aforementioned contact loadings are now taken as inputs for the Envisat dynamic analysis using the methodologies presented in Chapter 3 and Chapter 6. Before being able to define the initial conditions, it is essential to present the Envisat's inertial and geometric properties for the simulation. These can be found summarised in Table 7.3

Table 7.3: Envisat inertial properties.

Inertial property	Symbol	Value
Satellite mass	m_{SC}	7821 kg [25]
Solar array mass	m_{SA}	338 kg [25]
Solar array arm length	d	7.740 m [18]
Solar array stiffness	κ	5000 Nm/rad (M. Kroon, Priv. Comms)
Solar array damping ratio	ζ	2.5 % [89]
Body-fixed MMOI Matrix	$\mathbf{I}_d$	$\begin{pmatrix} 17023.3 & 397.1 & -2171.4 \\ 397.1 & 124825.7 & 344.2 \\ -2171.4 & 344.2 & 129077 \end{pmatrix}$ [25]
Solar array MMOI (principle axis)	$\mathbf{I}_h$	$\begin{pmatrix} 1800.0 & 0 & 0 \\ 0 & 10669.4 & 0 \\ 0 & 0 & 11290.9. \end{pmatrix}$ [18]

The initial conditions of the Envisat main body and solar array translational and rotational dynamics, before being hit by the net, are summarised in Table 7.4.

Table 7.4: Envisat initial conditions for single- and two-body dynamics.

Initial condition	Symbol	Value
Initial debris CG position	$(\boldsymbol{r}_{d/O})_0$	[-5.46, 22.36, -1.19] m
Initial debris velocity	$(\dot{\boldsymbol{r}}_{d/O})_0$	[0, 0, 0] m/s
Euler angular state	$[\theta_{X_0}, \theta_{Y_0}, \theta_{Z_0}]$	[0, 0, 0] deg
Body self-rotation	$(\dot{\boldsymbol{\theta}}_d)_0$	[0, 0, −1.0] deg/s
Solar array state	$[\theta_{s_0}, \dot{\theta}_{s_0}]$	[0 deg, 0 deg/s]

7.4.1. Single rigid-body risks

When assuming that the Envisat spacecraft is a single-rigid body system, the aforementioned contact forces and moments, will lead to a dynamic response of the satellite related to its translational and rotational dynamics.

Translational dynamics

The first dynamics of interest are related to the CG perturbation in the $\mathcal{L}$-frame. The perturbation of the CG position and velocity w.r.t. its initial position before impact can be found in Figure 7.6a and Figure 7.6b, respectively.
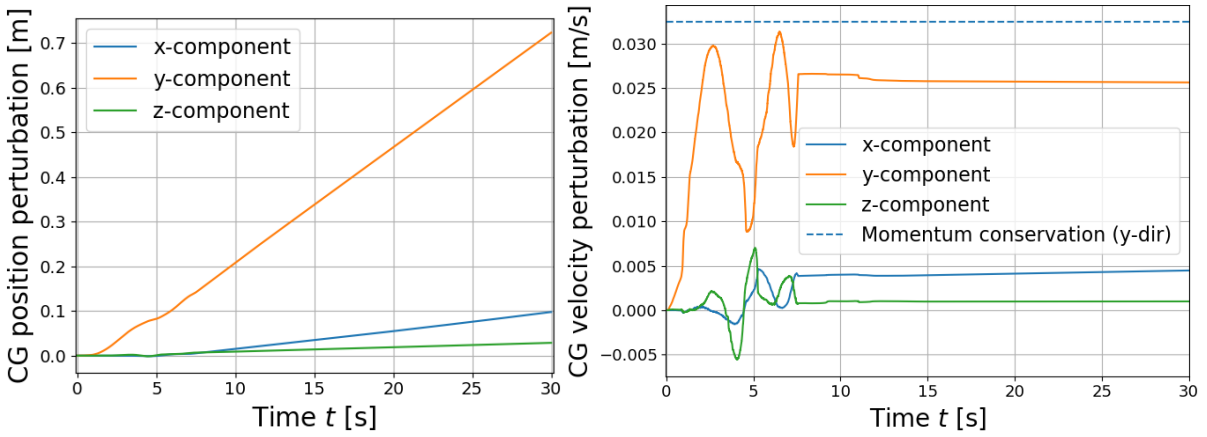
(a) Debris cg variation in the LVLH $\mathcal{L}$-frame due to net impact.   **(b)** Debris velocity cg variation in the LVLH $\mathcal{L}$-frame due to net impact.

Figure 7.6: Resulting translational dynamics of single-rigid body caused by a frontal net impacting with $V_{net} = 20$ m/s.

One can observe that the contact forces act as Dirac pulse inputs resulting in the satellite having an impulse response for its velocity. With the latter, the highest perturbation is in the along-track direction, which is expected as it is in the main net impact velocity direction. The high oscillation in Figure 7.6b are due to the bullet wrapping which occurs cyclically in multiple direction until the entire satellite is covered.

Additionally, the response reaches a settling value at a total velocity magnitude of 0.026 m/s, which is lower than the maximum allowable value that could have resulted from an ideal plastic impact. Given that velocity, one can see that the position variation in the along-track direction is also dominant with a slope equal to the settling value (verifying the latter result). However, as this variation in cg reaches 0.7 m in only 30 s, this shows the importance of active control in order to remove the danger that the spacecraft would leave the net (known as net slipping). To mitigate the latter risk, it is recommended to use a closing mechanism as done in [15, 76] with the addition of tether-length control system.

Lastly, due to the positional and velocity oscillations, a final risk related to the vibrational coupling between the tether and the solar array of the Envisat could arise [5, 6]. In the case of such coupling, a resonance phenomenon would occur in which the solar array could highly vibrate and break, leading to ejecta and potentially smaller debris escaping the net. Due to the high likelihood of the latter, it is suggested to mitigate this risk by appropriately designing the tether which will be the subject of Appendix C.

Given the translational dynamic analysis, the variation in the variables were found to be low. Whereas an exception can be made on the severity of the resonance-related risk, three control methodologies are still suggested to limit any type of perturbations. From the identified risks, it is clear that no significant events resulting in catastrophic failure can be observed. A similar analysis is required to be made for the rotational dynamics in order to evaluate if catastrophic failure, specifically related to net-tether breaking could occur.

Rotational dynamics

The second analysis is related to the contact moment input and its effects on the Envisat's rotational dynamics. The relevant results, related to the rotation rate and angular deviation can be found in Figure 7.7a and Figure 7.7b, respectively.
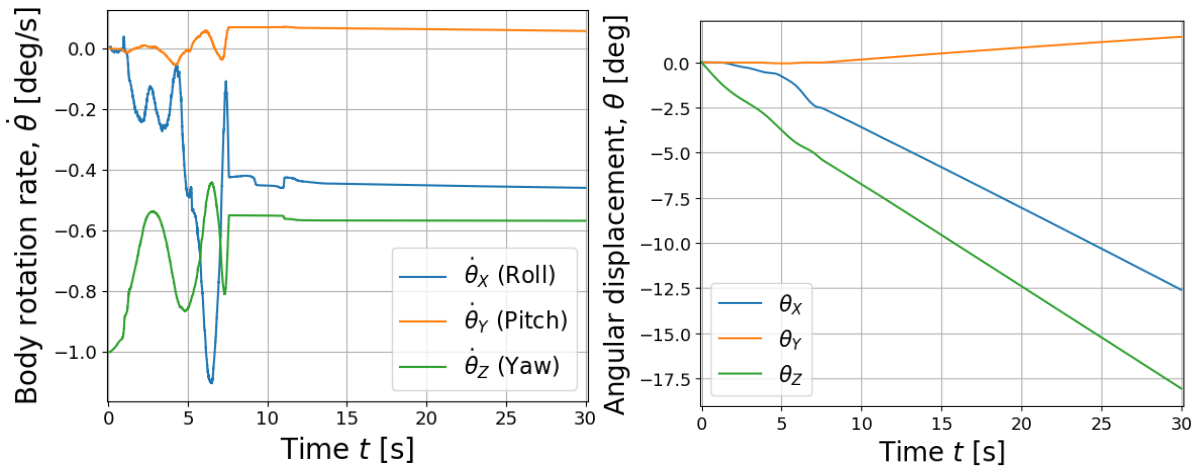
(a) Debris body-frame self rotation velocity $\dot{\boldsymbol{\theta}}_d$ due to net impact.

(b) Debris Euler angular motion due to net impact.

Figure 7.7: Resulting rotational dynamics of single-rigid body caused by a frontal net impacting with $V_{net} = 20$ m/s.

It can be immediately observed that as with translational dynamics, the contact moment results in impulse responses for the rotation of the system. Furthermore, the net impact itself acts as a yaw rotation rate damper as the magnitude of $\dot{\theta}_Z$ decreases from its initial value to 0.55 deg/s (see Figure 7.7a). Whereas, the impact has positive de-tumbling effect on the yaw rotation rate, it however induces a significantly large roll (from 0 deg/s to a settling value of -0.45 deg/s). Both results are to be expected as with the low effect on pitch motion, these are all due to the Envisat geometry itself. The yaw-related moment arms are the largest (due to the long solar array end being around 16 m away from the spacecraft cg), followed by roll moment arms as can be visualised in Figure 2.3.

These constant settling values can however lead to several issues, one of which can be observed in Figure 7.7b. After only 30 s, the spacecraft would have rotated in the yaw axis of -17.5 deg, which can be translated to a distance deviation in the y-direction of around 6 m. With such a significant deviation, the tether could entangle itself with the net body, resulting in a limited control authority during the towing phase or frictional tear and consequently net opening. Another potential risk has been described in Shan et al.[75], in which as the spacecraft continues to rotate. This induces a pulley-effect which can lead to a chaser-target collision. As any type of collision between the chaser and the 10 mm-thin solar array could result in solar panel breaking, secondary space debris would then be generated. As with the translational dynamics, it is suggested to have a tether-length control system which would immediately de-tumble the induced rotational rates, as done in [75].

7.4.2. Two-Body system risks

In the previous section, the Envisat was assumed to be a single-rigid body system. With already the single rigid-body simplification, several risks were identified. This leads to the necessity of verifying what happens to the solar array if it is allowed to move independently from the main body.

Identifying the risks of solar array dynamics

The relevant results are limited to the coupled rotational dynamics of the solar array in Figure 7.8 and of the main body in in Figure 7.9a and Figure 7.9a.
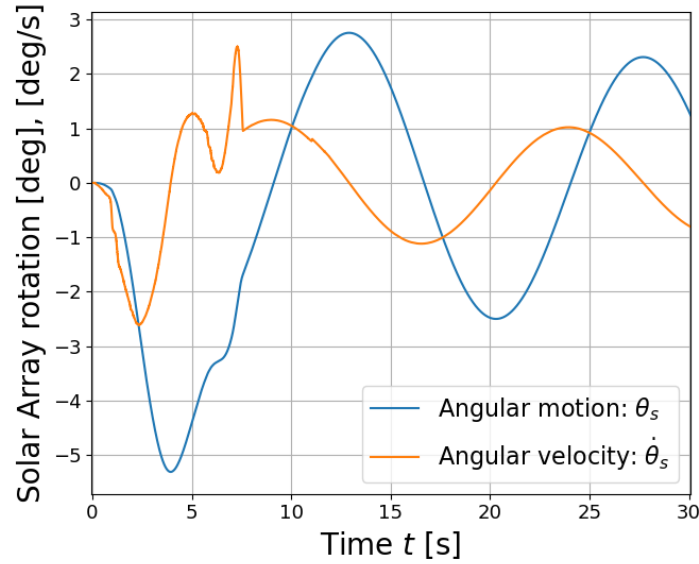
Figure 7.8: Angular motion of the solar array subjected to a frontal net impact of $V_{net} = 20$ m/s.
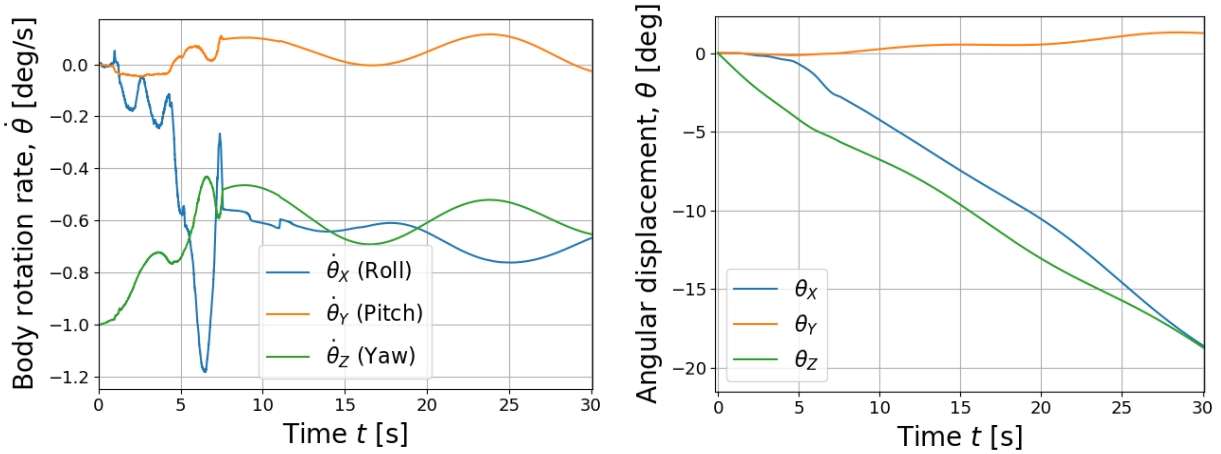
(a) Main satellite body-frame self rotation velocity $\dot{\boldsymbol{\theta}}_d$ due to net impact.

(b) Main body Euler angular motion due to net impact.

Figure 7.9: Resulting rotational dynamics of the two-rigid body caused by a frontal net impacting with $V_{net} = 20$ m/s.

First, one can observe from Figure 7.8, that with large contact torques, the solar array would initially oscillate between -5.2 and 3 deg, and exponentially damp out. Even though this result might seem insignificant, the deviations could lead to breaking near the hinge-panel interface. Additionally, these deviations can also be translated to 1.37 m in the z-direction, which could cause the net to break by cutting effect or exceeded elongation.

Lastly, as can be seen in Figure 7.9, the presence of an oscillating large solar array exacerbates the risks mentioned in the previous section. As one can see from Equation 6.14 and Equation 6.15, due to the large mass, moment arm and overall size of the solar array, the highest coupling term related to m_{SA} and d^2, is significant. This coupling results in a higher mean settling value of $\dot{\theta}_Z \sim -0.6$ deg/s and $\dot{\theta}_X \sim -0.7$ deg/s. These higher values show a significant increase in the Euler angles (Figure 7.9b), as Envisat would now rotate around the yaw and roll axis by -19 deg. These findings increase the severity of the aforementioned risks and with an increased likelihood of catastrophic failure of the solar array.

Risks at the primary hinge location

The severity of the dynamic results is accentuated by the actual loads experienced by the main solar array hinge as observed in Figure 7.10 with $M_{S_{h_i}}$ referring to the components of $\boldsymbol{M}_S$ in the hinge's local frame.
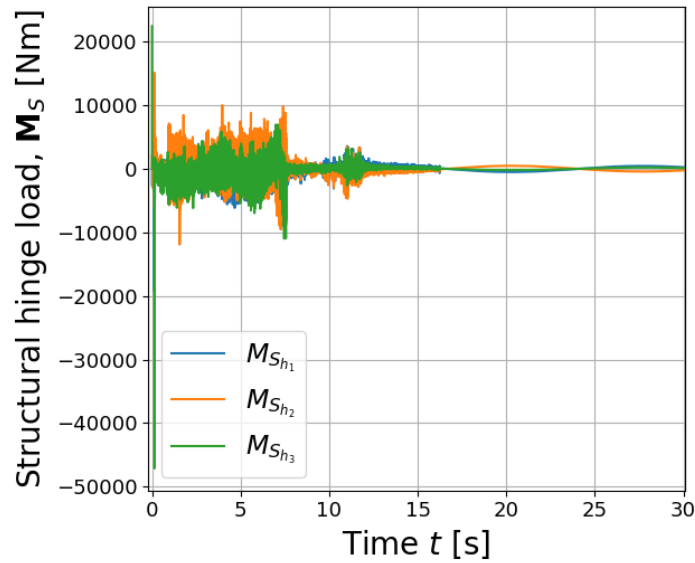
Figure 7.10: Structural hinge moment loading, $\boldsymbol{M}_{s_H}$, in hinge frame due to the frontal net impact of $V_{net} = 20$ m/s.

Before presenting the entirety of the graph, it is essential to mention that the maximum loads of 50 kNm and 15 kNm (in $\hat{\boldsymbol{h}}_3$- and $\hat{\boldsymbol{h}}_2$-directions) have both a duration of 10^{-5} s and are not to be considered in the structural analysis of the hinge. Whereas rejecting this large load would be seen as sufficient and the hinge could be assumed to be safe, it still experiences a consistently re-occurring ± 4 kNm ($M_{S_{h_1}}$) and ± 5 kNm ($M_{S_{h_3}}$) loads from $t \approx 0.25$ s. These two loadings largely exceed the maximum hinge loads in all directions (see section 6.4) and can be assumed to result in failure. Additionally, with such loadings, the hinge-panel interface can be found to experience a maximum out-of-plane load of 4.1 kNm. This means that at that location, failure would also have been expected to happen, as typical values of the interface strength vary from 200-1000 Nm (see section 6.4). Due to the closer location of the hinge-panel interface (see Figure 6.5), it can be assumed through the propagation of the stress waves, that this location would fail first, generating a 5×14.3 m secondary space debris.

It is still important to mention, that the latter results are mostly conservative due to the assumed higher moment arm (see subsection 2.8.2) and the post-processing implementation of the contact loads effect on the spacecraft. Additionally, the methodology used to compute the contact loads has been observed to show some irregularities in its results (see section 5.2). However, even with the latter, the assumptions made are still justified by the fact that Envisat's mass and size are much larger than the impacting net and hence the effective real loads would not be lowered sufficiently to be near the maximum allowable loads of the hinge-panel interface. Last but not least, the magnitude of the loads themselves will also be validated in Chapter 9, which further confirms the urgency of the risk.

7.4.3. Risks of antenna breaking

The final structure of interest which needs to be checked is the Ka-band antenna. Given the methodology in section 6.5, the risk of dynamic breaking at the moment of impact can now be investigated. All initial conditions for the deflection, Δy and deflection velocity, $\Delta \dot{y}$ are assumed to be null before impact.

Vibrations analysis

First, before presenting the deflection in both local $X-$ and $Y-$ directions for both CFRP and the Titanium alloy, it should be noted that the difference in behaviour between these two materials can be assumed to be negligible due to the similarity of the materials' $\sqrt{E/\rho}$ ratios (see Equation 6.23). Due to the latter, the material effect on the tip deflection is negligible.

Secondly, the contact force and tip deflection for the CFRP antenna can be observed in Figure 7.11.
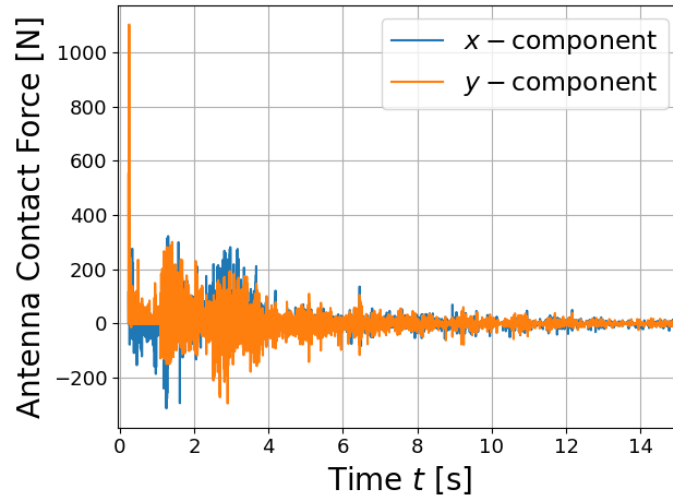
(a) Contact force (in $\mathcal{L}-$frame) of the net with the Ka-band antenna as a function of time.
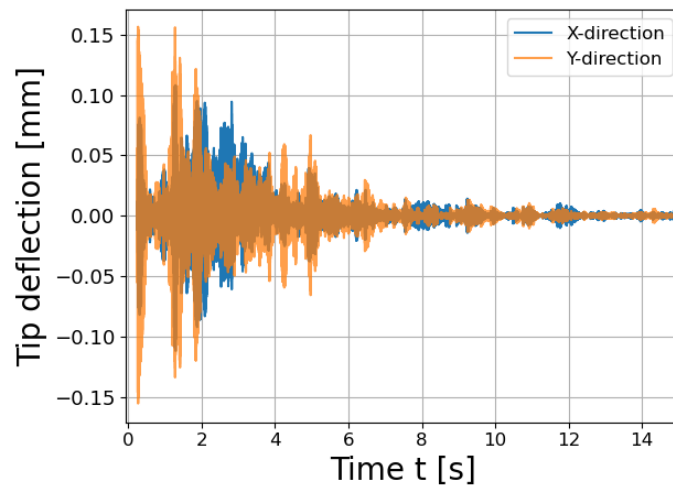
(b) Tip deflection of the Ka-band antenna in local $X-$ and $Y-$ directions for the CFRP material.

Figure 7.11: Resulting contact and vibrational dynamics of the Ka-band antenna by a frontal net impact with $V_{net} = 20$ m/s.

From Figure 7.11a, maximum loads of 0.405 kN and 1.105 kN ($x-$ and $y-$components respectively) can be observed. On average, and as expected due to the frontal net impact, the contact force in $y-$direction is higher than the one in x. This then results in an overall larger Y-tip deflection (see Figure 7.11b). The maximum deflections in the X- and Y-directions are approximately the same of ± 0.15 mm. This maximum occurs both around $t \approx 0.234$ s and $t \approx 1.585$ s, when the two highest contact forces affect the antenna, at impact and during the first bullet re-direction cycle (see Figure 7.3). Regardless, of these events, the antenna **does not break** due to vibration as the allowable material deflections for CFRP and Titanium are 7.306 and 76.24 mm (obtained using Equation 6.24).

Structural analysis

Lastly, the stresses experienced at the two weak locations were computed from the structural forces and moments (see subsection 6.6.3) and can be found in Figure 7.12.
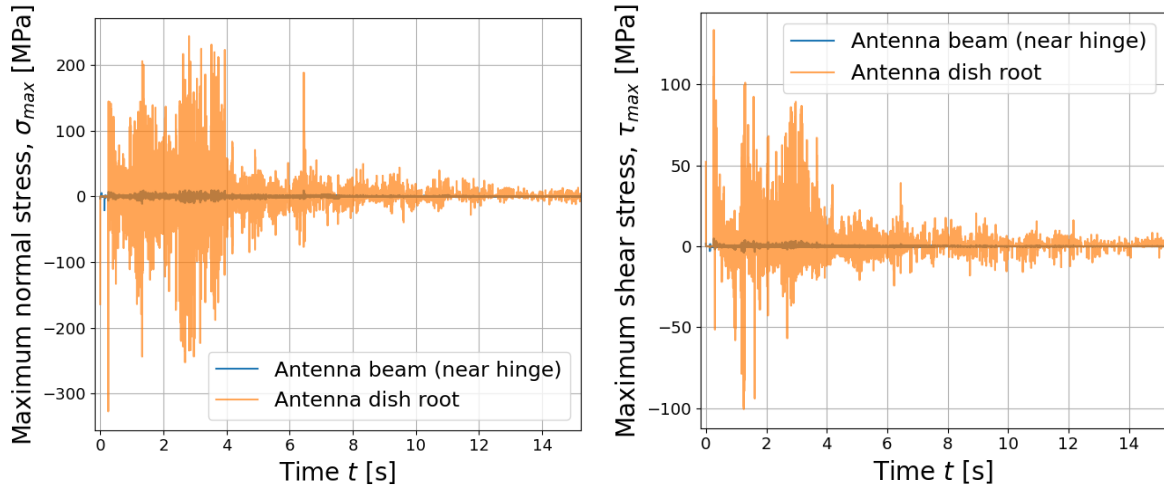
(a) Maximum normal stress (bending and axial combined) of the antenna at two locations as a function of time.

(b) Maximum shear stress (torque and linear combined) of the antenna at two locations as a function of time.

Figure 7.12: Resulting normal and shear stresses of the Ka-band antenna from the contact dynamics of a net impact of $V_{net} = 20$ m/s.

From both figures, one can see that at the dish root, both types of stresses are higher by one to two orders of magnitude due to the significantly lower cross-section (see Table 2.2). This means that the interface between the dish of the antenna and its beam is a more critical region for breaking to occur.

First, recalling the maximum allowable material properties for ultimate normal stress (3.5 GPa and 950 MPa) and shear stress (50-140 MPa and 550 MPa) summarised in Table 6.1 and for both materials, it can be seen that the Ka-band antenna **will not fail** due to bending and axial tensile stress in either of the two locations. Additionally, the antenna will not fail in compression as its negative normal stresses observed in Figure 7.12a do not reach even a third of its ultimate material values.

Secondly, in the case that the antenna is made of the Titanium alloy, shear is also not an issue and **will not** result in structural failure. However, in the case of CFRP sub-structures, a high uncertainty is present due to the maximum of 134 MPa, and the re-occurring 30-80 MPa values (see Figure 7.12b). As the maximum and subsequent shear stresses are near the highest extreme of the allowable interval ([50-140] MPa), it is thus possible that the Ka-band antenna **would fail** at the interface between the dish and the main beam (weak location 4, see Figure 6.5). In the case of breaking, a secondary space debris would be created being the Ka-band antenna dish and further ejecta from the fracture process.

Thirdly, the likelihood of (compression-related) breaking is accentuated by the high probability of buckling. Indeed, by computing the critical stress of the Ka-band antenna beam (see Equation 6.34), $(\sigma_{cr})_{TiGa} = 207.248$ MPa (Titanium alloy) and $(\sigma_{cr})_{CFRP} = 455.290$ MPa (CFRP) are obtained. The metallic alloy is therefore more prone to buckling and hence to high instability, compared to CFRP. However, as the ultimate compression load is still significantly larger, failure seems to be improbable. The second limit related to CFRP, even though not reached during the simulation, is very close to the "maximum" of -350 MPa (see Figure 7.12a). This added to the high probability of shear failure seems to increase the risk of breaking.

In conclusion, due to the uncertainty related to the Ka-band antenna material properties, a risk of shear failure at weak location 4 combined with buckling **does exist**. However, due to the simplicity of the method and models used, it is suggested to perform a robust numerical analysis of the stresses to definitely conclude if the latter is likely happen.

7.4.4. Brief note on the ASAR structural integrity

The 10 m-long ASAR antenna was assumed to not be a critical object of secondary space debris due to its large cross-section and eight-joint connection with the main body. As a result of the simulation, a maximum compression and tensile load of 2000 N and 640 N were obtained at the connection sight with shear loads reaching 500-750 N (see Figure 7.13).

(a) Structural load in mi-ASAR location as a function of time.

(b) Structural moment at mid-ASAR position as a function of time.
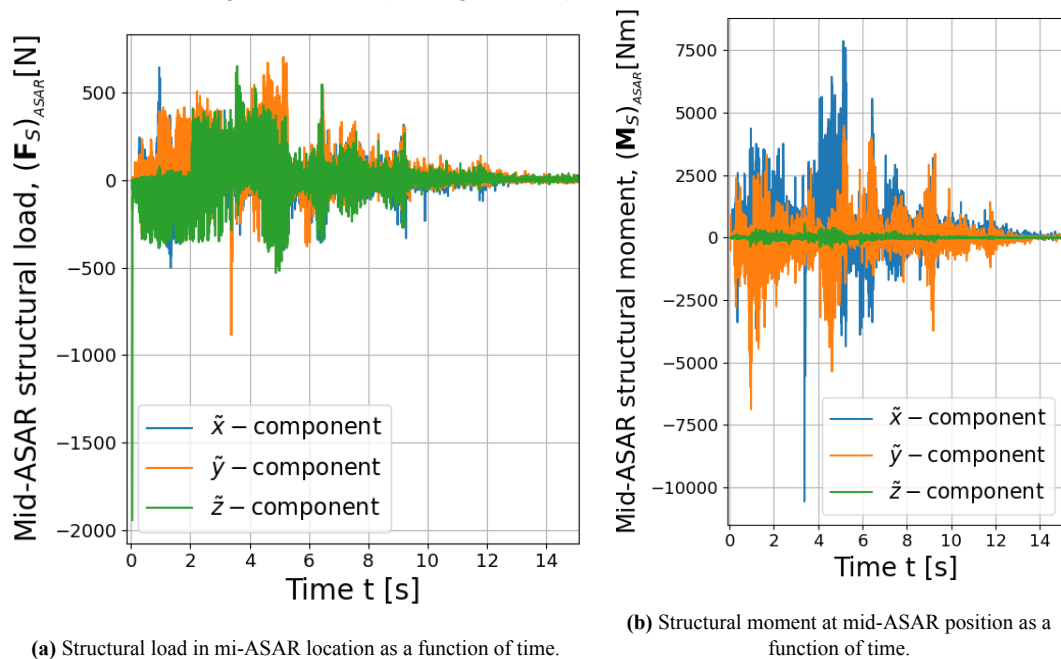
Figure 7.13: Resulting structural forces and moments at mid-ASAR position from the contact dynamics of a net impact of $V_{net} = 20$ m/s.

These divided by the cross-sectional area (see Table 2.3), result in a compressive and tensile stresses of 8.55 kPa and 2.78 kPa, which are five to six orders of magnitude lower than the ASAR's CFRP frame ultimate capabilities (see Table 6.1). Furthermore, when observing the total normal stress in Figure 7.14, which adds the contribution of bending, the latter is further confirmed as a maximum values are only of -1.0 to -1.75 MPa (three orders of magnitude below the ultimate strength). Shear stresses, in all directions, also seen from Figure 7.14, are insignificant compared to the ultimate material properties. Thus for failure to occur, a damage size-to-width ratio, $d/b = 0.98$ would be required (see Equation 6.6.5). This however has not been seen by Pleiades satellite observations [85] and is hence highly unlikely.
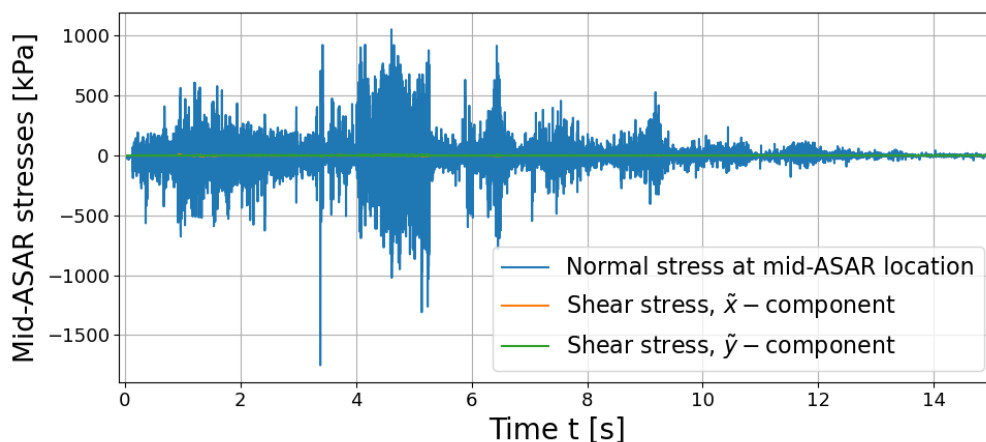
Figure 7.14: Normal and shear stresses in mid-ASAR location due to the frontal net impact of $V_{net} = 20$ m/s.

Finally, with eight joints (approximately 25-50 mm in diameter Figure 2.8), the loads present in Figure 7.13 would result in a maximum normal stress of 100 kPa, which itself is still lower than the material ultimate stresses of commonly used joint-related materials. Therefore, ASAR structural failure, due to net loadings, is thus confirmed to be a highly unlikely event and does not require further investigation.

7.5. Investigation Summary with mission design recommendations

In this section a summary of the dynamic investigation, from net to satellite dynamics, will be presented, ending with mission design recommendation.

7.5.1. Net and single rigid-body dynamics

Before presenting the spacecraft results, the net dynamics and internal stress analysis showed that no particular event could be used as a predictor of spacecraft structural failure (apart from the ASAR-bullet impact event). This means that the net dynamics are not a sufficient indicator of the mission overall success. The first risk-related finding was obtained by assuming that the Envisat is a single-rigid body. The risks related to its dynamics were shown to be lower for translational motion than for rotational motion due to the satellite's size and geometry. Nevertheless, two risks were identified related to the dynamics of the connecting tether and the potential of a chaser-target collision (through a pulley effect), resulting in a high amount of secondary space debris. Given this, a dynamic towing phase simulation will be performed in the next chapter, resulting in an optimal tether design.

7.5.2. Two-rigid body dynamics

The second finding was obtained by considering the Envisat as a two-rigid body system. The solar array was found to increase the aforementioned (single-rigid body) risks and create new problems leading to net cutting or/and solar array partial breaking. The primary hinge and panel-secondary hinge locations were found to be critical with the second one being were structural breaking would most likely occur first, creating a secondary space debris with size 5×14.3 m and a mass of 338 kg.

7.5.3. Antenna structural dynamics

Thirdly, the antenna vibrational dynamics and structural analysis were performed. It was concluded that whereas dynamic failure would not be present, the antenna would most likely break at its dish root interface due to a combination of shear and buckling failure. This would create a secondary debris as a 0.9 m radius Ka-band antenna dish with the additional 230 mm-long (48.6 mm wide) supporting beam.

7.5.4. Mission design recommendations

Finally, given these results, several recommendations can be made. Three of the recommendations strive to lower the contact forces experienced by the satellite, with the third eliminating them completely (or at least to a significant extent) the final one focuses on designing an optimal control system ensuring optimal control authority and status monitoring.

The first recommendation is to lower impact velocity of 20 m/s used for these simulations, to 2.5 m/s. This is expected to lower contact loads by a factor of 10 and is more in-line with existing literature. Additionally, due to the lower velocity, the stability of the penalty-based method (see section 5.2) would highly improve and the force values' uncertainty would be diminished. The second recommendation would then be to design the net with a high dampening effect. This can be implemented by a thorough material selection and an inflatable thread design, similar to [56]. As with the first point, it is expected to lower the contact loads and hence the likelihood of failure. Lastly, to limit the severity of a bullet-ASAR impact, it is recommended to increase the net size. This is expected to reduce the bullet velocity and the impact likelihood itself. as the net wrapping is more evenly distributed.

Given these three methods, it also be suggested to deploy the net such that to avoid impact and

wrapping of the solar array. With this method, the solar array would only vibrate due to its base, lowering not only solar array vibration (seen as increasing dynamical risks in subsection 7.4.2), but also the structural loads on the PIP and hinge weak location sights. This recommendation would also be simple to implement and could result in a lower net mass, thus lowering also the chaser mass itself. Furthermore, in the case of that a control system is wished to be used, the functions and requirements on the latter could be alleviated by focusing only on tether-length control (see subsection 7.4.1) and on the dampening of the solar array oscillations during the towing phase (see Appendix C).

The final recommendation is to design an optimal control system for both the chaser-tether system and the bullets. The first one will ensure that the dynamic perturbations caused by the impact will be eliminated and should limit any oscillations during the towing phase. The second one relates to already existing in literature robotic bullet systems with active control [98]. These in turn would ensure optimal impact, wrapping and net closing under non-nominal impact conditions. With the additional benefit which could be to design the bullet's control system to lower the probability of bullet-flexible appendage hard impact and solar array hinge loadings which were both observed during the simulation. By decelerating during the wrapping process, the loads on the flexible appendages and connection sights would be significantly lowered, decreasing the probability of generating secondary space debris.

8
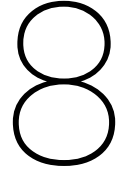
Sensitivity Analysis of Net-Spacecraft Dynamics

Given thorough descriptions of all dynamical models, and the results of the preliminary investigation, a sensitivity analysis can be made, as part of a better understanding which physical net dynamic properties accentuate secondary space debris generation. With this, it is essential to select the crucial input parameters and perform a sensitivity analysis.

8.1. Strategy Overview for Sensitivity Analysis

Given the complexity and the interactions of the different models used in this Thesis work (see Chapter 3), two types of sensitivity analysis will be made. The first one will be purely analytical by focusing on the phenomenological nature of the penalty-based method and understanding to which extent the inputs have an influence on the normal component of the contact force (see section 8.2). The reason for this analytical approach is that numerical simulations would only provide the time distribution of the contact forces, but their magnitude which is highly related to the breaking process is simply computed analytically.

The second type of sensitivity analysis will focus on the net dynamics simulation, varying two of all the relevant input parameters presented in Chapter 4 and evaluate their influence on the tension and contact forces and moments. These should be chosen as part of numerical simulations, as their influence is the result of an accumulation of multiple dynamic interactions resulting in a non-analytical behaviour.

For the first type of analysis, an analytical evaluation of the effect of net dynamics on the contact force will be performed. In contrast, for the numerical simulations, the parameters will be chosen via a selection procedure with their increasing/decreasing impact evaluated on a coarser mesh.

8.2. Sensitivity analysis of the analytical contact force relation

A simple sensitivity analysis is presented here which allows to rapidly and efficiently predict the variation of net deployment variables without requiring a time-consuming multi-variate Monte-Carlo simulation.

The deployment variables V_e and θ_e, and initial debris body-fixed rotation rate $\omega_{d,0}$, can be seen to have an effect, during a frontal impact, on the penetration δ and rate $\dot{\delta}$, which can be approximated as follows:

$$\dot{\delta} \approx V_e \cdot \cos(\theta_e) \pm \omega_d \cdot r_{i/C} \cdot \sin(\xi) \tag{8.1}$$

$$\Delta\delta \approx \dot{\delta} \cdot \Delta t \tag{8.2}$$

where $r_{i/C}$ is the point of contact relative position $x-$component to the debris center and ξ refers to the complementary of the normal incidence angle. As these parameters affect an input parameter of the normal force, it is understood that they will also affect the contact dynamics.

Therefore, by defining a nominal simulation, described with subscript 0, resulting in $F_n(\dot{\delta}_0)$ and a maximum possible contact force $(F_n)_{max}|_{\dot{\delta}_0}$ taken from literature [15], an approximation of the effect with a different conditions (1) can be found with:

$$F_n(\dot{\delta}_1) \sim F_n(\dot{\delta}_0) \cdot \left(\frac{\dot{\delta}_1}{\dot{\delta}_0}\right)^n \cdot \frac{1 + \frac{3}{2}\alpha\dot{\delta}_1}{1 + \frac{3}{2}\alpha\dot{\delta}_0} \leq (F_n)_{max}|_{\dot{\delta}_0} \cdot \left(\frac{\dot{\delta}_1}{\dot{\delta}_0}\right)^n \cdot \frac{1 + \frac{3}{2}\alpha\dot{\delta}_1}{1 + \frac{3}{2}\alpha\dot{\delta}_0}. \qquad (8.3)$$

The effect of other variables is hence limited by this maximum value in order to increase the realism of the simplified analysis.

Given Equation 8.2 and Equation 8.3, the effect of changing V_e and θ_e can be quickly determined without the need of multiple time-consuming numerical simulations. It must be noted that the deployment and impact time can also be easily altered by a simple velocity ratio in the same manner as Equation 8.3.

Thus, a simplified and analytical Monte-Carlo analysis will be performed by distributing the inputs presented in Equation 8.2 uniformly with input-specific ranges. The deployment velocity and angle will be limited to $[0.5, 20]$ m/s and $[15, 65]$ deg, respectively [69]. The net node position $r_{i/C}$ will also be distributed uniformly from -7.0 m (most extreme position of the Envisat's hub CG) to 20 m (second extreme location of the solar array from CG). Lastly, given the potential of space debris rotation (see subsection 2.8.2), this will be distributed uniformly from $[-1.5, 1.5]$ deg/s with the impact angle assumed to be normal ($\xi = 90$ deg).

8.3. Selection of Net Dynamics Input Parameters

As an initial observation, one can identify more than six input parameters related to the internal physical and dynamic properties of the net to fully parametrise the **MSD** model, seven initial conditions required to initialise the numerical simulations and two parameters that define the bullet mass and location.

8.3.1. Net and bullets physical properties inputs

To properly define the net dynamics, one must define its material (1), geometry (2), internal tension-related properties (3) and bullet mass and location (4). Thus there are four main categories observed which can aid in the selection process. As a initial step, it is decided to fix the net material (hence fixing the Young's Modulus E and net density ρ_{net}) to Kevlar, as this one will be decided mainly in the beginning of mission design for similar reasons presented in subsection 2.4.1. Furthermore, both the net mesh size (l_{0_q}) and bullet tether length (l_{0_b}) are fixed based on the high sensitivity and limitations of the contact detection algorithm, and on literature [15, 68].

The net physical parametrisation starts with the geometry being full defined by the net side length L_{net} and thread diameter d_q. These two parameters will influence the contact detection algorithm, but also the distribution of stresses in the net and on the spacecraft. Having defined the net geometry, the stiffness and damping constants (k_q and c_q) follow. By assuming only tension, the stiffness is already fully defined by the latter variables whereas the damping constant only requires the damping ratio ζ. This usually is taken in literature as 0.1 [15, 68] to ensure that the net's EoMs are stable in time. Lastly, the bullets are purely defined by their mass m_b which is usually a free-variable and can be used in the selection procedure.

8.3.2. Net initial conditions

Now that a geometry is defined, the kinematic initial conditions are essential to initialise the net (deployment) dynamics. These are the following:

1. bullet deployment velocity V_e,
2. bullet deployment angle θ_e,
3. net compact ratio η_{net},

    4. net-body velocity ratio η_V,

    5. Center-of-Mass deviation, $\Delta\boldsymbol{r}_0$, in xz-plane (LVLH-frame) w.r.t the target geometrical center.

From basic intuition, the effect of η_V is assumed to negligible due to the very restricted typical range of values used in literature [15, 16, 68, 72]. Furthermore, the compact ratio η_{net} is also assumed to not have a great effect on any of the important aspects to be considered in this study. Its effect would mostly affect the net deployment dynamics quality and not its potential to break the satellite's sub-structures.

8.3.3. Final choice of parameters

To select the most relevant parameters, a similar method to the graphical trade-off matrix will be implemented. The positive, negative or neutral qualitative (or quantitative) influence on the various important aspects of the capturing process will be evaluated. These aspects with their associated weights of importance (in brackets) and ID are listed below:

- wrapping capability, WP (3/10),
- effect on the distribution of tension forces, DTF (1.5/10),
- severity of the impact, SI (3/10),
- net momentum distribution, NMD (2.5/10).

Both WP and SI are given the highest weights with NMD second, as those are expected to have the highest influence on the risks of structural breaking. Thus, the lower the wrapping efficiency and the higher the impact severity, the higher the risk of structural breaking can be expected.

    The increasing effects of input parameters on the aforementioned aspects can be found summarised in Table 8.1, in which green means that there is an expected high variation (score of 100%), blue is for an expected medium-level variation (80%), yellow reveals little effect (score of 50%), gray is when it is uncertain if variation could occur (score of 40%) and red when no effects can be predicted (score of 0%). The input parameter(s) with the highest potential will be chosen.

    Given these summarising explanations, scores can be attributed and the selection of parameters can be finalised. The ranking of the parameters with associated scores can be found below.

1. Bullet mass, m_b (**8.8/10**),
2. net side length, L_{net} (**8.5/10**),
3. initial CM deviation, $\Delta\boldsymbol{r}_0$ (**7.5/10**),
4. deployment velocity, V_e (**7.3/10**),
5. thread diameter, d_q (**5.3/10**),
6. deployment angle, θ_e (**4.3/10**).

First, interestingly enough, one can identify that the highest scores are given to net physical characteristics, whereas the third and fourth places are related to the net's kinematic initial conditions.

    Secondly, from the ranking, m_b and L_{net} are winners of the selection procedure, with scores indicating a possible significant difference w.r.t the other parameters. However, the difference within the two pairs: $\Delta\boldsymbol{r}_0$ and V_e, and m_b and L_{net} are minimal and cannot be used to definitely reject one or the other. On the other hand, d_q and θ_e are clearly not relevant parameters to be used for the sensitivity analysis due to their considerably lower scores.

    Finally, it is decided to not select V_e, given the fact that the effect of V_e will be analysed in the analytical sensitivity analysis. Additionally, as it would be more optimal to vary the type of parametric input type for this sensitivity analysis, it is decided to select both the **bullet mass** and **CM deviation**. Last but not least, it is also decided to perform the simulations assuming a frontal impact without simulating deployment. This is due to the fact that the main deployment characteristics are dominated by V_e and θ_e, and as these were not selected there is no need for net deployment numerical simulations.

Table 8.1: Graphical Trade-off matrix between possible sensitivity analysis parameters with dynamical aspects. Column width is proportional to the aspect's/criterion's weight.

Input \ Aspect	WP (3/10)	DTF (1.5/10)	SI (3/10)	NMD (2.5/10)
L_{net}	The larger the net, the higher potential of total wrapping. [Green]	An increase results in different tension-force distribution. [Blue]	Contact forces are expected to have some limited variation. [Yellow]	A larger net (higher mass) results in momentum variations. [Green]
d_q	Whereas a minimum d_q is essential to not break, increasing d_q has little effect above the minimum value. [Yellow]	An increase causes a high decrease in tensile stress. [Green]	Contact forces are not assumed to be affected. [Red]	An increase in d_q results in a limited increased mass. [Blue]
m_b	A considerably large minimum bullet mass is essential for optimal wrapping. [Blue]	m_b affects the net corner tension, with little effect on the total stress distribution.[Yellow]	With increasing m_b, the net impact velocity is expected to increase with bullet impacts could result in breaking-off. [Green]	Increasing m_b should increase momentum. [Green]
V_e	An increase in V_e above a maximum value could result in tension breaking (no wrapping) below this value there is high uncertainty. [Gray]	Increasing V_e should result in increased tension at the corners (the rest of the net is uncertain). [Gray]	As V_e increases, the impact speed is increased and thus its severity. [Green]	Momentum is affected by impact velocity. [Green]
θ_e	Above the minimum 30-45 deg, an increase should not change wrapping. [Yellow]	Below maximum values of 60-75 deg [69], no effect is expected. [Red]	Below maximum values of 60-75 deg, no effect is expected. [Red]	Linear momentum is highly dependent on deployment angles. [Green]
Δr_0	With Δr_0 above certain thresholds, wrapping should be considerably affected. [Green]	No considerable effect expected. [Red]	Deviations result in different contact force distribution. [Green]	Deviations should result in variations of momentum exchange. [Yellow]

8.4. Risks as a function of net input parameters

As a first step, the analytical sensitivity analysis will be presented followed by the numerical type and a final summary of this secondary investigation of the net physical and dynamical properties.

8.4.1. Analytical evaluation and mitigation of risks related to contact-force model

First, the sensitivity of F_n w.r.t each input parameter will be estimated to select which one will be used to check under which conditions failure occurs.

Analytical risk evaluation

The sensitivity results can be found in Figure 8.1.

(a) Normal force sensitivity scatter plot as a function of V_e (and α-variation) with other input parameters being uniformly distributed.

(b) Normal force sensitivity scatter plot as a function of θ_e (and V_e-variation) with other input parameters being uniformly distributed.

(c) Normal force scatter plot as a function of ω_d (and θ_e variation) with other input parameters being uniformly distributed.

(d) Normal force scatter plot as a function of $r_{i/C}$ (and θ_e-variation) with other input parameters being uniformly distributed.

Figure 8.1: Sensitivity Results from a Monte-Carlo population on normal force variation w.r.t deployment initial conditions V_e (with α variation), θ_e and spacecraft initial conditions $\omega_{d,0}$ and location of impact $r_{i/C}$.

A first observation from Figure 8.1c and Figure 8.1d shows that due to the small allowable range of $\omega_{d,0}$ being only from -1.5 to 1.5 deg/s, its variation and that of $r_{i/C}$ show no particular pattern. This is due to their multiplicative combination $\omega_{d,0} \cdot r_{i/C}$ in Equation 8.2. Thus, in the case of small values of $\omega_{d,0}$, the target's rotation rate **is not** an interesting parameter to evaluate its effect on the potential of structural breaking-off. Whereas the impact location also does not result in any specific trend, it is still important as it will dictate the magnitude of the contact moment.

A second observation can be made for the deployment initial conditions V_e and θ_e in Figure 8.1a and Figure 8.1b. As expected, varying V_e from 0.5 to 20 m/s results in an overall F_n-variation of one to two orders of magnitude (depending on α). This is due to the approximate $\dot{\delta}^{n+1}$ term in Equation 8.3. Additionally, an increase in the contact parameter α shows, for high values of V_e, an approximate gradual increase in the force (Figure 8.1a) as can be predicted from Equation 8.3. In contrast with the latter are the results shown inFigure 8.1b. One can observe that the distribution of these values for θ_e is less pronounced for intermediary F_n-values. The maxima and minima are still affected by highly varying θ_e, but only by a factor of 1.6. This is confirmed in how θ_e-values are distributed in Figure 8.1c

and Figure 8.1d, compared to the regular trend for V_e. Thus, it can be concluded that **only** V_e can be considered to be a clear indicator if secondary-space debris could be generated.

Mission design risk mitigation strategy

Let us now recall that from a 20 m/s-frontal impact, breaking-off of the Envisat's solar array and Ka-band antenna occurred at two specific locations. Given the results obtained in this section, it is now possible to evaluate the variation of the maximum hinge-panel interface moment and structural stresses as a function of the impact velocity. This would allow to estimate the maximum impact velocity, and hence given a deployment angle, the maximum allowable deployment velocity. The results for the PIP interface and antenna dish root can be found in Figure 8.2.

(a) Antenna dish root absolute maximum shear stress as a function of impact velocity with maximum allowable shear stress interval (50-140 MPa).

(b) Maximum in-plane structural moment at the hinge-panel interface as a function of impact velocity with maximum allowable moment range (200-1000 Nm).
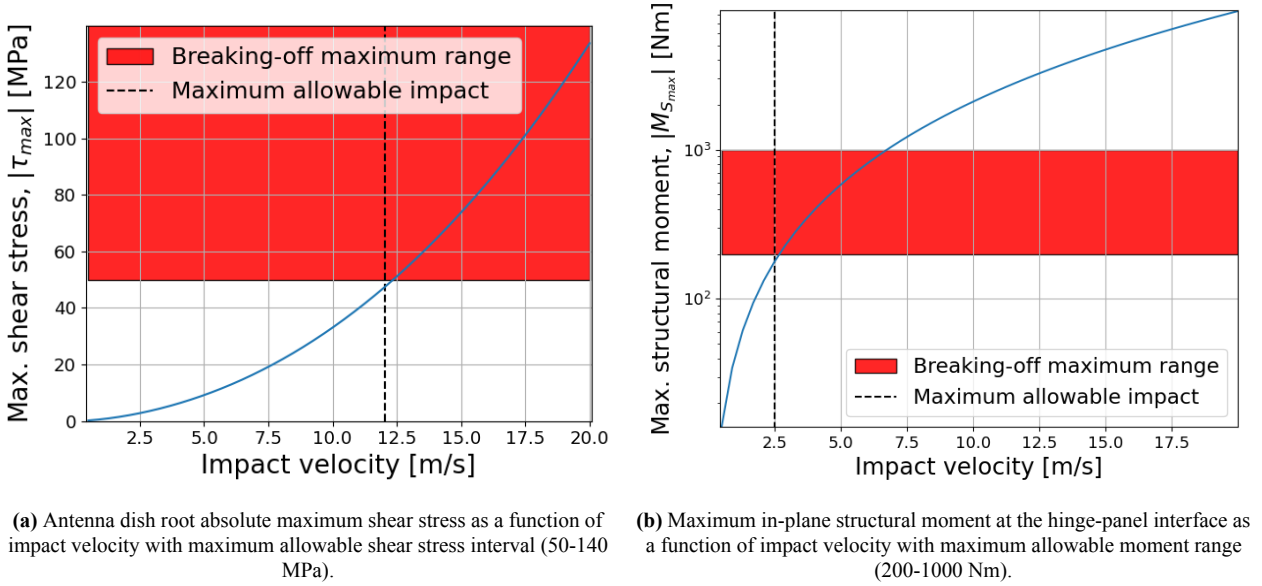
Figure 8.2: Sensitivity plots of structural breaking indicators as a function of impact velocity.

From Figure 8.2a and Figure 8.2b, two maximum allowable impact velocities are obtained being 12.0 m/s and 2.50 m/s respectively. Therefore, the aforementioned shows that the solar array structural integrity is more critical and highly constrains the impact velocity to a fourth of the simulation scenario results presented in Chapter 7. Thus by limiting the impact velocity to 2.0 m/s (1.25 ultimate safety factor), both the Ka-band antenna and solar array will not break. Using Equation 4.13, this can be ensured by an optimal combination of V_e and θ_e, resulting in the **mission design constraint**:

$$\frac{4\,m_b}{(m_{net} + 4\,m_b)} \cdot V_e \cdot \cos(\theta_e) \leq 2.0 \text{ m/s}. \tag{8.4}$$

8.4.2. Risk and mitigation evaluation via numerical method

Before presenting the numerical results it is decided to normalise the bullet mass w.r.t the total net mass in order to provide a general suggestion for the net design. Additionally, the interval of bullet-to-net mass ratio m_b/m_{net} is: $[0.125,\ 2]$, with $m_b/m_{net} = 0.75$ corresponding to the nominal simulation from Chapter 7. The deviation of the net is focused on the x-direction with an interval: $[-10,\ 5]$ m. Furthermore, to alleviate the computational time, the time step is set to $\Delta t = 0.75 \cdot 10^{-4}$ s and the total simulation time is limited to 10 s.

Risks of net dynamics and tensile breaking

Given the set of input parameters in Chapter 7, only the effect of m_b/m_{net} variation on net dynamics will be checked. The entire net dynamics sensitivity results can be found in Figure 8.3.
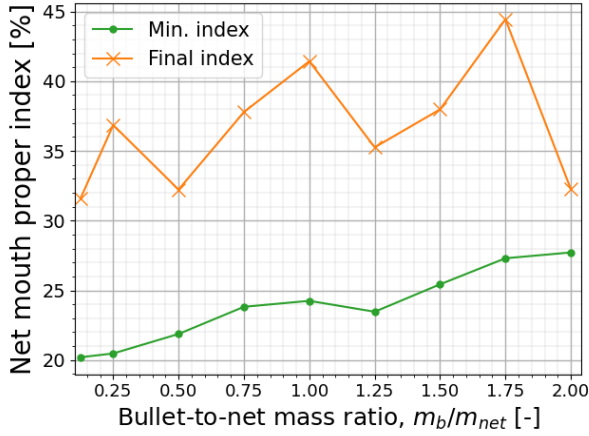
(a) Net mouth proper index ($L(t)/L_{net}$) with limits (minimum and end simulation values) as a function of bullet-to-net mass ratio.
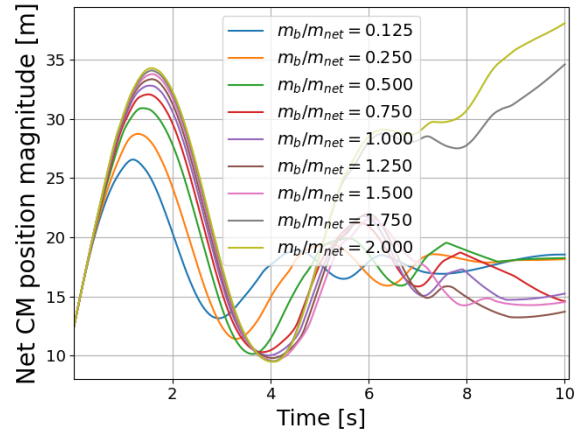
(b) CM position magnitude as a function of time for nine bullet-to-net mass ratios.
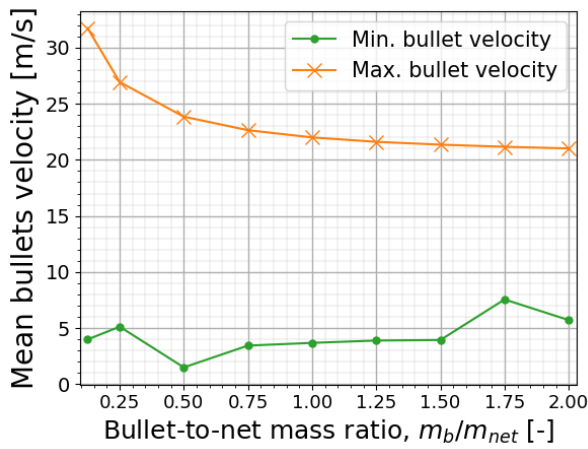
(c) Mean velocity magnitude over the four bullets as a function of bullet-to-net mass ratio.
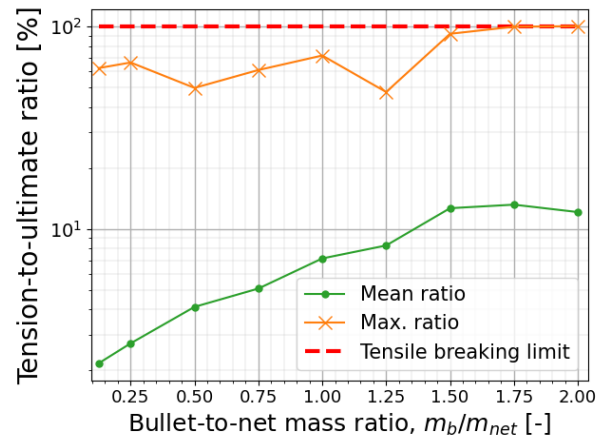
(d) Maximum and mean tension to ultimate value ratio as a function of bullet-to-net mass ratio.

Figure 8.3: Sensitivity Results on net dynamics as a function of varying bullet mass (with step size $\Delta t = 0.75 \cdot 10^{-4}$ s and total simulation time of 10 s).

First, an overview of the trends can be analysed and verified. One can see from both Figure 8.3a and Figure 8.3d, that as m_b/m_{net} increases, (mean) tension and net mouth proper increase, respectively. In fact, as the bullets become more massive, the mean maximum tension felt by the net increases from 2% to 15%, with the minimum net mouth proper increasing from 20% to 27.5% (decreased wrapping capability). With only these two sets of results, it could be assumed that a high bullet mass is undesirable. However, as their mass increase, their maximum velocity decreases (see Figure 8.3c), from a mean value of 32.5 m/s to about 21 m/s (approaching the impact velocity). This decrease and the general lack of trend for the minimum mean velocity suggest the inverse of what was previously mentioned, as a high maximum velocity can lead to a hard impact breaking the solar array or ASAR antenna.

Secondly, it can be seen from both Figure 8.3b and Figure 8.3d, that above $m_b/m_{net} > 1.50$, the net breaks ($T_{max}/T_{ult} > 1$) at the thread location of one bullet. The bullet is thrown into space (see quasi-linear variation of CM in Figure 8.3b after $t = 5$ s) resulting in **1-10 cm-sized secondary debris**.

Lastly, given these results, it is suggested to have the mean maximum and absolute maximum tension ratios below 10% and 50% as a safety requirement to avoid that any internal damage/imperfections result in tensile or lateral breaking. Thus, to allow for optimal capture whilst not breaking the net, the following interval is suggested:

$$0.25 \leq m_b/m_{net} < 1.25. \tag{8.5}$$

Structural risks

The second part of this study is to investigate the effect of changing bullet mass and CM deviation on the structural breaking indicators (τ_{max} and $M_{S_{max}}$) as done in Figure 8.2. The results for the bullet mass and CM deviation can be found in Figure 8.4.
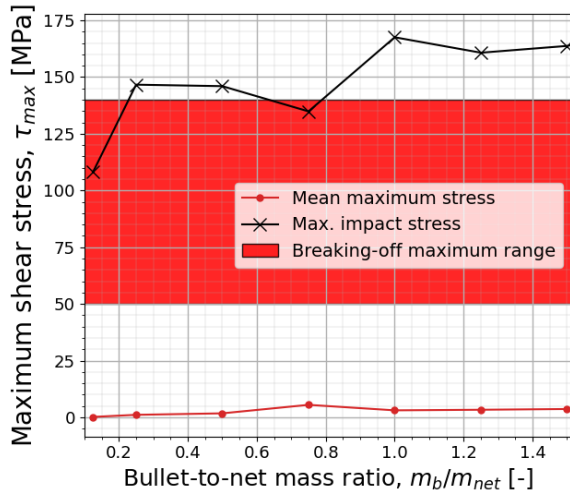
(a) Maximum shear stress at the Ka-band antenna root as a function of the bullet-to-net mass ratio.
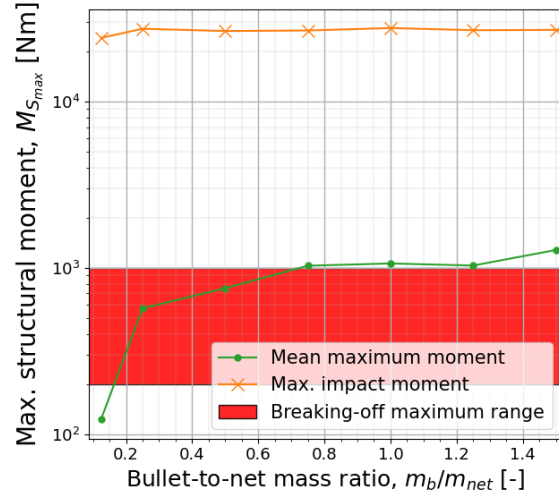
(b) Maximum structural moment at the PIP interface as a function of the bullet-to-net mass ratio.
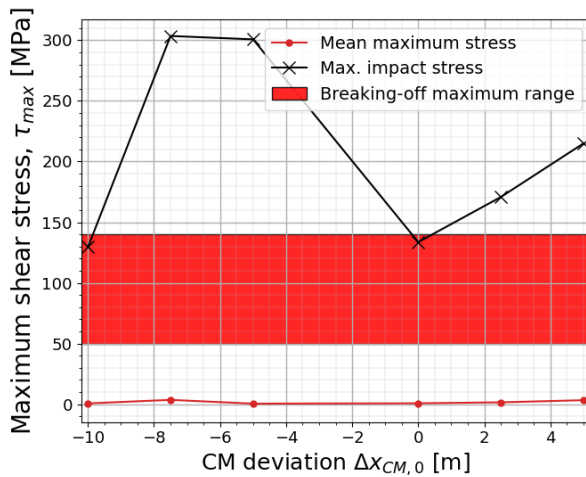
(c) Maximum shear stress at the Ka-band antenna root as a function of CM deviation in x-direction.
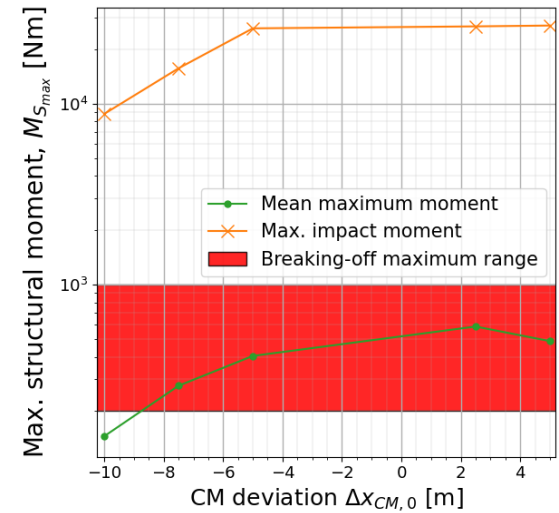
(d) Maximum structural moment at the PIP interface as a function of CM deviation in x-direction.

Figure 8.4: Total Sensitivity Results on breaking indicators as a function of varying bullet mass and CM deviation.

First, with these results one can identify common traits in Figure 8.4b and Figure 8.4d between increasing the bullet mass and translating the net in the positive x-direction, leading to an increase in the mean structural moment experienced by the hinge-panel interface. This is due to the fact that as the bullet mass increases, the transferred increase in momentum is directly applied at the solar array. For $\Delta x_{CM,0}$, as the net is sent towards the solar array (away from the main body), this also increases the experienced loads (Figure 8.4d). The significantly higher maximum shear values of 300 MPa in Figure 8.4c are thought to result from the increased step size used for the sensitivity analysis, compared to the nominal case $\Delta x_{CM,0} = 0$. A final note can be made on the maximum impact moment, which does not vary with m_b/m_{net} (see Figure 8.4b) as the contact force is not dependent on m_b.

Secondly, to further explain the results, the same pattern (with same drop at the nominal value) can be observed for the net tension in Figure 8.5.
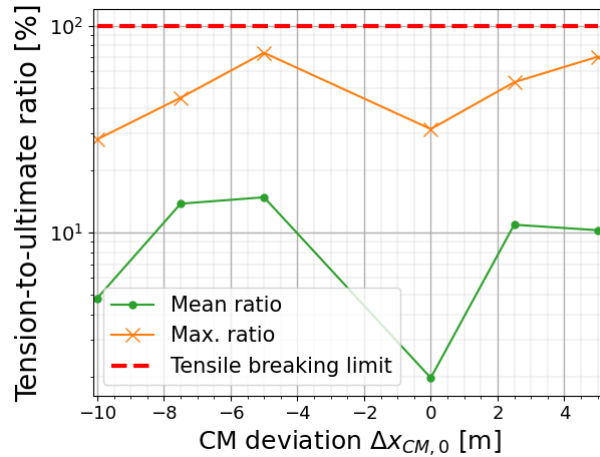
Figure 8.5: Sensitivity result of the maximum and mean tension ratios as a function of the CM deviation.

As the net is sent towards the main body (negative $\Delta x_{CM,0}$), the antenna is directly in contact with the net, leading to higher shear stresses (see Figure 8.4c). This is not the case for $\Delta x_{CM,0} = -10$ m, in which the net is barely able to wrap around the Envisat's solar array leading to a decrease in mean net tension (as observed in Figure 8.5) and thus a decreased stress. Additionally, as the net is sent towards the solar array (positive $\Delta x_{CM,0}$), the maximum shear stress of the antenna increases. An explanation for this is that while $\Delta x_{CM,0}$ increases, the net wraps mostly the panel, decreasing the hub wrapping. As this occurs, the tightening (see Figure 8.5) around the Envisat hub end increases, leading to a higher τ_{max}. Therefore, there is a **direct** relationship between mean tension and the Envisat's stresses.

Dynamical risks

The last and final step is to present briefly the sensitivity, represented as relative dependencies (see methodology in [69]), of the rotation rate and solar array deflection, which can be found in Table 8.2.

Table 8.2: Relative sensitivities for the selected simulation inputs on the object's rotation rate and solar array deflection.

Dynamic parameter	m_b/m_{net}-Sensitivity [%]	$\Delta x_{CM,0}$-Sensitivity [%]
Mean rotation rate	85.46	17.76
Array max. deflection	361.4	-21.58

By analysing the results in Table 8.2, an increase in bullet mass can be seen to be highly detrimental both in creating higher space debris oscillations and leading to fracture of the solar array (with a critical dependency above 100 %). Additionally, a decrease (towards negative values) of $\Delta x_{CM,0}$ can be seen to be advantageous as it decreases the maximum solar array deflection, whilst not increasing highly the space debris rotation rate (see relatively small $\Delta x_{CM,0}$-sensitivity magnitude).

8.4.3. Conclusive mitigation strategies from numerical method

Thus, it can be concluded that changing m_b/m_{net} and $\Delta x_{CM,0}$ leads to different risks. Whereas, it is essential to keep a sufficiently large bullet mass to properly propel the net forward, the same interval as in Equation 8.5 is suggested (due to the low variation in array structural moment above $m_b/m_{net} > 0.75$).

The need to send the net towards the main body is the second result of this analysis. Thus, the solar array is less affected by the net impact loads. Therefore, in order to also limit $T_{max}/T_{ult} < 0.5$ (see Figure 8.5), it is suggested to **only capture the Envisat's main body**, corresponding to a -10 m deviation (or -13.3 m when corrected), and leave the solar array free. However, as high space debris rotation rates can be expected (see Table 8.2), an analysis of the array free vibrations during towing is required to limit the resonance between the tether and the appendage (see Appendix C).

<div align="right">

9

</div>

Model Verification and Validation

9.1. Defining Verification and Validation

There are many definitions of Verification and Validation present in literature and industry. In this Thesis, the focus is on modelling and not specifically on designing a system. Thus, verification focuses on simulation and modelling implementation and if the simulation model(s) used correctly describe the chosen physical models. Within verification one must check if the numerical simulation results are as expected with the known attributes of the associated physical model, e.g., the case of the numerical contact dynamics model which should show a hysterisis loop behaviour. To fully verify all the results, the individual models and their associated interfaces described in section 3.1 will be verified.

Finally, validation is defined in this Thesis as checking if the numerical simulation results actually conform with reality or the physical problem. For this, one might design an experimental test case in order to show that the numerical results are close to reality. One can also use an already widely used validated model to validate the obtained numerical results.

9.2. Verification of Net Dynamics Modelling

In order to verify the numerical results from Chapter 7, first the net deployment dynamics will be checked to see if the **MSD** behaves as expected. Then a simplified test case will be used to verify the contact dynamics model. Lastly, the integration of the shape model and net contact dynamics is checked using three different shapes.

9.2.1. Multi-Spring Damper net dynamics verification

Two different aspects of the tether-net dynamics will be verified. This will start, by verifying the initialisation and entire net deployment dynamics and lastly by identifying that specific net deployment dynamic characteristics are present. The latter also refers to the connection point between the tether and the main net body. Due to the importance of this connection for the towing phase, this interface should be thoroughly verified. Thus, the net dynamics verification process will then end with the checking of the additional tether-net body connection by simply limiting the tether length to a small value.

Verification of correct sequence for deployment dynamics

First, the deployment characteristics of a 20 m $\times$ 20 m net (discretised by 25 side nodes), deployed with velocity $V_e = 30$ m/s and $\theta_e = 45$ deg can be found in Figure 9.1.
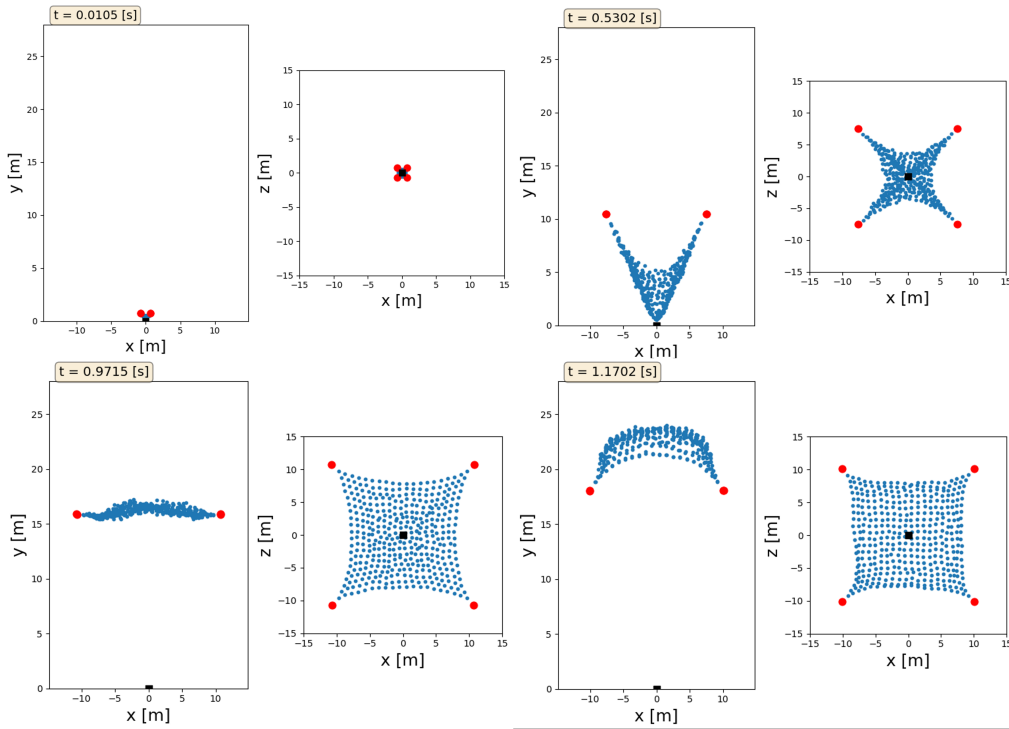
Figure 9.1: Deployment sequence of a 20 m × 20 m net dynamics, discretised with 25 side nodes, a deployment velocity and angle of $V_e = 30$ m/s and $\theta_e = 45$ deg.

With Figure 9.1, the correct behaviour of deployment dynamics and spring-backwards effect associated to the **MSD** modelling can be observed [68]. Lastly, the capture distance (see Equation 4.12) computed analytically to be $d_{capt} = 16.3$ m is confirmed numerically at $t \approx 0.9715$ s, when the net is at its highest deployed area point. Thus, the net internal dynamics verification test is successful.

Tether connection to chaser verification
The final verification is a tether limit test which verifies the tether-net interface in Figure 9.2.
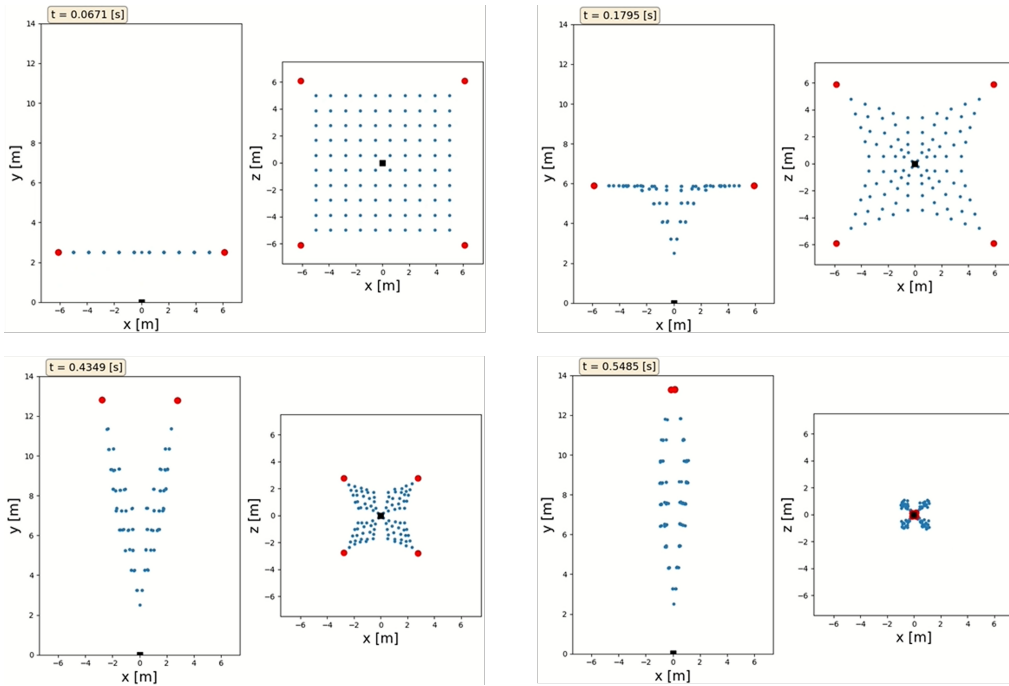
Figure 9.2: Sequence of the 10 m × 10 m net dynamics, discretised with 100 nodes, a frontal velocity $V_{net} = 30$ m/s, a tether length of 2.5 m and a chaser mass of 500 kg.

As can be seen from Figure 9.2, the net simply moves forward until $t = 0.0671$ s, which from that point, it has travelled exactly its tether length. After that, the pulling effect of the tether starts, and the connection point stays fixed to the chaser. Additionally, the chaser (represented in black), seems to not move due to its significantly larger mass of 500 kg compared to the net's total mass of 0.95 kg.

When the chaser mass is artificially reduced to a small value of 0.5 kg, the chaser is found to be propelled forward (travelling a distance of 2 m after 0.4 s). This is in accordance with the conservation of linear momentum, where a velocity change of 57 m/s is expected. Furthermore, the aforementioned means that with a sufficiently massive chaser, no significant errors in the net attitude dynamics are expected to occur. Given these results, the tether connection and coupling to the chaser's dynamics are verified.

9.2.2. Contact dynamics model verification
In order to verify that the contact dynamics provides the correct results, a simplified test case of a falling and bouncing ball can be used.

The verification can be complete if four different aspects are identified: first the height must exponentially decrease after each bounce, secondly the normal force is always positive, thirdly a complete hysterisis loop is present and, lastly, the contact normal force as a function in time is a skewed impulse. The results associated to this simple test case can be shown in Figure 9.3.

(a) Ball (lower) height as a function of time, released from rest at an altitude of $h = 1$ m, with radius 0.1 m and mass of 1 kg.

(b) Normal contact force as a function of time, released from rest at an altitude of $h = 1$ m, with radius 0.1 m and mass of 1 kg.

(c) Hysterisis loops behaviour of contact force from Hunt-Crossley model.

(d) Zoomed behaviour of normal contact force as a function of time, released from rest at an altitude of $h = 1$ m, with radius 0.1 m and mass of 1 kg..

Figure 9.3: Contact dynamics test case: a falling 1 kg-ball with 0.1 m radius from rest with ground constant $\alpha = 0.08$.

First, as can be seen in Figure 9.3a, the altitude of the ball exponentially decreases due to the loss of

energy (the impact is assumed to be inelastic). Secondly, the normal contact force is never negative (see Figure 9.3b) and decreases as the impact velocity decreases. Lastly, the force characteristic hysterisis loop as function of virtual penetration δ and its skewed impulse behaviours are also both present in Figure 9.3c and Figure 9.3d. With the aforementioned results, the contact dynamics model is verified. This test has also been performed successfully during the contact between the net and space debris.

9.3. Verification of Shape Contact Model Integration

Due to the complexity of the Envisat mock-up model which is comprised of multiple cuboids, cylindrical connections and a spherical mock-up antenna, it is essential to verify individually if the net model is able to handle multiple different shapes. Furthermore, space debris have different shapes, making it essential that to verify if the net model can capture all shapes correctly.

9.3.1. Capturing sequence of shapes and composites

The capturing sequence for the cuboid, spherical and cylindrical shapes can be found in Figure 9.4.
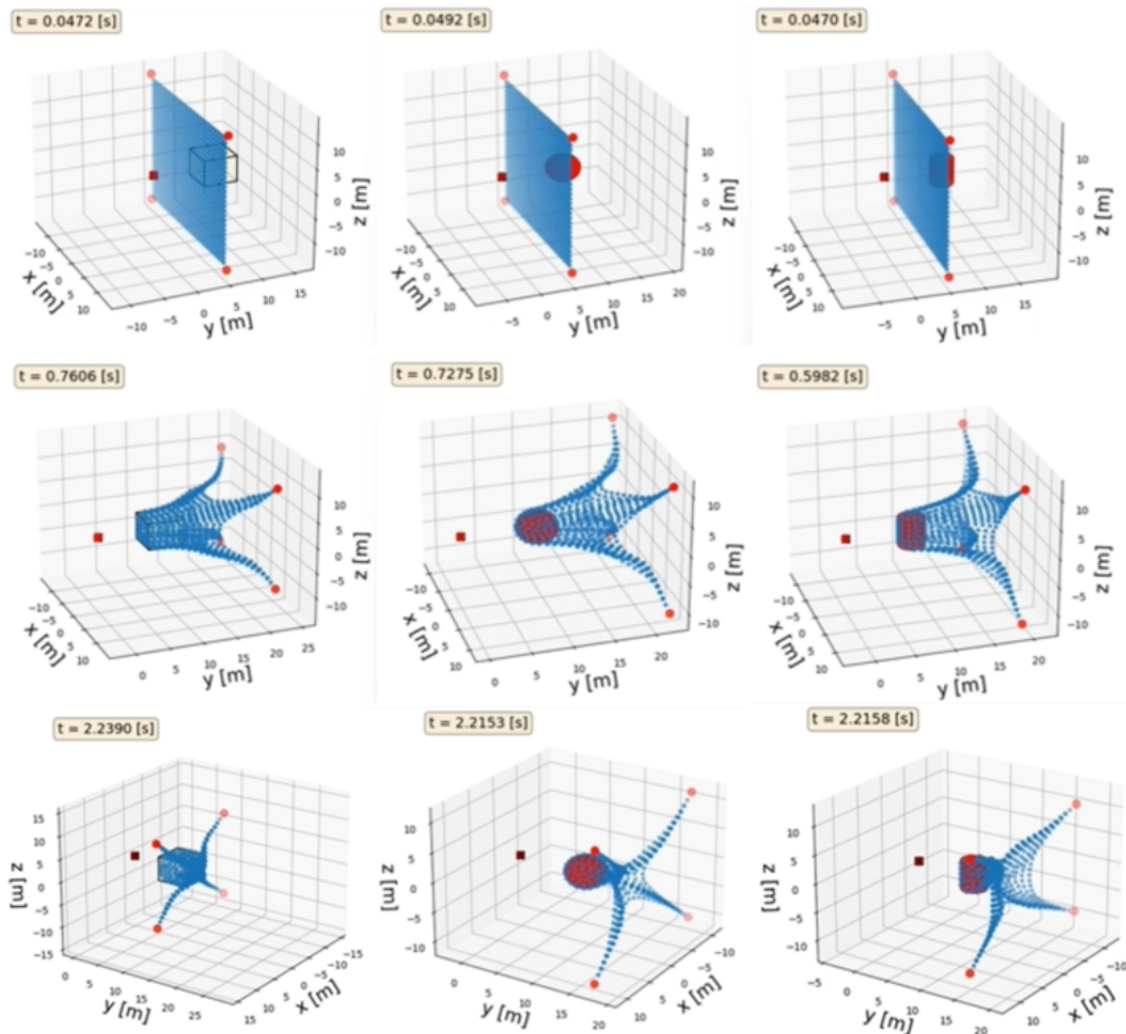
Figure 9.4: Capturing sequence for cuboid (first column), sphere (second column) and cylinder (last column), all with equivalent size (2.6 m) for a 25 m × 25 m net, discretised with 27 side nodes, and a frontal velocity $V_{net} = 25$ m/s.

As can be seen from Figure 9.4, the net model is well integrated with all three of the shape models, contact algorithms and also contact dynamics.

Lastly, as a final step it is essential to see what occurs for a composite cuboid such as a satellite. For this, the Jason layout (Figure 2.4.2) is used and the capture sequence can be found in Figure 9.5.
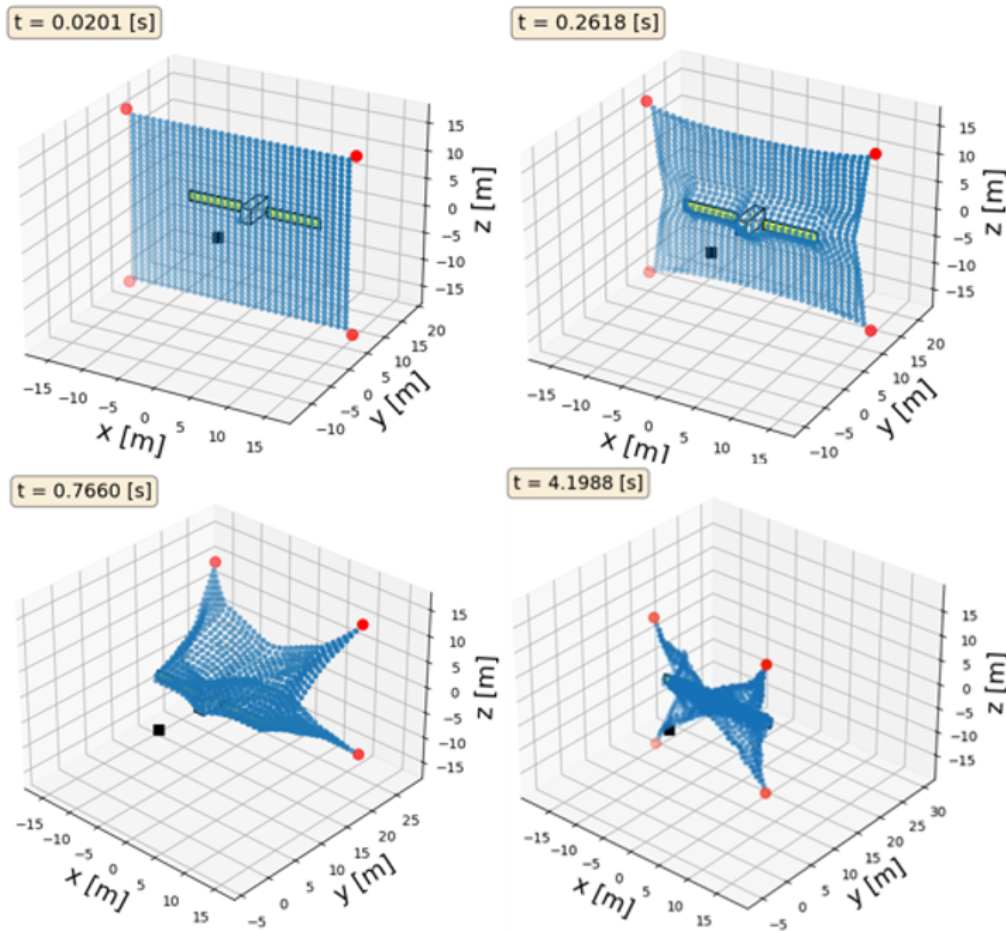
Figure 9.5: Capturing sequence for Jason-type satellite (1 m x 2 m x 3.7 m with 6 m-long arrays) for a 30 m × 30 m net, discretised with 32 side nodes, and a frontal velocity $V_{net} = 25$ m/s.

The net model can be seen in Figure 9.5 to successfully capture a complex shape model with optimal wrapping. However, as a final note, it is essential that the thickness of the solar arrays is set to be around the mesh length l_{0_q} of the net. This is necessary to ensure that the contact algorithm detects correctly the collision with the array's sides. The latter does not affect the realism of the contact loads, as the increased thickness ensures that only one net segment touches the thin structure.

Thus, it can be concluded that the contact detection algorithm, the shape models, and the contact dynamics of the net are behaving as expected and are verified.

9.3.2. Net breaking and shape model verification

The last verification test as part of verifying the combined net deployment and contact dynamics, is to check that given the condition of tensile breaking of the net, the program successfully models net breaking whilst still capturing an object.

To observe net breaking, a 17 m × 17 m net discretised by 21 side nodes is sent towards a cuboid shape with a high impact velocity of 50 m/s and bullet masses of 0.610 kg. ´The results of this verification case can be found in Figure 9.6.

(a) Number of thread tensile breaking events as a function of time for the 50 m/s net impact.

(b) Thread (number 350) tension time series with ultimate tensile force, breaking at $t = 0.315$ s.

t = 0.6415 [s]

t = 0.7261 [s]

(c) Side view visualisation of at least three broken threads at $t = 0.6415$ s.

(d) Final capturing time-shot at $t = 0.7261$ s, showing successful capture with a net area index of 40%.
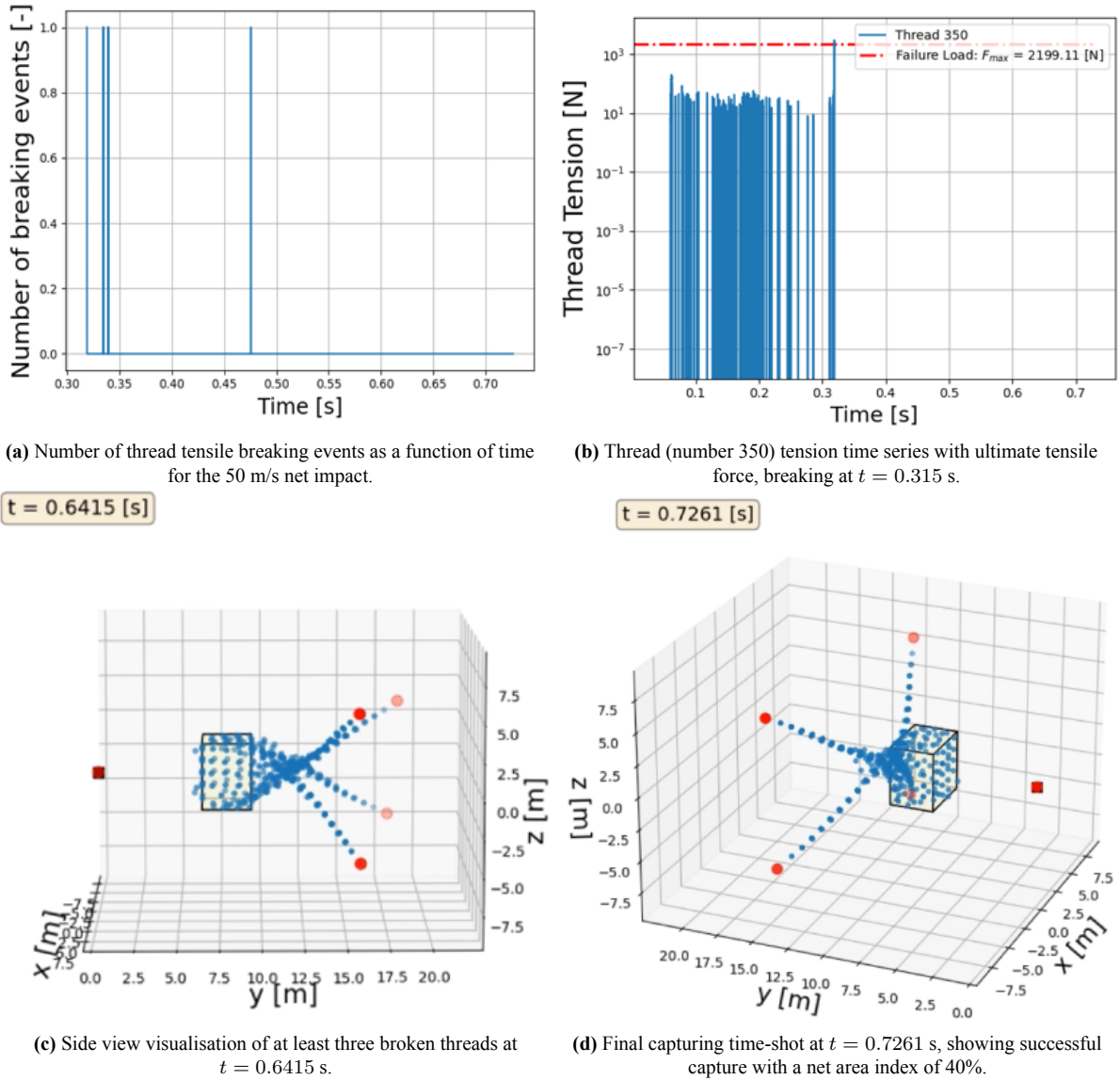
Figure 9.6: Verification results of a 17 m × 17 m net (discretised by 21 side nodes) high impact velocity ($V_{net} = 50$ m/s) with a cuboid (3.9 × 3.25 × 3.9 m).

With this capturing scenario, one can see from Figure 9.6a, that four tensile breaking events have occurred after $t = 0.3$ s, with three being nearly consecutive and the final one at $t = 0.48$ s. The result is confirmed by the time series of one of the breaking threads (number 350) in Figure 9.6b, which after breaking must be set to zero as it is in fact the case. At least, three threads can be seen in Figure 9.6c, showing that a breaking thread with one node does not mean that all other connections should be broken (as the nodes stay connected to the main net body). Even with these four events, which constitute a significant failure for the net structural integrity, a successful capture is still possible, with the contact dynamics, shape and net model interfaces still working.

All four models are hence verified not only individually but their connecting model interfaces have also passed their related verification tests.

9.4. Net Deployment and Contact Dynamics Validation

The validation process will be implemented visually, using an existing deployment and contact dynamics model by Shan Minghe [68], which has been validated through a deployment experiment [76].

9.4.1. Validation inputs and simulation scenario

The validation simulation scenario consists of the capturing of a cube space debris object with a side length of 0.12 m, placed at a capturing distance of 1 m [68]. A secondary simulation has been done for a spherical debris too and can be found in Appendix D. The input parameters for the validation process can be found in Table 9.1 and Table 9.2, with the **RK4** integrator and step size of 10^{-4} s.

Table 9.1: Simulation net dynamics inputs similar to [68].

Input sets	Value (unit)
$(L_{net},\ l_{0_q})$	$(0.48\text{ m},\ 0.08\text{ m})$
$(k_q,\ c_q)$	$(1.094 \cdot 10^3\text{ N/m},\ 0.02\text{ N/(m/s)})$
(V_e, θ_e)	$(1.50\text{ m/s},\ 25\text{ deg})$
m_b	0.05 kg

Table 9.2: Contact detection and dynamics inputs.

Input sets	Value (unit)
(R_q, R_b)	$(0.8\text{ mm},\ 1\text{ cm})$
(μ_s, μ_k)	$(0.1, 0.152)$
(k_n, d_n)	$(1.31 \cdot 10^3\text{ N/m}^{1.5},\ 1.97 \cdot 10^2\text{ N/(m}^{2.5}\text{s}))$
(α, E_i, ν_i)	$(0.1,\ 10^5\text{ Pa},\ 0.3)$

9.4.2. Validation results

The visual comparison of the results can be found in Figure 9.7, with the proposed model in Figure 9.7b and validated model in Figure 9.7a.
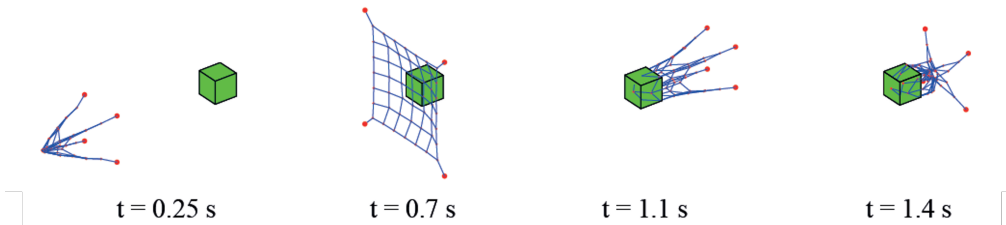
$t = 0.25$ s $\qquad$ $t = 0.7$ s $\qquad$ $t = 1.1$ s $\qquad$ $t = 1.4$ s

(a) Visualisation of net deployment and contact dynamics sequence of a 0.12 m-side length cube debris using the validated model (image retrieved from [68].)
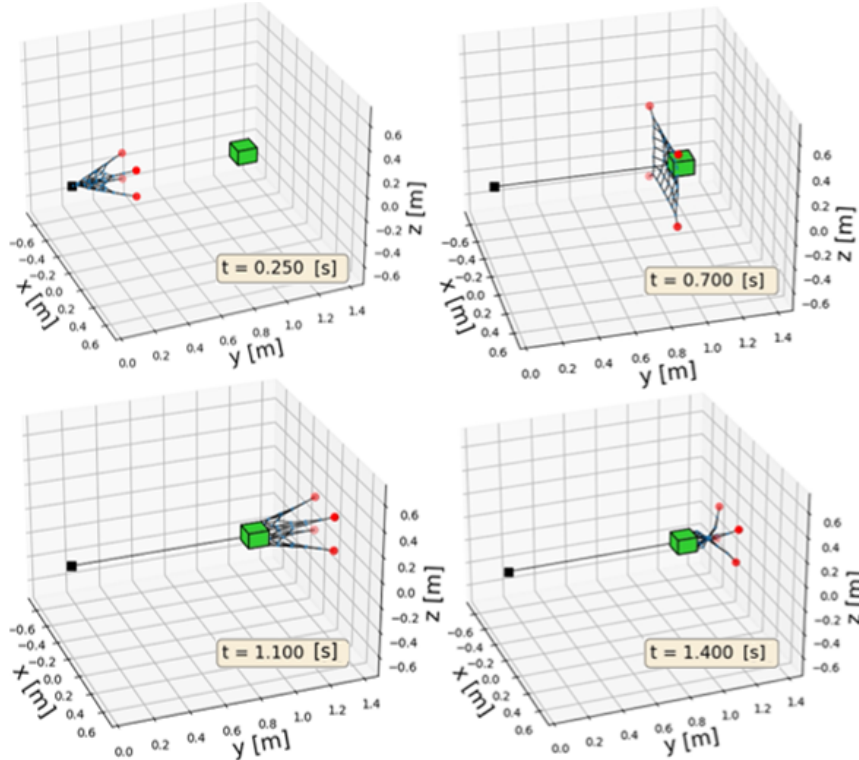
(b) Visualisation of net deployment and contact dynamics sequence of a 0.12 m-side length cube debris (own model).

Figure 9.7: Visual validation comparison results given the simulation scenario (top: validated model, bottom: own model).

First, by comparing Figure 9.7a and Figure 9.7b, one can see that the model is virtually the same, with a minor difference. The latter refers to how the proposed model is found to be slightly ahead in time w.r.t the validated model. Specifically, this can be seen at $t = 1.4$ s, in which the closing is more advanced than the validated model.

An explanation for the aforementioned is thought to be related to the tether stiffness at the net edges. In fact, as explained in [68] and found in the model input file, the edge stiffness of the validated model is set to be higher than for the internal threads. With stiffer edge threads, the flexibility of the net is reduced which is clearly the pattern found in the validated model at $t = 1.4$ s.

The second reason might be related to the contact model itself. The validated model directly implements the contact forces and applies these to the net, whereas the proposed model uses a hybrid model that imposes kinematic constraints obtained through integrating the penetration EoMs (see section 5.2).

Lastly, the initial conditions of the net state is not the same. For the validated model, the net is packed in a specific folding sequence (see [68]), whereas the proposed model is simpler by simply reducing the net size by a factor η_{net}. Even though this difference exists, the overall behaviour is nearly identical and any combination of the three major differences in the model are still justified.

Given the success the visualisation part of the validation process, a secondary result related to the bullet displacement as a function of time will be used to confirm the validity of the model. The bullet displacements can be found in Figure 9.8.
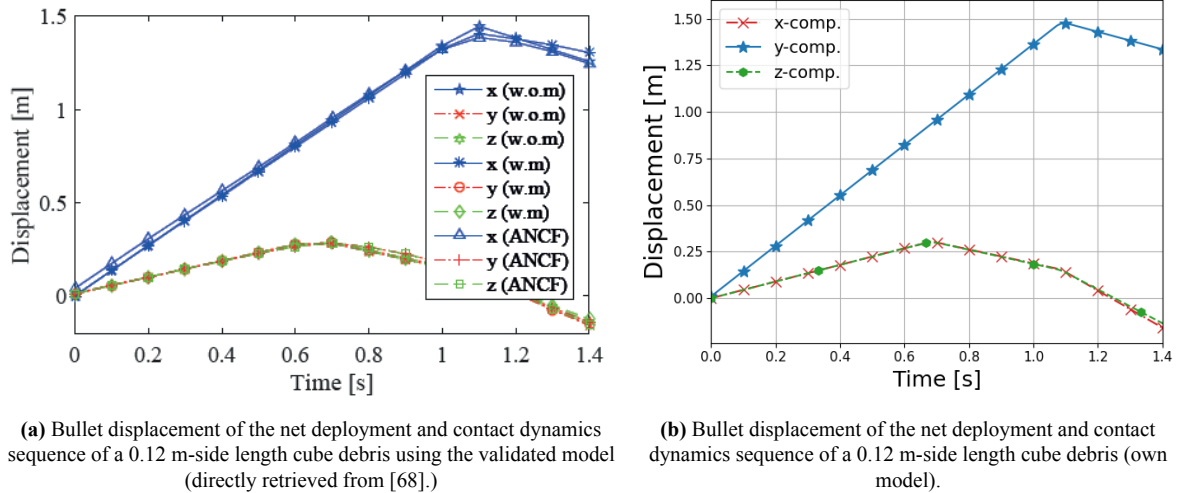
(a) Bullet displacement of the net deployment and contact dynamics sequence of a 0.12 m-side length cube debris using the validated model (directly retrieved from [68].)

(b) Bullet displacement of the net deployment and contact dynamics sequence of a 0.12 m-side length cube debris (own model).

Figure 9.8: Visual validation comparison results given the simulation scenario (left: validated model, right: own model).

To finally validate the net MSD and contact dynamics, a comparison between the validated (see the "w.o.m" case of Figure 9.8a) and own model (Figure 9.8b) bullet displacements, shows that the linear trends and values for the y-direction (x-direction for the validated model) are the same. Furthermore, the two other axis displacements are also very similar in trend and values.

The aforementioned difference between the two models is again confirmed with these results. As it can be seen, the slopes of the $x-$ and $z-$ displacements change at $t \approx 0.7$ s for the validated model (see Figure 9.8a), compared to $t = 0.67$ s (see Figure 9.8b). This confirms the delay argument, with the difference being the edge thread stiffness. Given this and the additional test for a spherical debris in Appendix D, the net deployment and contact dynamics model has been validated.

9.5. Spacecraft Dynamics Verification

The final step in the verification process of the capturing net-spacecraft dynamics modelling is to independently verify the spacecraft dynamics model. This can be done in a two-step process: first the magnitude of the input contact forces needs to be verified, and secondly the dynamic model of the space-

craft (translational and rotational) will be checked by applying known inputs and verifying if expected outputs are observed.

9.5.1. Contact loads verification

In order to verify that the magnitude of the forces is correct, one can compute the total impulse on the spacecraft and compare it to the maximum ΔV obtained using the principle of impulse and momentum conservation.

From the specific case with $V_{net} = 20$ m/s and m_{net} = 12.7 kg, the maximum allowable forward ΔV is computed using:

$$\Delta V = \frac{m_{net} \cdot V_{net}}{m_{SC} + m_{net}}, \tag{9.1}$$

which results in $\Delta V = 0.032$ m/s.

The total impulse, $\boldsymbol{I}_{tot}$, experienced by the spacecraft during contact and wrapping (of t_f duration) is calculated using:

$$\boldsymbol{I}_{tot} = \int_0^{t_f} \boldsymbol{F}_c \, \mathrm{d}t, \tag{9.2}$$

resulting in a magnitude of 203.9 Ns. The latter can be translated into a velocity impulse by dividing it by the spacecraft mass resulting in a velocity increment of 0.026 m/s. Thus, the actual magnitude is lower than the allowable value.

The latter means that the maximum magnitude of the forces does not violate the principle of impulse and momentum conservation as it results in a lower impulse. Secondly, this observed difference of around 6 mm/s is due to the wrapping process in which the direction of the bullets changes from the "forwards" to "backwards" directions resulting in a "negative" ΔV. It can be concluded that the contact forces themselves can be assumed to be realistic and valid.

9.5.2. Input-output model verification

With the contact loads verified, it is now important to perform an input-output verification test of the spacecraft dynamics model. For this, a load in the y-direction will be applied on the spacecraft. The satellite's single rigid-body reaction both in translational and rotational dynamics will be compared to analytical equations. Lastly, the solar array vibrations will be added leading to additional terms in the EoMs of the main body.

Single-rigid body dynamics verification

A constant force with a magnitude of 10 N is applied on the Envisat for 50 s at a body-relative position $\boldsymbol{r}_{i/CG} = [5, \ 0, \ 0]^T$ m. With this type of simplified loading, two (approximate) quadratic analytical relationships associated to the satellite's y-translation and Z-rotation can be used:

$$y(t) = \frac{1}{2} \frac{F_{c_y}}{m_{SC}} t^2 + \dot{y}_0 t + y_0, \tag{9.3}$$

$$\theta_Z(t) = \frac{1}{2} \frac{M_{c_z}}{I_{ZZ}} t^2 + \dot{\theta}_{Z_0} t + \theta_{Z_0}, \tag{9.4}$$

where t is the time and I_{ZZ} is the satellite's MMOI around the Z-axis. Given this, the satellite's translational and rotational reactions can be seen in Figure 9.9.

(a) Input contact force as a function of time in the $\mathcal{L}$-frame (LVLH).

(b) GG perturbation (in $\mathcal{L}$-frame) due to input force in $y-$direction, with $y-$direction quadratic analytical relationship.

(c) Input contact moments as a function of time in the $\mathcal{B}$-frame (body frame).

(d) Euler angular displacements response (in $\mathcal{B}$-frame) due to contact force in $y-$direction, with the associated θ_Z-analytical relationship.

Figure 9.9: Verification results of an applied constant force of 10 N in the $y-$direction ($\mathcal{L}$-frame) at $\boldsymbol{r}_{i/CG} = [5, \ 0, \ 0]^T$, inducing a contact moment and a rotational reaction represented in angular displacements (using the odeint Python integrator, a time step $\Delta t = 0.01$ s and relative and absolute tolerances of 10^{-12}).

First, it can be noted from Figure 9.9a and Figure 9.9c, that due to the fact that two different reference frames are used, F_{c_y} induces not only a $Z-$direction (body-fixed) moment but also generates two other minor moments (due to the body-frame rotation). This is as expected and is also the main reason why one can see from Figure 9.9d that the other two angles (θ_X and θ_Y) also change to a significant extent (mainly linearly as $\boldsymbol{M}_c = \boldsymbol{0}$ after $t = 50$ s). The second reason for their variation is the coupling between the axis that is present from the rotational EoM (see Equation 6.8).

Secondly, the numerical behaviour of the main motions in y- and Z-directions can be seen in Figure 9.9b and Figure 9.9d, to fit very well the predicted analytical relations. In fact, as the contact force is set to 0 (no linear or angular acceleration), the approximate quadratic behaviour becomes an approximate linear behaviour. These two different trends are confirmed by the linear and then constant variation of their respective derivatives, which reach a plateau of 0.0639 m/s and 0.577 deg/s, which can be identified as the respective slopes after $t = 50$ s.

Lastly, from Figure 9.9b, two small displacements in x- and z-directions can be noted, with the x perturbation being more prominent. This can be explained through the translational EoMs themselves (see Equation 6.6), in which only a coupling between the x- and y-directions exists, with the z-direction being an uncoupled a harmonic oscillator. Thus, this coupling and the similar trend for the x- perturbation, explains the observed behaviour.

The spacecraft single-rigid body dynamic model is conclusively verified and the inclusion of the

solar array vibrations can now be added.

Two-body dynamics verification

The addition of the solar array induces an inertial torque $\boldsymbol{M}_{SA,I}$ which leads to a coupled rotational reaction with the satellite. Thus, to verify that the two-body spacecraft dynamics model is correct, the same verification test is used. For this test, three typical trends should be present and identifiable. The additional moment and the satellite's reaction can both be found in Figure 9.10.

(a) Solar array state (θ_s and $\dot{\theta}_s$) reaction from a constant load ($F_{c_y} = 10$ N) and an initial condition ($\theta_{s_0}, \dot{\theta}_{s_0}$) = (2 deg, 0 deg/s).

(b) Induced solar array torque (in $\mathcal{B}$-frame) on the main satellite dynamics as a function of time.

(c) Euler angular displacements response (in $\mathcal{B}$-frame) due to contact force $F_{c_y} = 10$ N and solar array vibration, with the associated θ_Z-analytical relationship.

(d) Space debris rotation rate response (in $\mathcal{B}$-frame) due to contact force in y−direction and solar array vibration.

Figure 9.10: Verification results of an applied constant force of 10 N in the y−direction ($\mathcal{L}$-frame) at $\boldsymbol{r}_{i/CG} = [5, \ 0, \ 0]^T$ on the Envisat dynamics and with added solar vibrations with an initial condition $\theta_{s_0} = 2$ deg (odeint integrator is used with a time step $\Delta t = 0.01$ s and relative and absolute tolerances of 10^{-12}).

First, the solar array can be seen to behave as a simple damped oscillator in Figure 9.10a. This is due to the dominant term $-(\kappa\theta_s + d_\theta\dot{\theta}_s)$ in Equation 6.15. The analytical half-time (not including coupling) is 68.9 s. However, 58 s can be found from Figure 9.10a. This is due to the coupling, which adds a damping term from Equation 6.14. Hence, the solar array motion behaviour is as expected.

Secondly, θ_Y seems to hardly be affected and θ_Z can still be well approximated by Equation 9.4 (all compared to Figure 9.9d). The lack of variation in the Y−direction is expected due to the induced torque magnitude behaviour being highly damped (see Figure 9.10b). Furthermore, both MMOI around the Y− and Z−directions are significantly higher compared to the remaining direction (see Table 7.3).

Thus, for both directions, induced angular accelerations remain small, consequently leading to similar trends observed in Figure 9.9d. The oscillatory behaviour for the rotation rate (Figure 9.10d) is thus only the product of the damped oscillations of the additional induced torque in the Z-direction (Figure 9.10b), as it still can be seen to reach a mean plateau at around $t = 80$ s of 0.57 deg/s (similar to the single-rigid body response).

The final observation is that due to the additional induced torque created by the solar array (see Figure 9.10b), the rotation around the X-axis θ_X and $\dot{\theta}_X$, is highly affected as can be seen in Figure 9.10c and Figure 9.10d. In fact, the coupling with the solar array leads to unstable dynamic behaviour in the $X-$direction as the induced torque increases with the angle's rotation rate as well. This unstable behaviour is expected and has been already identified in literature [36] and is related to the fact that $I_{d_{XX}}$ is one order of magnitude smaller than for the other two directions (see Table 7.3).

In conclusion, all three predictions for the two-body dynamics model were observed confirming that the model is correct and verified.

10

Conclusion and Recommendations

In this chapter, a summary of the results and associated Research Questions answers obtained from all three investigations will be presented in section 10.1. These investigations consisted on a main frontal impact case study, a sensitivity study on the simulation parameters and, lastly, a tertiary study on the towing effects on the space debris object solar panels. This chapter ends by presenting potential recommendations for future work in section 10.2.

10.1. Conclusions associated to Research Questions

Due to the ever growing threat of space debris, a net capturing strategy for ASDR mission has been proposed and analysed throughout the literature. However, what was found to be lacking was the analysis of the effects of net capturing on the space debris itself, specifically related to the risks of generating more space debris.

After analysing the literature, the goal of the Thesis was set and a general theme (**GT**) was defined, focused on what are the **Risks of Secondary Space Debris Generation from Net Capturing in ASDR mission**. To answer this open theme, two main Research Questions (**RQ**) were derived, relating both to the risks themselves and what contributes to the generation of secondary space debris (**RQ1**), and secondly, what preliminary measures can be put in place to mitigate those aforementioned risks (**RQ2**).

Before presenting further the various sub-research questions and their associated answers, it is essential to mention that this work is presented in the form of a preliminary mission design investigation. ESA's largest space debris, the non-operational Envisat satellite, has been selected as the main case study, not only due to its considerable threat and size, but also due to its multiple flexible appendages which were thought to show the highest level of structural breaking risk. Thus, this work started by preliminarily defining and selecting how space debris generation can be defined and which risks are to be prioritised in Chapter 2. Within the same chapter, the Envisat target is selected and is consequently simplified to a mock-up version used for the main investigation simulation scenario. An overview of the modelling strategy for such a multi-disciplinary project was required and was defined in a sequential manner in Chapter 3. All dynamic models followed, from the net MSD deployment and penalty-based method contact dynamics in Chapter 4 and Chapter 5, to the spacecraft single and two-body rigid dynamics and structural modelling in Chapter 6. The first part of the investigation followed using as a main case study the 30 m × 30 m net 20 m/s-impact with an Envisat mock-up (see Chapter 7). Secondly, a two-part sensitivity study was performed to complete the investigation in Chapter 8, with the verification and validation of the results implemented in Chapter 9. Lastly, a tertiary study was focused on the towing phase in Appendix C, in which the simulation was further simplified.

With regards to the Research Questions, several answers and associated conclusions were made.

RQ1) How can the risks of secondary space debris generation for net capturing ASDR missions be modelled?

RQ1.1) How can secondary space debris generation be defined?

- Secondary space debris was specifically defined as the breaking of the satellite sub-structures and the net threads. The unsuccessful capture, due to net slipping or sub-optimal wrapping was considered, but the secondary space debris generation definition is limited to failure, break-off and ejecta.

- Two main sources of risks were identified, relating to the net-tether and space debris systems. For net tether-related risks, tensile breaking during the capturing phase has been found as the main candidate of risk, whereas for the space debris, long flexible appendages breaking due to shear, bending and vibrations were identified.

RQ1.2) Which simulation scenarios and mission phases are adequate to model secondary space debris generation using net capturing?

- The Envisat satellite has been modelled as a composite cuboid mock-up with its main solar array, ASAR and Ka-band antenna dish modelled as a spheroid. The solar array thickness has been artificially increased for contact to be detected. During the capture, the attitude of the Envisat is taken in its A-configuration (see subsection 2.8.2), and initial rotation rate of 1 deg/s.

- A frontal 30 m x 30 m Kevlar 20 m/s net impact is simulated, by modelling the net as a MSD system with equally distributed mass along point masses (called net nodes).

- Contact between the net and Envisat is modelled using Hertzian theory in which the normal force is computed via the non-linear damping model and friction is based on Hollar's model. Due to the limitations of this penalty-based method, the model is re-formulated to a hybrid formulation with kinematic constraints.

- Lastly, the Envisat is modelled first as a single rigid-body and later as a more refined two-rigid body system with a Single-Degree-of-Freedom (SDoF) hinge connecting the solar array to the main body.

RQ1.3) What are the main factors which contribute to the risk increase related to the physical and dynamical interactions between the tether-net, chaser and space debris?

- With regards to the net's structural integrity, the **impacting velocity**, **bullet mass** and **total net size** are considered as potential factors of net breaking. The bullet mass effects were investigated and a sensitivity analysis limited the parameter to 1.25 times the net mass. During verification, the net size was found to result in tensile breaking, if the parameter was not large enough compared to the object size. The deployment velocity of 50 m/s was also a main contributor to net structural breaking.

- Due to the impact velocity of the net, the maximum magnitude of contact forces and moments was found to be 8000 N and 10^5 Nm at impact, later followed by re-occurring ± 1000 N and $\pm 10^4$ Nm loadings.

- The **vibrational motion** of the solar array (for the two-rigid body dynamics), associated to a high **coupling** results in aggravated rotational related risks.

- The Ka-band antenna was found to **not** fail due to **structural vibrations**. However it was observed that due to its **2 m-length** and thin supporting structure, failure can occur when loaded in bending, shear and compression.

- With regards to the impact force magnitude only, the **rotation rate** was concluded to **not be** a factor of structural breaking.

- Finally, as part of the towing modelling (see Appendix C), the **chaser mass**, **tether stiffness** and **propulsion force** were all found to be high contributing factors of a resonance coupling between the solar array and net-tether. Additionally, due to the solar array large geometry, the design space for these parameters was found to be limited.

RQ1.4) **What are the relevant results from RQ1.2 and RQ1.3 that can be used to characterise the generation of space debris?**

- From the main simulation scenario, first related to the net structural integrity itself, no tensile breaking was found. During the wrapping process, however one bullet was found to impact the ASAR antenna (with a 1 kN force) and lead to a momentarily decrease in the net's wrapping capability. However, apart from the latter, an impact velocity of 20 m/s was considered to be safe w.r.t the net's structural integrity alone.

- Given the magnitude of the contact loads from net-satellite contact, and assuming a single rigid-body Envisat model, rotational dynamics were found to be the highest inducing risk indicator of structural breaking, due to the inability of the net to properly damp the rotation rate of the satellite. Thus, this can result in a potential pulley-effect with the chaser [75], which consequently leads to a collision.

- Furthermore, a maximum deflection of 5.2 deg was found for the 16 m-long solar array which could result in a combination of net-solar array breaking.

- From four identified weak locations of failure, all being related to structure interfaces, two were found to be the most critical. These are the solar array-hinge interface (PIP) and the Ka-band antenna dish and supporting beam connection. The first is related to the design being focused only on stiffness and not strength, whereas the second is due to the small thickness of the supporting beams of the antenna. For the second, an excessive shear load of 134 MPa combined with unstable buckling and an uncertainty in its material properties, showed a high likelihood of structural failure.

- Due to bending, shear and buckling failure, two large secondary space debris objects are thought to be generated. The first one is the 5 m x 14.2 m solar panel with ejecta related to the interface connection and the second one is the Ka-band 0.9 m radius antenna dish. Additionally, due to an impact event identified in the main case study investigation, there is a high probability of ejecta being generated due to bullet - ASAR antenna impact.

RQ2) **What preliminary mitigation techniques can be formulated to reduce the risks of secondary space debris generation in ASDR missions using nets?**

RQ2.1) **How sensitive is the risk model w.r.t. the physical and dynamical properties of the interactions between the tether-net, chaser and space debris?**

- From the analytical sensitivity study, a variation of impact velocity from 0.5 to 20 m/s, resulted in the highest variation of contact force (three orders of magnitude), with the second being the net material property α varied from 0.01

to 0.1 (one order of magnitude) and the deployment angle, third, varied from 15 to 65 deg (less than one order of magnitude).

- The numerical study showed that the bullet-to-net-mass ratio (m_b/m_{net}) and the lateral deviation in initial position ($\Delta x_{CM,0}$), yield different results of the structural breaking indicators. The first, results in a general increase of the maximum and mean tension values by 25% and 15% respectively. The antenna maximum shear and mean solar array moment also have been found to increase by 50 MPa and 900 Nm. In terms of $\Delta x_{CM,0}$, a variation of ±100 MPa and 500 Nm were found for these indicators.

RQ2.2) Which mitigation techniques could be used to reduce the risks?

- First, the net size (L_{net}) should be increased to limit the likelihood and intensity of a bullet-ASAR antenna impact.

- As a result from the analytical and numerical sensitivity studies, a maximum impact velocity of 2.0 m/s is allowed, with a maximum bullet mass, resulting in the following design space for the deployment velocity, angle and bullet mass:

$$\frac{4\,m_b}{(m_{net} + 4\,m_b)} \cdot V_e \cdot \cos(\theta_e) \le 2.0 \text{ m/s, for } 0.25 \le \frac{m_b}{m_{net}} \le 1.25.$$

- The second result of the numerical sensitivity study showed that the lateral deviation of the net initial condition should be mainly focused on the main Envisat body. The latter can be translated to a (corrected) value of -13.3 m.

- Finally, having performed a sensitivity analysis on the towing model (see Appendix C), a tether design has been completed. This resulted in a chaser mass of 850 kg, a propulsion force of 440 N (bi-propellant) and lastly, a tether stiffness of 3622.7 N/m (constraining the tether diameter and length).

What can be deduced as a major conclusion and innovation from this Thesis, is that net capturing is **riskier** than originally assumed throughout the literature. With the simplifications and assumptions made in this investigation, it is suggested to further investigate these findings by verifying and validating these results.

10.2. Recommendations for Future Work

The recommendations for future work can be divided into three major parts: net dynamics modelling, overall dynamic modelling strategy and lastly the structural modelling.

10.2.1. Net modelling improvements

The first set of recommendations are related to the assumptions made when modelling the net itself, both in terms of flexibility and contact dynamics.

Flexibility modelling improvements

The net mesh size has been found to be very limiting when modelling the contact between the net and thin structures such as the Envisat solar array. Thus, it is recommended to improve the so-called flexibility modelling of the Multi-Spring Damper (MSD) model in three possible manners. One can first add intermediary nodes which would be the first step in modelling lateral effects on net threads as done in [68]. The second possibility is to add directly lateral modelling by using, similar to the first option, intermediary net nodes, but also by adding to the net stiffness a lateral component as done in [15]. This would also ensure that the proper net tension values would be computed, which is not the case now, and could provide more certainty in modelling the net structural integrity. The final possibility could be

to reject the MSD model itself, and implement the Absolute Nodal Coordinates Formulation or ANCF model implemented in [68]. Whereas, this model was found to be considerably more computationally expensive [70] compared to the improved MSD model, it has been found to be more realistic using a net deployment experiment [76], both in terms of deployment and contact dynamics.

Contact dynamics formulation recommendations

The net modelling can also be improved by formulating a robust contact dynamics model. As it was found in section 5.2, the penalty-based method is highly unstable and provides different results with minor changes in initial conditions and allowable maximum penetrations. It is thus recommended to apply the impulse-based momentum formulation found in [68], from which the impulse would then be translated into loads by using numerical differentiation. Whereas, with the ANCF method, this is also more computationally expensive, the model is more robust and shows a less stiff set of differential equations.

10.2.2. Overall strategy for dynamics modelling recommendations

As presented in section 3.2, the modelling strategy is sequential in order to lower the modelling complexity of moving and rotating space debris contact detection and dynamics. Whereas this assumption is still thought to be valid due to the fact that the Envisat satellite is much larger and massive compared to the capturing net (by two to three orders of magnitude), the additional component of dynamic motion of the so-called shape wall model could result in slightly lower contact forces and moments. As these are fundamental in understanding if secondary space debris is generated, it is recommended to directly integrate the dynamics of the space debris system and verify the validity of the assumption.

It is lastly recommended to include an analysis of the effect of deployment, capture and de-tumbling on the chaser, by modelling the latter as a rigid-body. Furthermore, this would also entail in formulating a more realistic and 3-dimensional towing model, in which the chaser dynamics are also extended to a 6 DoFs system of equations.

10.2.3. Improvements required for structural modelling

The final set of recommendations is related to the structural modelling of stresses induced by the net and spacecraft contact dynamics. In this Thesis work, any structure was assumed to be a 1-dimensional Bernoulli-Euler beam with the rigidly attached boundary condition. With the latter, analytical equations could be used to translate structural forces and moments into normal and shear stresses. However, as for typical spacecraft structures, these assumptions can be be seen as unrealistic. Therefore, it is recommended to perform two different types of advanced analysis.

First, the analytical relationships should be replaced with a more advanced structural Finite Elements Method (FEM) or using the ANSYS software. This would ensure that the computed stresses, at the identified weak locations, can in fact result in structural failure for the nominal case and could yield a more accurate design space for the net impact velocity and bullet mass.

Lastly, as it was recognised at the very beginning of this investigation and during the nominal case scenario, it is suggested to perform a numerical impact-inducing fracture analysis. This is due to the fact that there is a high probability of bullet-structure impact which could result in fracture (and thus secondary space debris) for thin or fragile structures (or surfaces) such as the solar array or smaller instruments on board of the Envisat.

References

[1] Gasser Abdelal and Mohamed Kassab. "Design, Analysis, and Reliability of Solar Panel Rotation Mechanism for Microsatellite". In: *International Conference on Aerospace Sciences and Aviation Technology* 11 (ASAT CONFERENCE May 2011), pp. 1–21. DOI: `10.21608/asat.2011.27158`.

[2] Cody Allard, Hanspeter Schaub, and Scott Piggott. "General hinged rigid-body dynamics approximating first-order spacecraft solar panel flexing". In: *Journal of Spacecraft and Rockets* 55 (5 Aug. 2018), pp. 1290–1298. ISSN: 15336794. DOI: `10.2514/1.A34125`. URL: `https://arc.aiaa.org/doi/10.2514/1.A34125`.

[3] *ASAR Overview - Envisat Instruments*. URL: `https://earth.esa.int/eogateway/instruments/asar/description`.

[4] E. Askar et al. "Improvement of Passive Vibration Damping of Satellite Solar Array Using Adaptive Boundary Conditions". In: *Aerospace Sciences & Aviation Technology* (2017). DOI: `10.21608/asat.2017.22449`.

[5] Vladimir S. Aslanov and Vadim V. Yudintsev. "Behavior of tethered debris with flexible appendages". In: *Acta Astronautica* 104.1 (Aug. 2014), pp. 91–98. ISSN: 00945765. DOI: `10.1016/J.ACTAASTRO.2014.07.028`.

[6] Vladimir S. Aslanov and Vadim V. Yudintsev. "Dynamics, analytical solutions and choice of parameters for towed space debris with flexible appendages". In: *Advances in Space Research* 55.2 (Jan. 2015), pp. 660–667. ISSN: 18791948. DOI: `10.1016/j.asr.2014.10.034`.

[7] Umberto Battista et al. "Design of Net Ejector for Space Debris Capturing". In: *7th European Conference on Space Debris*. Ed. by Ed. T. Flohrer and Schmitz F. ESA Space Debris Office, Apr. 2017. URL: `http://spacedebris2017.sdo.esoc.esa.int`.

[8] Riccardo Benvenuto and Riccardo Carta. "Active Debris Removal System Based on Tethered-Nets: Experimental Results". In: *9th Pegasus-AIAA Aerospace Student Conference*. 2013, pp. 1–11.

[9] Riccardo Benvenuto, Michèle Lavagna, and Samuele Salvi. "Multibody dynamics driving GNC and system design in tethered nets for active debris removal". In: *Advances in Space Research* 58.1 (July 2016), pp. 45–63. ISSN: 0273-1177. DOI: `10.1016/J.ASR.2016.04.015`. URL: `https://ui.adsabs.harvard.edu/abs/2016AdSpR..58...45B/abstract`.

[10] Riccardo Benvenuto, Samuele Salvi, and Michèle Lavagna. "Dynamics analysis and GNC design of flexible systems for space debris active removal". In: *Acta Astronautica* 110 (May 2015), pp. 247–265. ISSN: 0094-5765. DOI: `10.1016/J.ACTAASTRO.2015.01.014`.

[11] M R Bhagat. "Convex Guidance for Envisat Rendez-vous". Delft University of Technology, 2016. URL: `http://resolver.tudelft.nl/uuid:a554505a-21a9-4cc4-8b5e-34da84e1fed8`.

[12] Robin Biesbroek et al. "The e.deorbit CDF Study: A Design Study for the Safe Removal of a Large Space Debris". In: *6th European Conference on Space Debris*. Aug. 2013.

[13] B. Bischof et al. "ROGER - Robotic geostationary orbit restorer". In: *Science and Technology Series* 109 (2005), pp. 183–193. ISSN: 02784017. DOI: `10.2514/6.IAC-03-IAA.5.2.08`. URL: `https://arc.aiaa.org/doi/10.2514/6.IAC-03-IAA.5.2.08`.

[14] Susana Cortés Borgmeyer. *Chemical Bi-Propellant Thruster Family*. URL: `http://www.spa`
      `ce-propulsion.com/`.

[15] Eleonora M Botta. "Deployment and capture dynamics of tether-nets for active space debris
      removal". McGill University, 2018. URL: `https://escholarship.mcgill.ca/concern/`
      `theses/rv042w43j?locale=en`.

[16] Eleonora M. Botta, Inna Sharf, and Arun K. Misra. "Energy and momentum analysis of the
      deployment dynamics of nets in space". In: *Acta Astronautica* 140 (Nov. 2017), pp. 554–564.
      ISSN: 0094-5765. DOI: `10.1016/J.ACTAASTRO.2017.09.003`.

[17] Eleonora M. Botta, Inna Sharf, and Arun K. Misra. "Simulation of tether-nets for capture of
      space debris and small asteroids". In: *Acta Astronautica* 155 (Feb. 2019), pp. 448–461. ISSN:
      0094-5765. DOI: `10.1016/J.ACTAASTRO.2018.07.046`.

[18] M. H. Bredero. *Deployed Wing Mathematical Model Description - Internal Report*. Fokker
      (Airbus), Dutch Space B.V., Sept. 1994.

[19] Marco M. Castronuovon. "Active space debris removal—A preliminary mission analysis and
      design". In: *Acta Astronautica* 69.9-10 (Nov. 2011), pp. 848–859. ISSN: 0094-5765. DOI: `10.`
      `1016/J.ACTAASTRO.2011.04.017`.

[20] A. Chiesa and F. Alberto. "Enabling technologies for active space debris removal : the CADET
      project". In: *Space Safety is No Accident - 7th IAASS Conference*. Ed. by T. Sgobba and I.
      Rongier. Springer, 2014, pp. 29–38. ISBN: 978-3-319-15981-2. DOI: `10.1007/978-3-319-`
      `15982-9_4`.

[21] Nicola Cimmino et al. "Tuning of NASA Standard Breakup Model for Fragmentation Events
      Modelling". In: *Aerospace 2021, Vol. 8, Page 185* 8.7 (July 2021), p. 185. ISSN: 2226-4310.
      DOI: `10.3390/AEROSPACE8070185`. URL: `https://www.mdpi.com/2226-4310/8/7/`
      `185/htm%20https://www.mdpi.com/2226-4310/8/7/185`.

[22] W. H. Clohessy and R. S. Wiltshire. "Terminal Guidance System for Satellite Rendezvous".
      In: *Journal of the Aerospace Sciences* 27 (9 Sept. 1960), pp. 653–658. ISSN: 1936-9999. DOI:
      `10.2514/8.8704`.

[23] Michal Cuadrat-Grzybowski. *Literature Study - Risks from Net Capturing in Active Space De-
      bris Removal Missions*. Delft University of Technology, 2022.

[24] Y-L Desnos et al. *ASAR-Envisat's Advanced Synthetic Aperture Radar Building on ERS Achieve-
      ments towards Future Earth Watch Missions*. ESA, May 2000.

[25] *e.Deorbit Assessment - CDF Study Report - Technical Report CDF-135(C)*. European Space
      Agency, 2012.

[26] *Envisat - Photo Archive*. 1998. URL: `https://www.esa.int/ESA_Multimedia/Keywords/`
      `Description/Envisat/(result_type)/images`.

[27] *Envisat - Space Dutch Technology*. 1998. URL: `https://www.airbusdefenceandspacene`
      `therlands.nl/project/envisat/#`.

[28] *ESA - Mitigating space debris generation*. URL: `https://www.esa.int/Safety_Securit`
      `y/Space_Debris/Mitigating_space_debris_generation` (visited on 07/01/2022).

[29] *ESA's re-entry predictions*. URL: `https://reentry.esoc.esa.int/home/modelling`.

[30] Bo Fang et al. "Nonlinear dynamic modeling and responses of a cable dragged flexible space-
      craft". In: *Journal of the Franklin Institute* 359 (7 May 2022), pp. 3238–3290. ISSN: 0016-0032.
      DOI: `10.1016/J.JFRANKLIN.2022.02.015`.

[31] *Fracture Mechanics | MechaniCalc*. URL: `https://mechanicalc.com/reference/fract`
      `ure-mechanics` (visited on 06/19/2022).

[32] Shuai Gao et al. "Dynamic simulation of fishing net based on cubic B-spline surface". In: *Communications in Computer and Information Science* 325 CCIS (PART 3 2012), pp. 141–148. ISSN: 18650929. DOI: `10.1007/978-3-642-34387-2_17/COVER`. URL: `https://link.springer.com/chapter/10.1007/978-3-642-34387-2_17`.

[33] G. Gilardi and I. Sharf. "Literature survey of contact dynamics modelling". In: *Mechanism and Machine Theory* 37.10 (2002), pp. 1213–1239. ISSN: 0094114X. DOI: `10.1016/S0094-114X(02)00045-9`.

[34] Andrea Gini. "Don Kessler on Envisat and the Kessler Syndrome". In: *Space Safety Magazine* (Apr. 2012). URL: `http://www.spacesafetymagazine.com/2012/04/25/don-kessler-envisat-kessler-syndrome/`.

[35] Werner Goldsmith. *"Impact: the theory and physical behaviour of colliding solids"*. Dover Publications, 2002, p. 379. ISBN: 0486420043.

[36] J.M.G. Habets. "Evolving Systems Approach to the Attitude Control of a Large-Space-Debris Removal Spacecraft". Delft University of Technology, Nov. 2015. URL: `http://resolver.tudelft.nl/uuid:f1bc854a-36f9-4401-a892-2313e4022ea8`.

[37] Toshiya Hanada. "Developing a Low-Velocity Collision Model Based on the Nasa Standard Breakup Model". In: *Space Debris 2000 2:4* 2 (4 June 2000), pp. 233–247. ISSN: 1572-9664. DOI: `10.1023/B:SDEB.0000029903.61467.CD`. URL: `https://link.springer.com/article/10.1023/B:SDEB.0000029903.61467.cd`.

[38] Lisa Hill et al. "The Market for Satellite Cellularization: A historical view of the impact of the satlet morphology on the space industry". In: *AIAA SPACE 2013 Conference and Exposition*. American Institute of Aeronautics and Astronautics (AIAA), Sept. 2013. DOI: `10.2514/6.2013-5486`.

[39] Panfeng Huang et al. "Novel Method of Monocular Real-Time Feature Point Tracking for Tethered Space Robots". In: *Journal of Aerospace Engineering* 27 (6 July 2013), p. 04014039. ISSN: 0893-1321. DOI: `10.1061/(ASCE)AS.1943-5525.0000367`. URL: `https://ascelibrary.org/doi/abs/10.1061/%28ASCE%29AS.1943-5525.0000367`.

[40] Oğuzcan İnal and A. Atas. "Open-hole compressive strength prediction of CFRP composite laminates". In: *Internal Conference on Advances in Applied & Computational Mechanics*. Aug. 2015.

[41] Graham S. Kelly. *"Fundamentals of Mechanical Vibrations"*. Second Edition. New York: McGraw-Hill, 2000. ISBN: 0-07-230092-2.

[42] Donald J. Kessler and Burton G. Cour-Palais. "Collision Frequency of Artificial Satellites: The Creation of a Debris Belt". In: *Journal of Geophysical Research* 83.A6 (1978), pp. 2637–2646. ISSN: 0148-0227. DOI: `10.1029/JA083IA06P02637`.

[43] G. Kirchner and F. Koidl. "Envisat Spin and Attitude Determination Using SLR". In: *Physics* (2014).

[44] Pierre Kœchlin and Sergueï Potapov. "Classification of soft and hard impacts—Application to aircraft crash". In: *Nuclear Engineering and Design* 239 (4 Apr. 2009), pp. 613–618. ISSN: 0029-5493. DOI: `10.1016/J.NUCENGDES.2008.10.016`.

[45] C. G. Koh and Y. Rong. "Dynamic analysis of large displacement cable motion with experimental verification". In: *Journal of Sound and Vibration* 272 (1-2 Apr. 2004), pp. 187–206. ISSN: 0022-460X. DOI: `10.1016/S0022-460X(03)00326-2`.

[46] N. Koshkin et al. "Remote Sensing of the EnviSat and Cbers-2B satellites rotation around the centre of mass by photometry". In: *Advances in Space Research* 58 (3 Aug. 2016), pp. 358–371. ISSN: 0273-1177. DOI: `10.1016/J.ASR.2016.04.024`.

[47] Michelle Lavagna et al. "Debris removal mechanism based on tethered nets". English. In: *International Symposium on Artificial Intelligence, Robotics and Automation in Space (iSAIRAS 2012)*. 2012.

[48] J. C. Liou. "An active debris removal parametric study for LEO environment remediation". In: *Advances in Space Research* 47.11 (June 2011), pp. 1865–1876. ISSN: 0273-1177. DOI: 10.1016/J.ASR.2011.02.003.

[49] Changxi Liu et al. "Improvement on the passive method based on dampers for the vibration control of spacecraft solar panels". In: *Advances in Mechanical Engineering* 14 (3 Mar. 2022). ISSN: 16878140. DOI: 10.1177/16878132221080596. URL: https://journals.sagepub.com/doi/10.1177/16878132221080596.

[50] L. Liu et al. "Deployment dynamics of throw-net for active debris removal." In: *65th International Astronautical Congress*. 2014.

[51] Kalyan K. Mankala and Sunil K. Agrawal. "Dynamic modeling and simulation of satellite tethered systems". In: *Journal of Vibration and Acoustics* 127 (2 2005), pp. 144–156. ISSN: 10489002. DOI: 10.1115/1.1891811.

[52] J. Mas-Albaiges and L. Huertas. *Communicating with the Polar Platform/Envisat - The DRS Terminal*. Nov. 1996. URL: https://www.esa.int/esapub/bulletin/bullet88/masal88.htm.

[53] T. H. G. Megson. *Aircraft Structures for engineering students*. Sixth. Butterworth-Heinemann, 2017. ISBN: 978-0-08-100914-7.

[54] Sayed Abolfazl Mirdehghan. *Fibrous polymeric composites*. Woodhead Publishing, Jan. 2021, pp. 1–58. DOI: 10.1016/B978-0-12-824381-7.00012-3.

[55] *NASA-Canadarm2 and the mobile servicing system*. 2008. URL: https://www.nasa.gov/mission_pages/station/structure/elements/mobile-servicing-system.html.

[56] William J. O'Connor and Deborah J. Hayden. "Detumbling of space debris by a net and elastic tether". In: *Journal of Guidance, Control, and Dynamics* 40.7 (2017), pp. 1829–1836. ISSN: 15333884. DOI: 10.2514/1.G001838.

[57] *Orbital Debris Quarterly News*. Tech. rep. Orbital Debris Program Office, NASA, 2022. URL: https://orbitaldebris.jsc.nasa.gov.

[58] Carmen Pardini and Luciano Anselmo. "Introducing a New Method for Orbital Debris Collision Risk Assessment". In: *International Symposium on Space Dynamics*. June 2000.

[59] Mike Pauken. *Simplified Plume and Aerothermal Heating Analysis for LDSD*. 2012. URL: http://www.nasa.gov/mission_pages/tdm/ldsd/ldsd_overview.html.

[60] Walter D Pilkey. *Formulas for Stress, Strain, and Structural Matrices*. Second. John Wiley & Sons, Inc, 2005. ISBN: 0471032212. URL: www.wiley.com..

[61] *Press Kit | Ocean Surface Topography Mission/ Jason 2 Launch*. June 2008. URL: https://www.jpl.nasa.gov/news/press_kits/jason-2.pdf.

[62] Si yuan Ren et al. "Satellite breakup behaviors and model under the hypervelocity impact and explosion: A review". In: *Defence Technology* (Aug. 2022). ISSN: 2214-9147. DOI: 10.1016/J.DT.2022.08.004.

[63] B. Robin et al. "The e.Deorbit mission: Results of ESA's phase a studies for an active debris removal mission." In: *66th International Astronautical Congress*. 2015.

[64] Mohamed Nasr Saleh et al. "Investigating the Potential of Using Off-Axis 3D Woven Composites in Composite Joints' Applications". In: *Applied Composite Materials* 24 (2 Apr. 2017), pp. 377–396. ISSN: 15734897. DOI: 10.1007/S10443-016-9529-9.

[65] Samuele Salvi. "Flexible devices for active space debris removal: the net simulation tool". Politecnico Di Milano, Dec. 2014. URL: `https://www.politesi.polimi.it/handle/10589/98745`.

[66] Peter B. de Selding. *Envisat To Pose Big Orbital Debris Threat for 150 Years, Experts Say*. July 2010. URL: `https://spacenews.com/envisat-pose-big-orbital-debris-threat-150-years-experts-say/`.

[67] J. Serrano, J. SanMillan, and R. Santiago. "Antenna pointing mechanism for ESA ENVISAT polar platform". In: *30th Aerospace Mechanisms Symposium*. 1996.

[68] Minghe Shan. "Net deployment and contact dynamics of capturing space debris objects". English. PhD thesis. Delft University of Technology, 2018. ISBN: 978-94-6295-985-9. DOI: `10.4233/uuid:803af7c5-4a97-48e9-870b-8e2f6fd325d8`.

[69] Minghe Shan, Jian Guo, and Ebcrhard Gill. "IAC-15-A6.5.7 An analysis of critical deployment parameters for tethered-net capturing for space debris removal". In: *Proceedings of the International Astronautical Congress, IAC* 3 (2015), pp. 2262–2267. ISSN: 00741795.

[70] Minghe Shan, Jian Guo, and Eberhard Gill. "An analysis of the flexibility modeling of a net for space debris removal". In: *Advances in Space Research* 65.3 (Feb. 2020), pp. 1083–1094. ISSN: 18791948. DOI: `10.1016/J.ASR.2019.10.041`.

[71] Minghe Shan, Jian Guo, and Eberhard Gill. "Contact Dynamic Models of Space Debris Capturing Using A Net". In: *Acta Astronautica* (2017). DOI: `10.13009/EUCASS2017-612`.

[72] Minghe Shan, Jian Guo, and Eberhard Gill. "Contact Dynamics on Net Capturing of Tumbling Space Debris". In: *Journal of Guidance, Control, and Dynamics* (2018). DOI: `10.2514/1.G003460`. URL: `www.aiaa.org/randp.`.

[73] Minghe Shan, Jian Guo, and Eberhard Gill. "Deployment dynamics of tethered-net for space debris removal". In: *Acta Astronautica* (2017). DOI: `10.1016/j.actaastro.2017.01.001`. URL: `http://dx.doi.org/10.1016/j.actaastro.2017.01.001`.

[74] Minghe Shan, Jian Guo, and Eberhard Gill. "Review and comparison of active space debris capturing and removal methods". In: *Progress in Aerospace Sciences* 80 (Jan. 2016), pp. 18–32. ISSN: 0376-0421. DOI: `10.1016/J.PAEROSCI.2015.11.001`.

[75] Minghe Shan and Lingling Shi. "Analytical method for net deployment dynamics modeling and its experimental validation". In: *Acta Astronautica* 200 (Nov. 2022), pp. 494–505. ISSN: 0094-5765. DOI: `10.1016/J.ACTAASTRO.2022.08.041`.

[76] Minghe Shan et al. "Validation of Space Net Deployment Modeling Methods Using Parabolic Flight Experiment". In: *Journal of Guidance, Control and Dynamics* (2017). DOI: `10.2514/1.G002761`. URL: `www.aiaa.org/randp.`.

[77] Jiyue Si et al. "Dynamics modeling and simulation of self-collision of tether-net for space debris removal". In: *Advances in Space Research* 64.9 (Nov. 2019), pp. 1675–1687. ISSN: 0273-1177. DOI: `10.1016/J.ASR.2019.08.006`.

[78] Sunayna Singh. "Multibody Approach to Controlled Removal of Large Space Debris with Flexible Appendages". Delft University of Technology, Jan. 2019. URL: `http://resolver.tudelft.nl/uuid:625c408b-97ae-47a5-90c9-493dc4bc0224`.

[79] *Six ways space technologies benefit life on Earth | Briefing papers*. Sept. 2020. URL: `https://www3.weforum.org/docs/WEF_GFC_Six_ways_space_technologies_2020.pdf`.

[80] Svenja Sommer et al. "Temporal Analysis of ENVISAT's Rotational Motion". In: *Journal of the British Interplanetary Society* 70 (2017). Ed. by Holger Krag and Duncan Law-Green, pp. 45–51. ISSN: 0007-084X. URL: `www.bis-space.com`.

[81]   K Stadnyk, K Hovell, and L Brewster. "Space Debris Removal with Sub-Tethered Net: A Feasibility Study and Preliminary Design". In: *8th European Conference on Space Debris*. Apr. 2021. URL: `https://conference.sdo.esoc.esa.int/proceedings/packages`.

[82]   *Stress Intensity Factor Solutions | MechaniCalc*. URL: `https://mechanicalc.com/reference/stress-intensity-factor-solutions` (visited on 06/20/2022).

[83]   *Titanium Ti-6Al-4V - ASM Material Data Sheet*. URL: `https://asm.matweb.com/search/SpecificMaterial.asp?bassnum=mtp641` (visited on 08/01/2023).

[84]   Meggie Vilaranda et al. "Systema-Debris risk assessment tool". In: *8th European Conference on Space Debris*. Ed. by T. Flohrer, S. Lemmens, and F. Schmitz. ESA Space Debris Office, 2021. URL: `https://conference.sdo.esoc.esa.int`.

[85]   B Bastida Virgili, S Lemmens, and H Krag. *Investigation on Envisat attitude motion - e.Deorbit Workshop*. 2014.

[86]   Hongdong Wang and Jianyao Wang. "Dynamics and control of spacecraft solar array deployment considering physical contacts between locking mechanisms". In: *Acta Astronautica* 195 (June 2022), pp. 481–492. ISSN: 00945765. DOI: `10.1016/j.actaastro.2022.03.028`.

[87]   Q. Jane Wang and Dong Zhu. "Hertz Theory: Contact of Spherical Surfaces". In: *Encyclopedia of Tribology*. Springer, Boston, MA, 2013, pp. 1654–1662. DOI: `10.1007/978-0-387-92897-5_492`. URL: `https://link.springer.com/referenceworkentry/10.1007/978-0-387-92897-5_492`.

[88]   D. Whelan et al. "Darpa orbital express program: effecting a revolution in space-based systems." In: *International Symposium on Optical Science and Technology*. 2000, pp. 48–56.

[89]   Jacob Job Wijker. *"Spacecraft Structures"*. 2008. ISBN: 9783540755524. DOI: `10.1007/978-3-540-75553-1`. URL: `https://link.springer.com/book/10.1007/978-3-540-75553-1`.

[90]   Chunbo Wu et al. "Dynamic Simulation and Parameter Analysis of Harpoon Capturing Space Debris". In: *Materials 2022, Vol. 15, Page 8859* 15 (24 Dec. 2022), p. 8859. ISSN: 1996-1944. DOI: `10.3390/MA15248859`. URL: `https://www.mdpi.com/1996-1944/15/24/8859/htm%20https://www.mdpi.com/1996-1944/15/24/8859`.

[91]   LTD WUXI HUAXIN RADAR ENGINEERING CO. *HUAXIN ANTENNA | Products | Vehicle-mounted Antenna*. URL: `https://www.hxantenna.com/products.html?gclid=Cj0KCQjw8qmhBhClARIsANAtboemebFapWZKNhvWtkfQVVgIEzPc5oJNNkh35P2OVpKeAutrS1F3qFEaAu0cEALw_wcB` (visited on 04/03/2023).

[92]   Leping Yang et al. *"Dynamics and Design of Space Nets for Orbital Capture"*. Berlin: Springer-Verlag GmbH, 2017. ISBN: 978-3-662-54062-6.

[93]   Tetsuo Yasaka, Toshiya Hanada, and Hiroshi Hirayama. "Low-Velocity Projectile Impact on Spacecraft". In: *Acta Astronautica* 47 (10 Nov. 2000), pp. 763–770. ISSN: 0094-5765. DOI: `10.1016/S0094-5765(00)00127-2`.

[94]   K. Yoshida and H. Nakanishi. "Impedance matching in capturing a satellite by a space robot." In: *Intelligent Robots and Systems(IROS 2003). IEEE/RSJ International Conference*. 2003, pp. 3059–3064.

[95]   K. Yoshida et al. "Dynamics, control and impedance matching for robotic capture of a noncooperative satellite." In: *Advanced Robotics* (2004).

[96]   Bruce Yost and Sasha Weston. *State of the Art Small Spacecraft Technology Report*. Jan. 2023. URL: `http://www.nasa.gov/smallsat-institute/sst-soa`.

[97] Alan T. Zehnder. *Fracture Mechanics*. Ed. by Friedrich Pfeiffer and Peter Wriggers. Vol. 62. Springer Netherlands, 2012. ISBN: 978-94-007-2594-2. DOI: `10.1007/978-94-007-2595-9`. URL: `http://link.springer.com/10.1007/978-94-007-2595-9`.

[98] Yakun Zhao, Fan Zhang, and Panfeng Huang. "Capture dynamics and control of tethered space net robot for space debris capturing in unideal capture case". In: *Journal of the Franklin Institute* 357 (17 Nov. 2020), pp. 12019–12036. ISSN: 0016-0032. DOI: `10.1016/J.JFRANKLIN.2020.04.037`.

[99] Zhuo Zhuang et al. "Dynamic Crack Propagation". In: *Vestnik Sankt-Peterburgskogo Universiteta. Ser 1. Matematika Mekhanika Astronomiya*. 1. Academic Press, Jan. 2014, pp. 33–50. ISBN: 978-0-12-407717-1. DOI: `10.1016/B978-0-12-407717-1.00003-0`.

[100] Nicholas Zinner et al. "Junk Hunter: Autonomous rendezvous, capture, and De-orbit of orbital debris". In: *AIAA SPACE Conference and Exposition 2011* (2011). DOI: `10.2514/6.2011-7292`. URL: `https://arc.aiaa.org/doi/10.2514/6.2011-7292`.

[101] R. Zwanenburg. "The qualification test programme of the ENVISAT solar array mechanism". In: *Sixth European Space Mechanisms and Tribology Symposium*. Vol. 374. ESA, 1995, p. 65.

<div style="text-align: right; font-size: 4em;">A</div>
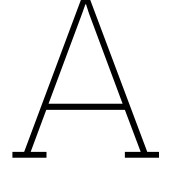
Multi-Body Dynamics of Satellite with Large Solar Array

In this chapter, the necessary matrices and inertial loads of the two-rigid body EoMs (see Chapter 6) will be fully described here.

A.1. Solar Array Dynamic Matrices

The dynamics of the ith solar array depend on the summarising dynamical accelerations $\boldsymbol{a}_{\theta_{s_i}}$, $\boldsymbol{b}_{\theta_{s_i}}$ and $c_{\theta_{s_i}}$ written as [2]:

$$\boldsymbol{a}_{\theta_{s_i}} = -\frac{m_{SA_i} d_i}{(I_{s_{i,2}} + m_{SA_i} d_i^2)} \hat{\boldsymbol{h}}_{i,3}, \tag{A.1}$$

$$\boldsymbol{b}_{\theta_{s_i}} = -\frac{1}{(I_{s_{i,2}} + m_{SA_i} d_i^2)} \left[(I_{s_{i,2}} + m_{SA_i} d_i^2)\hat{\boldsymbol{h}}_{i,2} + m_{SA_i} d_i \boldsymbol{r}_{Hi/B} \times \hat{\boldsymbol{h}}_{i,3} \right], \tag{A.2}$$

$$\begin{aligned} c_{\theta_{s_i}} = \frac{1}{(I_{s_{i,2}} + m_{SA_i} d_i^2)} \Big[&-\kappa_i \theta_{s_i} - d_{\theta_i} \dot{\theta}_{s_i} + \boldsymbol{M}_{ext,Hi} \cdot \hat{\boldsymbol{h}}_{i,2} \\ &+ (I_{s_{i,3}} - I_{s_{i,1}} + m_{SA_i} d_i^2)\omega_{s_{i,3}}\omega_{s_{i,1}} - m_{SA_i} d_i \hat{\boldsymbol{h}}_{i,3} \cdot \big(\boldsymbol{\omega}_{\mathcal{B}/\mathcal{N}} \times (\boldsymbol{\omega}_{\mathcal{B}/\mathcal{N}} \times \boldsymbol{r}_{Hi/B}) \big) \Big], \end{aligned} \tag{A.3}$$

where m_{SA_i}, $I_{s_{i,j}}$ and d_i refer to the ith solar array mass, mass moment of inertia around the jth axis and moment arm respectively. Furthermore, the reaction of the solar array to its motion is described by the linear rotational stiffness and damping κ_i and d_{θ_i} to the external torques $\boldsymbol{M}_{ext,Hi}$ (w.r.t to the ith hinge line H_i). Lastly, the angular rates of the solar array $\omega_{s_{i,j}}$ are the projection of $\boldsymbol{\omega}_{\mathcal{B}/\mathcal{N}}$ w.r.t the ith hinge line axis $\hat{\boldsymbol{h}}_{i,j}$.

A.2. Total System Dynamic Matrices

The full expressions of the dynamic matrices $[\mathbf{A}]$, $[\mathbf{B}]$, $[\mathbf{C}]$ and $[\mathbf{D}]$ can be found below [2]:

$$[\mathbf{A}] = m_{SC}\mathbf{I}_{3x3} + \sum_i^N m_{SA_i} d_i \hat{\boldsymbol{h}}_{i,3} \boldsymbol{a}_{\theta_{s_i}}^T, \tag{A.4}$$

$$[\mathbf{B}] = -m_{SC}\tilde{\mathbf{c}} + \sum_i^N m_{SA_i} d_i \hat{\boldsymbol{h}}_{i,3} \boldsymbol{b}_{\theta_{s_i}}^T, \tag{A.5}$$

$$[\mathbf{C}] = m_{SC}\tilde{\mathbf{c}} + \sum_i^N (I_{s_{i,2}}\hat{\boldsymbol{h}}_{i,2} + m_{SA_i}d_i\boldsymbol{r}_{Sc,i/B} \times \boldsymbol{h}_{i,3})\boldsymbol{a}_{\theta_{s_i}}^T, \tag{A.6}$$

$$[\mathbf{D}] = \mathbf{I}_{SC,B} + \sum_i^N (I_{s_{i,2}}\hat{\boldsymbol{h}}_{i,2} + m_{SA_i}d_i\boldsymbol{r}_{Sc,i/B} \times \boldsymbol{h}_{i,3})\boldsymbol{b}_{\theta_{s_i}}^T, \tag{A.7}$$

where m_{SC} and $\mathbf{I}_{SC,B}$ are the mass and mass moment of inertia (in the $\mathcal{B}$-frame) of the entire spacecraft and $\tilde{\boldsymbol{c}}$ is the skew-matrix representation of the CG vector $\boldsymbol{c}$.

A.3. Total Inertial Loads

The last step in fully defining the system dynamics of the multi-body satellite, is to define the loadings $\dot{\boldsymbol{v}}_{Trans}$ and $\dot{\boldsymbol{v}}_{Rot}$. The first term refers to the total inertial force experienced by the satellite and is expressed as [2]:

$$\dot{\boldsymbol{v}}_{Trans} = m_{SC}\ddot{\boldsymbol{r}}_{C/N} - 2m_{SC} \cdot \boldsymbol{c}' \times \boldsymbol{\omega}_{\mathcal{B}/\mathcal{N}} - m_{SC} \cdot \boldsymbol{\omega}_{\mathcal{B}/\mathcal{N}} \times (\boldsymbol{\omega}_{\mathcal{B}/\mathcal{N}} \times \boldsymbol{c})$$
$$- \sum_i^N \left(m_{SA_i}d_i\dot{\theta}_{s_i}^2\hat{\boldsymbol{h}}_{i,1} + m_{SA_i}d_i c_{\theta_{s_i}}\hat{\boldsymbol{h}}_{i,3} \right), \tag{A.8}$$

where $\boldsymbol{c}'$ is the local time derivative of the CG location $\boldsymbol{c}$.

Given the translational dynamics, the total inertial torque experienced by the system is [2]:

$$\dot{\boldsymbol{v}}_{Rot} = -\sum_i^N \left[(\dot{\theta}_{s_i}\tilde{\boldsymbol{\omega}}_{\mathcal{B}/\mathcal{N}} + c_{\theta_i}\mathbf{I}_{3\times3})(I_{s_{i,2}}\hat{\boldsymbol{h}}_{i,2} + m_{SA_i}d_i\boldsymbol{r}_{Sc,i} \times \hat{\boldsymbol{h}}_{i,3}) + m_{SA_i}d_i\dot{\theta}_{s_i}\boldsymbol{r}_{Sc,i} \times \hat{\boldsymbol{h}}_{i,1} \right]$$
$$- \tilde{\boldsymbol{\omega}}_{\mathcal{B}/\mathcal{N}}\mathbf{I}_{SC,B}\boldsymbol{\omega}_{\mathcal{B}/\mathcal{N}} - \mathbf{I}'_{SC,B}\boldsymbol{\omega}_{\mathcal{B}/\mathcal{N}} + \sum_k^{N_k} \boldsymbol{M}_k, \tag{A.9}$$

with $\sum_k^{N_k} \boldsymbol{M}_k$ being the sum of the external torques on the spacecraft and $\mathbf{I}'_{SC,B}$ is the local time derivative of the spacecraft mass moment of inertia.

B

Envisat Solar Array Layout

Due to the size and complexity of the Envisat solar array, it is essential to have a overview of the structure to be able to identify different points of failure.

The layout can be found in Figure B.1.
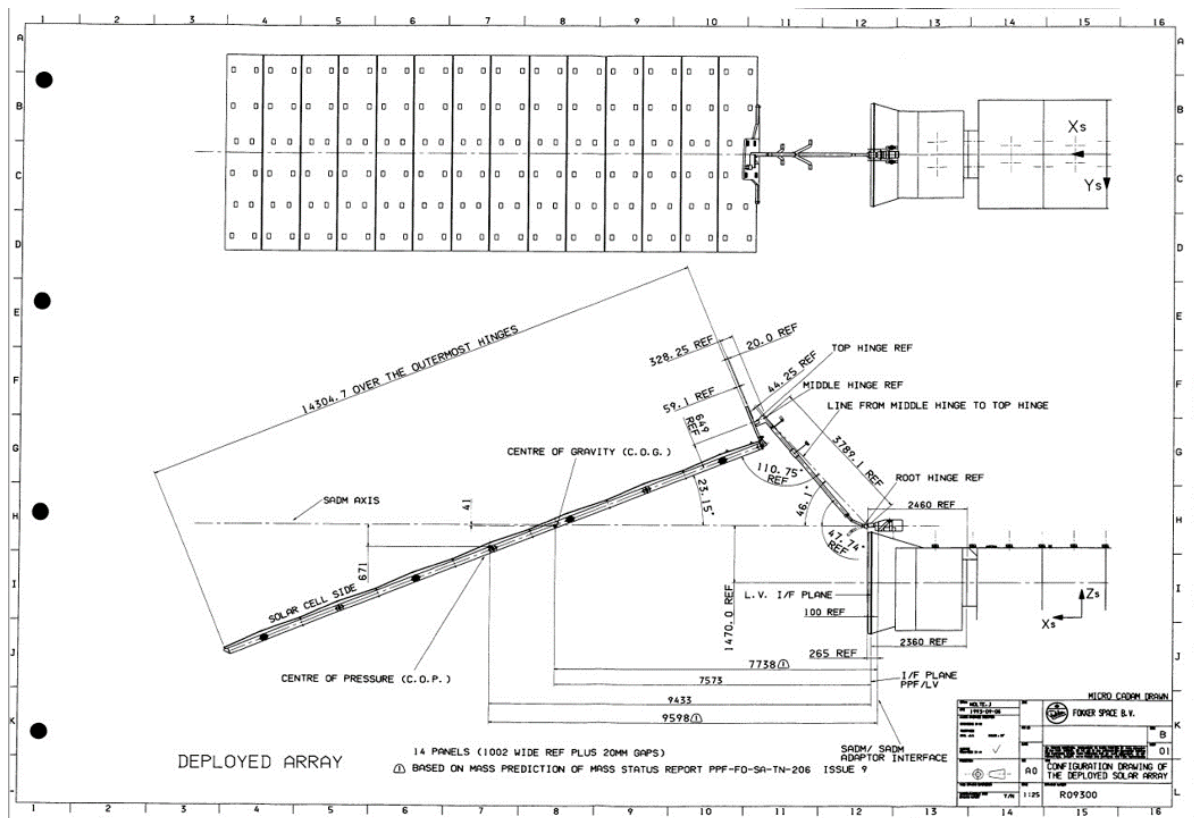
Figure B.1: Envisat solar array technical drawing with relevant dimensions, locations and local coordinate system (courtesy of Airbus, Dutch Space B.V).

C

Tether Design for Safe Towing Dynamics

An independent, but still essential, part of mitigating the risks of secondary space debris generation (and identified in Chapter 6) is the tether design. In this chapter, three important considerations will be presented on how to appropriately design the tether, especially related to the towing phase.

C.1. Limiting Tether Breaking due to Thruster Heating

During the towing phase, the tether pulling the space debris will come in some form of contact with the thruster plumes of the chaser/tug spacecraft. In the case that these plumes create excessive heat, the tether could melt and break at the base. In this section, a simplified and preliminary insight will be made such that no failure or secondary space debris is generated due to the thruster plumes.

C.1.1. Simplified plume model

To have a preliminary idea of the plume size, the plume can be modelled as a cylindrical black body with diameter being the same as the exit thruster diameter d_e and length $l_e = 10 \cdot d_e$ [59].

As found in the previous section, for a 440 N-thruster (which is required as seen in [12] and section C.4), $d_e \sim 0.29$ m [14] and hence $l_e \sim 2.9$ m. This means that there is a 2.9 m region of the tether affected by the thruster plume. This preliminary value is similar to what is obtained in [12] where a maximum heat flux is obtained around 2 m along the tether dimension. For that part of the tether, a thermal reinforcement is required, such as steel. The latter is due to the high melting point of steel (around 1750 K). This steel reinforcement is therefore added at a region of 1 - 3 m.

C.1.2. Heat flux consideration and design options

Within the study made by Biesbroek et al. [12], for a four thruster combination, a maximum heat flux of 0.3 MW/m^2 was found at a distance of 2 m along the tether direction. Even though, the steel reinforcement is placed, this value must be decreased. Three options can be seen as depicted in [12]: (1) place only two thrusters resulting in a maximum heat flux between 0.05-0.1 MW/m^2, (2) place the thrusters with an incident angle around 30 deg or (3) place the thrusters on a different side entirely.

Option (3) is directly rejected as it would add high complexity to the control system during the towing phase with additional torques on the system. Additionally, a thicker region of thermal protection would be required resulting in an added mass. For Option (2), the heat flux is then highly limited but it would result in a high decrease in manoeuvrability which as for the previous option would increase complexity. Lastly, option (1) shows two advantages, as with only two thrusters, Biesbroek et al. found that two burns could be made in order to de-tumble and de-orbit the space debris, compared to the four-thruster option, with the second advantage being a mass reduction. Whereas Biesbroek et al. [12]

decided to implement option (1), due to a reduced manoeuvrability of tilting thrusters, an improved option (1) must be selected. By limiting their separation, Biesbroek et al. predicts a further decrease in heat flux without any significant maneuvrability complications.

C.1.3. Minimum tether diameter

With two thrusters separated by a 50-cm distance a maximum heat flux of around 0.05 MW/m² is expected as obtained in [12]. With this high amount of heat, Zylon is selected out of the typically used four options for net-tethered systems (Kevlar, Vectran, Dyneema and Zylon). This is due to the fact, that it has the highest heat capacity and melting point around 650-780ºC.

To compute the tether properties. the heat flux should first be calculated with:

$$\dot{q} = \rho\, c\, \delta \cdot \frac{dT}{dt},$$ (C.1)

where $\dot{q}$ is the heat flux input, c is the heat capacity, δ the structure thickness (in this case the tether diameter) and dT/dt the temperature gradient w.r.t. time. Thus, the required minimum diameter of the tether, for a 0.05 MW/m² heat flux input is:

$$d_{min} \approx \frac{\dot{q}\,\Delta t_b}{\rho_Z\,\Delta T_{max}\,c_Z},$$ (C.2)

where Δt_b is the burn time (around 250 s [12]), $\Delta T_{max} \approx 650$ K, $\rho_Z = 1550$ kg/m³ and c_Z is the heat capacity of Zylon of 2000 J/kg/K [12]. One can see from Equation C.2, that the Material Index (to be maximised) is M.I. $= \rho\, c\, \Delta T_{max}$ and is found to be the highest for Zylon, confirming its choice. This results in a minimum diameter of 6.2 mm, for the approximate 4 m-region of the tether affected by the plumes. After 4 m, the heat input was found to be negligible [12], and hence to optimise for mass, the tether diameter is set to 2.5 mm for the rest of the tether.

In conclusion, resulting from the initial design process requirement is a minimum localised required diameter thickness of **6.2** mm, needed to resist a maximum temperature change of 650 K for a 4 m-tether region. Lastly, at around 1-3 m, a steel or other form of thermal reinforcement should be placed to provide a sufficiently large heat flux resistance margin and redundancy. The design of the reinforcement will not be analysed in this study due to the complexity of the Zylon-reinforcement interaction during the heating process.

C.2. Limiting Vibrations during Towing Phase

A second risk that can be studied in a preliminary manner, is to limit the vibrational coupling that can occur during the towing phase. This coupling occurs when the tether eigenfrequecny is close or equal to the flexible appendages natural frequencies. If this coupling is not well damped, breaking of the solar panels and other flexible appendages can occur during the towing phase [5, 6, 30].

C.2.1. Simplified towing phase modelling

As presented in the work of Aslanov and Yudintsev [5, 6], specific aspects of the net tether and the chaser can be therefore designed such that vibration coupling is suppressed to a minimum. This can be done by assuming a straight-line towing scenario with constant applied thrust F_t. The tug-boat chaser is assumed to be a point mass. The vibration behaviour of the ith flexible appendage can be computed using the normal-mode expansion method:

$$\eta_i = \sum_{j=1}^{\infty} f_j(\xi_i)q_{ij}(t),$$ (C.3)

where η_i is the lateral beam deflection dependent on ξ_i, the along-beam distance, $f_j(\xi_i)$, the mode shape function and q_{ij}, a modal subset of coordinates for the ith flexible appendage.

For the mode shape function, the beams can be assumed to be fixed-free and can be written as [41]:

$$f_j(\xi_i) = K_j \left[\cosh(\frac{\lambda_j^{1/2}\xi_i}{l_i}) - \cos(\frac{\lambda_j^{1/2}\xi_i}{l_i}) - d_j \left(\sinh(\frac{\lambda_j^{1/2}\xi_i}{l_i}) - \sin(\frac{\lambda_j^{1/2}\xi_i}{l_i}) \right) \right] \qquad \text{(C.4)}$$

where l_i is the undeformed length of the ith flexible appendage, K_j is a constant such that $f_j(l_i) = 1$, λ_j is a non-dimensional frequency (similar to section 6.5) and d_j is a constant obtained as [41]:

$$d_j = \frac{\cos(\lambda_j^{1/2}) + \cosh(\lambda_j^{1/2})}{\sin(\lambda_j^{1/2}) + \sinh(\lambda_j^{1/2})}. \qquad \text{(C.5)}$$

The non-dimensional natural frequencies are the roots of [41]:

$$\cos(\lambda_j^{1/2}) \cdot \cosh(\lambda_j^{1/2}) = -1, \qquad \text{(C.6)}$$

which result in the first five numerical solutions: $\lambda_1 \approx 3.51$, $\lambda_2 \approx 22.03$, $\lambda_3 \approx 61.70$, $\lambda_4 \approx 120.9$ and $\lambda_5 \approx 199.9$.

Given the aforementioned assumptions of straight translational motion, a set of differential equations (Equation C.7) are derived in [6]. These further assumed that the space debris has two identical solar arrays ($q_{11} = q_{12}$) and that only the first shape mode ($j = 1$) is necessary due to its higher order of magnitude in its dynamic influence of the system [6]. With this, the set of equations is the following:

$$\begin{cases} \ddot{q} = c_{qq}q + c_{q\epsilon}\epsilon \\ \ddot{\epsilon} = c_{\epsilon q}q + c_{\epsilon\epsilon}\epsilon + \frac{F_t}{l_t m_c} \end{cases} \qquad \text{(C.7)}$$

where ϵ is the tether strain and the constants c_{qq}, $c_{q\epsilon}$, $c_{\epsilon q}$ and $c_{\epsilon\epsilon}$ can be found derived in [6] and are a function of the space debris, chaser, tether and thrust characteristics.

C.2.2. Investigating tether-solar array resonance

Given the aforementioned simplified dynamics, it is now possible to investigate the severity of the coupling effect between the tether and solar array. This can be visualised in Figure C.1 and Figure C.2.
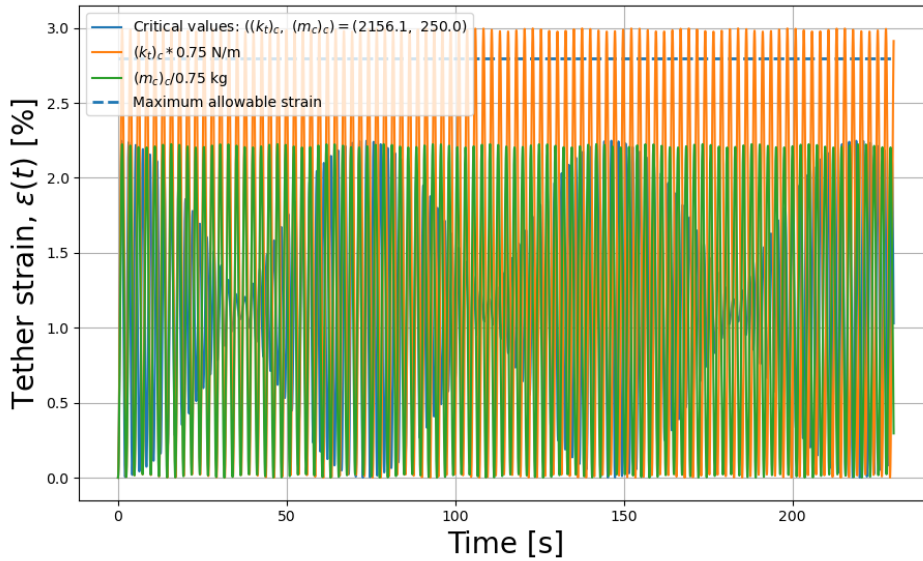
Figure C.1: Tether strain as a function of time for different values of tether stiffness and chaser masses with the visualised resonance phenomenon for $k_t = 2156.1$ N/m and $m_c = 250.0$ kg ($l_t = 20$ m and $F_{th} = 500$ N).
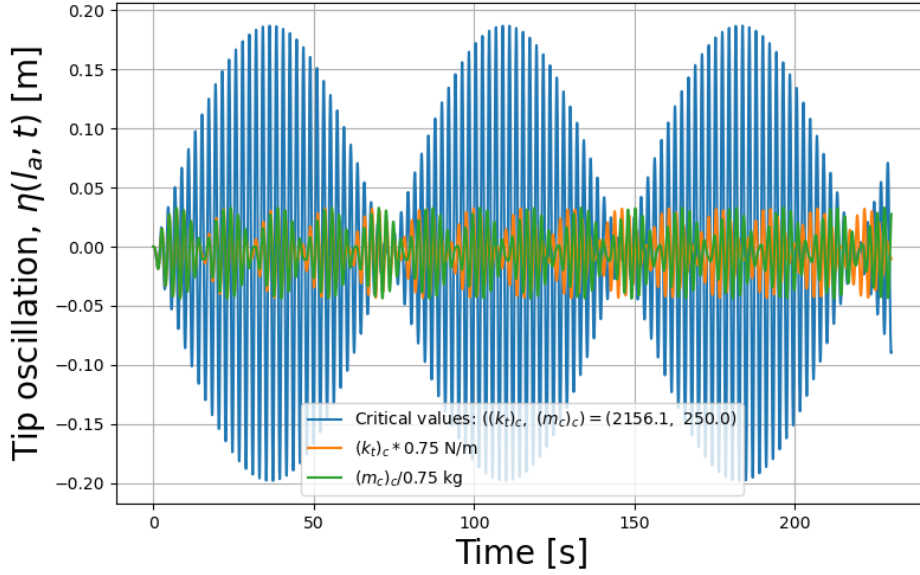
Figure C.2: Tip solar panel oscillation as a function of time for different values of tether stiffness and chaser masses with the visualised resonance phenomenon for $k_t = 2156.1$ N/m and $m_c = 250.0$ kg ($l_t = 20$ m and $F_{th} = 500$ N).

As can be seen from both figures, the resonance phenomenon can lead to tether breaking (see Figure C.1) or/and a highly cyclical and significant increase in the solar panel tip oscillation (see Figure C.2) leading to a structural break-off through fatigue and/or crack propagation of the solar panel. As these two are critical for the mission success and the evaluation if secondary space debris is going to be generated, it is essential to mitigate the latter situation by appropriately designing the tether-net and by selecting an adequate chaser mass.

C.2.3. Dynamic tether design considerations

The particularity of this work is that as the set of equations can be solved analytically, and that an approximate expression for the tether net stiffness k_t and the mass of the chaser, m_c, can be related to the eigenfrequencies and discriminant, D, of the dynamic system. The latter can be written as:

$$D = \frac{1}{4}(c_{qq} - c_{\epsilon\epsilon})^2 + c_{q\epsilon}c_{\epsilon q}. \tag{C.8}$$

In order to avoid the coupling, [6] proposes to avoid the local minima of D. This clearly defined minima of the discriminant can be found analytically in terms of the critical tether stiffness, $(k_t)_c$ which can be found visualised in Figure C.3 and is written as [6]:

$$(k_t)_c = \frac{EI\,m_c[MI_2(M - m_c) - N_f\,\mu_a I_1^2(M + m_c)]I_4}{\mu_a(N_f\,\mu_a I_1^2 - MI_2)^2}, \tag{C.9}$$

where EI is the flexible appendage's flexural rigidity, μ_a and m_a are the flexible appendage linear density and mass and $M = m_d + m_c + N_f m_a$ (with N_f the number of flexible appendages). For the Envisat, only one solar panel is present and hence $N_f = 1$. Finally, I_1, I_2 and I_4 refer to the mode shape integrals [6] which can be computed numerically:

$$I_1 = \int_0^{l_a} f_1(\xi)\,\mathrm{d}\xi, \tag{C.10} \qquad\qquad I_2 = \int_0^{l_a} f_1^2(\xi)\,\mathrm{d}\xi, \tag{C.11}$$

$$I_3 = \int_0^{l_a} \xi f_1(\xi)\,\mathrm{d}\xi, \tag{C.12} \qquad\qquad I_4 = \int_0^{l_a} (f_1''(\xi))^2\,\mathrm{d}\xi. \tag{C.13}$$
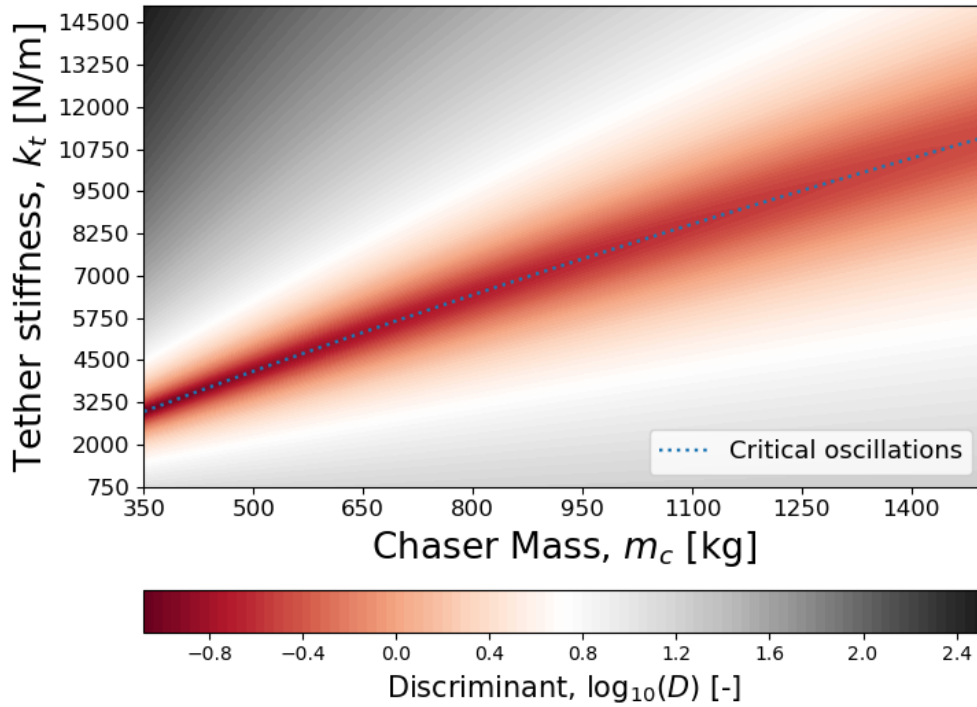
Figure C.3: Colour map of the Discriminant of the dynamic system (Envisat-chaser) as a function of the tether stiffness and chaser mass, with the critical tether-line.

As can be seen in Figure C.3, with an increasing given chaser mass, the critical tether stiffness increases and the exclusion zone (mostly represented in dark red) seems to widen for different chaser masses. Indeed, as the chaser mass increases, the tether stiffness required for the dangerous coupling to occur increases as the tether approaches a solid beam structure. The stiffer the tether becomes, the more the chaser-space debris system becomes rigidly connected. With this, increasing the tether vibrations directly transfer to an increasing of the space debris and hence solar panels vibrations.

Given this explanation, the last step of the tether design process is to choose the optimal combination of tether diameter and length (see Equation 4.5) which follow from Equation C.9, and take into consideration the maximum tip oscillation, η_{max}, and maximum tether strain ϵ_{max}. This will be done via a sensitivity analysis. One must then finally verify with Equation C.8 that the optimal solution is far from the local minimum shown as a red exclusion zone in and Figure C.3.

C.2.4. Towing model sensitivity analysis

Before presenting the sensitivity analysis, a chaser mass should be selected. This can be done by limiting the chaser mass' minimum, taking into consideration the momentum exchange from the net ejection phase. When ejecting the net, the chaser will experience a ΔV which should be as small as possible, taken as 0.1 m/s [12], to reduce the corrective manoeuvres (corrective propellant limited to 50 g) required to compensate for the considerable drift. The minimum mass is thus:

$$(m_c)_{min} = \frac{4m_b V_e \cos(\theta)}{\Delta V_{max}} \tag{C.14}$$

With $\theta = 50$ deg, and assumed high values of ejection velocity $V_e = 25$ m/s and bullet mass $m_b = 1$ kg, one obtains $(m_c)_{min} = 642.8$ kg. This estimate is close to the proposed wet mass of 878 kg by Biesbroek et al. [12]. Thus, a value of 850 kg is set as an independent variable and input to the design process.

To illustrate the effect of k_t and m_c on the maximum tip oscillation of the Envisat solar panel, a sensitivity analysis is performed and can be seen in Figure C.4.
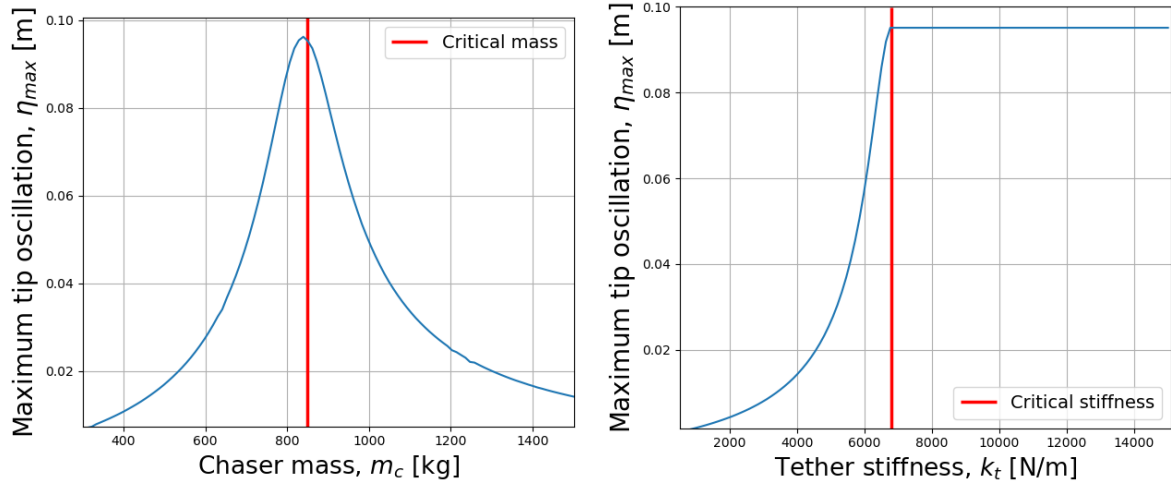
(a) Maximum tip solar panel oscillation as a function of chaser mass for fixed $k_t = 6790.96$ N/m, tether length $l_t = 20$ m and thrust $F_{th} = 500$ N.

(b) Maximum tip solar panel oscillation as a function of tether stiffness for fixed $m_c = 850$ kg, tether length $l_t = 20$ m and thrust $F_{th} = 500$ N.
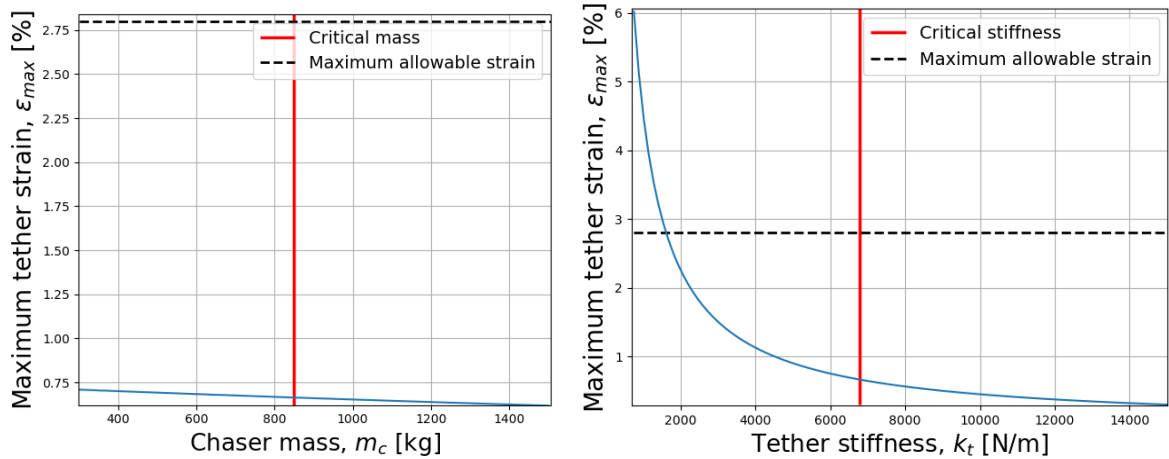
(c) Maximum tether strain elongation ϵ_{max} as a function of chaser mass for fixed $k_t = 6790.96$ N/m, tether length $l_t = 20$ m and thrust $F_{th} = 500$ N.

(d) Maximum tether strain elongation ϵ_{max} as a function of tether stiffness for fixed $m_c = 850$ kg, tether length $l_t = 20$ m and thrust $F_{th} = 500$ N.

Figure C.4: Sensitivity Analysis on Envisat solar array maximum tip oscillation, η_{max}, and tether strain ϵ_{max}, for all inputs.

First, when comparing the effect of the inputs, one can observe that a narrow range of chaser masses (see Figure C.4a) should be avoided and has little effect on the tether strain Figure C.4c. However, η_{max} highly increases near $(k_t)_c$ and reaches a steady plateau for $k_t \geq (k_t)_c$ (see Figure C.4b). The latter is due to the fact that as k_t increases, the tether approaches the behaviour of a solid beam of that length. From the latter, no matter the stiffness, the maximum oscillations cannot be damped due to the fact that the tether strain (see Equation C.7) highly decreases Figure C.4d.

C.2.5. Tether dynamic breaking

Secondly, what has not been covered in the work of Aslanov and Yudintsev [6], is that the tether itself should not break. In fact, the tether stiffness must be higher than 1615 N/m, in order to avoid tether breaking (see Figure C.4d) and the additional creation of space debris. Therefore, the design region for the tether stiffness is limited and linearly dependent on thrust-to-tether-length ratio (see Equation C.7).

The relationship found, for $(k_t)_{min}$, is as follows:

$$(k_t)_{min} = 64.6 \cdot \frac{F_{th}}{l_t}. \tag{C.15}$$

Additionally, as the maximum strain does not vary significantly with chaser mass (see Figure C.4c with a maximum change of 0.1%), the minimum allowable stiffness can therefore be seen as chaser-mass independent and hence Equation C.15 is valid for all chaser masses above 100 kg.

C.3. Tether Breaking at Equilibrium

It is however essential to mention that the tether should also not break in the static condition when the tether tension and thrust are in equilibrium. This can be translated into the following requirement on the stiffness:

$$k_t > (k_t)_{st} = \frac{1}{\epsilon_{ult}} \cdot \frac{F_{th}}{l_t}, \tag{C.16}$$

where ϵ_{ult} is the maximum material elongation of the tether. With all potential material candidates for the tether having an maximum allowable elongation between $2.8 - 3.5\%$, the proportional constant is in the range of $[28.57 - 35.71]$. This range is much lower than the dynamic solution (see Equation C.15), which means that tether breaking at the equilibrium condition is not a driving design requirement.

C.4. Tether Final Design and Summary

Given these three design limits, the thrust can be limited to 440 N [12], such that the re-entry manoeuvre from Envisat's altitude of 772 km to the re-entry orbit of 120 km [29] only consumes 95 kg (assuming a bi-propellant with effective exhaust velocity of 3149 m/s [14]) and can provide sufficient margin for more than two emergency burns of 220 N, in the case of postponement of the total de-orbiting burn [12].

Furthermore, the tether length should be designed such that the net can safely capture the Envisat target at a distance d_{capt} (see Equation 6.2 in section 4.4) and can satisfy all three design requirements of heat flux, dynamic solar panel vibrations and equilibrium conditions. As the largest Envisat dimension is 24.7 m, a 37 to 50 m-large net is required, which would lead to a range of tether lengths dependent on the shooting angle θ. This however would be a harsh minimum as the vibrations condition seems to be driving the design of the tether length as discussed before.

With a proposed tether length of 275 m (near half what is proposed in [12]), $(k_t)_{min} = 1033.6$ N/m and $(k_t)_c = 6790.96$ N/m (which is independent of the tether length). By further understanding that the tether has a 2.5-mm diameter for a length of 271 m, compared to the small 4-m region with a diameter of 6.2 mm, the effective spring constant of the entire cable is assumed to be dominated by the largest length. This is justified mathematically as the tether can be seen as an equivalent system of two springs (k_1 and k_2) in series with equivalent spring constant k_{eq}:

$$k_{eq} = \frac{k_1 \cdot k_2}{k_1 + k_2}, \tag{C.17}$$

where in this case k_1 is found to be of order 10^6 N/m whereas k_2 is only of order 10^3. With these values, k_{eq} is equal approximately to the lowest (and hence longest) spring constant. The effective tether stiffness is thus $k_t = 3622.7$ N/m, which is well between the bounds set above.

Finally, the tether mass would then be: $m_t = \rho_s \cdot (A_{t,1}l_{t,1} + A_{t,2}l_{t,2}) \approx 2.250$ kg, which can be accounted into the total mass of the chaser (~ 0.27 %). Within this 275 m-long tether, 271 m consists of a 2.5 mm Zylon material. Only 4 m of the tether near the thruster area, has a thicker 6.2 mm diameter with steel reinforcement. The tether is thus designed to accommodate both heating flux and to lower solar panel vibrations which could lead to solar array breaking and thus secondary space debris generation.

C.5. Tether Design Verification

To verify the towing model, the same test case as within the work of Aslanov and Yudintsev [5, 6] will be used. The input values are summarised in Table C.1.

Table C.1: Simulation inputs related to tether design model verification [6].

Simulation input	Symbol	Value
Array length	l_a	5.0 m
Array flexural rigidity	EJ	184.0 N/m^2
Array linear density	μ_a	10 kg/m
Tether initial length	l_0	50 m
Target mass	m_d	2800 kg
Mode 1 constant	λ_1	3.516 [-]

Given these inputs, the resonance behaviour with and without critical values can be verified numerically with the plot of the appendages' oscillations in Figure C.5a. Furthermore, the minimum critical stiffness computed analytically to be 178.72 N/m (using Equation C.9) can be compared to the analytical results of the discriminant in Figure C.5b for a chaser mass of 450 kg (as done in [6]).
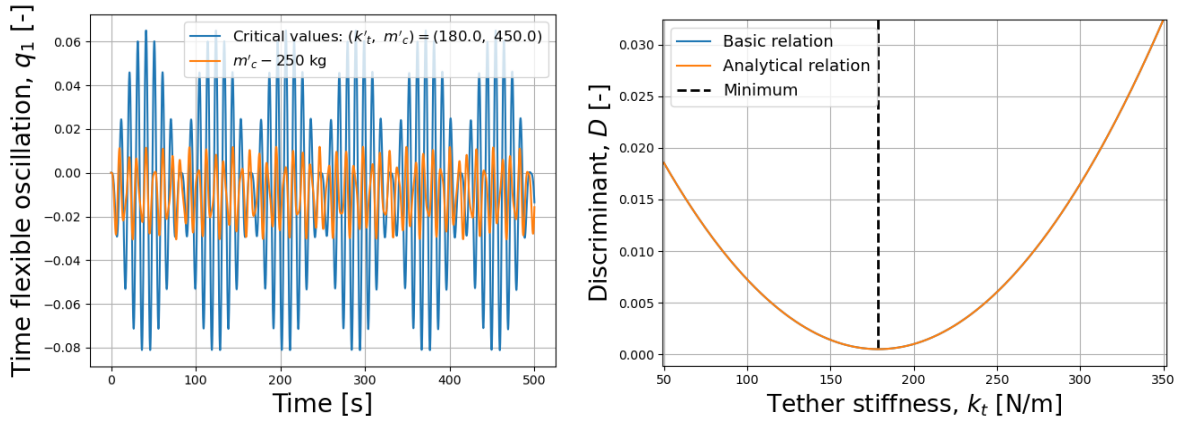
(a) Time oscillation behaviour of flexible appendage as a function of time for critical and non-critical values of tether stiffness and chaser mass.

(b) Discriminant of the dynamic system (target-chaser), computed from analytical and basic relations, as a function of the tether stiffness and for a chaser mass of 450 kg.

Figure C.5: Tether design verification tests figures.

From Figure C.5b, not only it can be observed that the critical stiffness is correct, but also that the general (Equation C.8) and analytical relations of the discriminant overlap exactly. Thus, there is no difference between the two curves, confirming the correct implementation of the method. Lastly, the expected behaviour of resonance at the critical point is confirmed in Figure C.5a with the change of critical mass showing a high decrease in oscillation as the "design point" (see Figure C.3) is away from the critical resonance region. With this, it can be confirmed that the tether-chaser-target dynamic model is verified.

D

Additional Net Deployment and Contact Dynamics Validation

The validation process done in section 9.4, can also be implemented for a spherical space debris of radius 0.08 m with similar input parameters and **RK4** integrator with $\Delta t = 10^{-4}$ s. The visualisation can be found in Figure D.1.

| t = 0.25 s | t = 0.7 s | t = 1.1 s | t = 1.4 s |

(a) Visualisation of net deployment and contact dynamics sequence of a 0.08 m-radius spherical debris using the validated model (image retrieved directly from [68].)

(b) Visualisation of net deployment and contact dynamics sequence of a 0.08 m-radius spherical debris (own model).
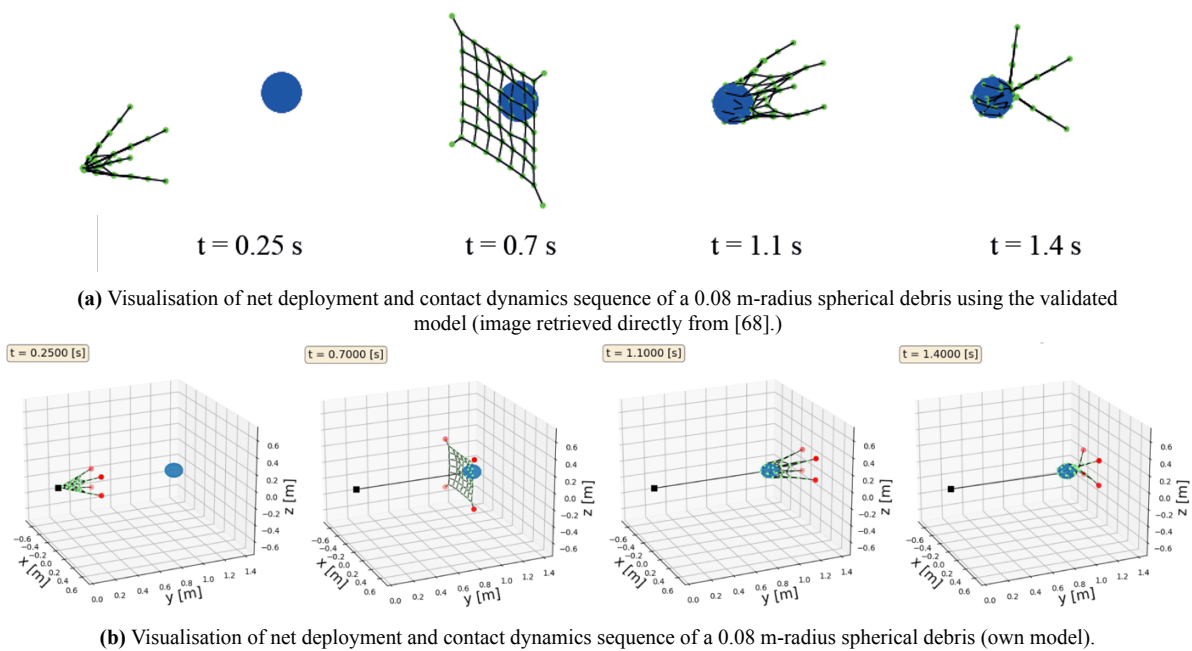
Figure D.1: Visual validation comparison results given the simulation scenario of ball capture (top: validated model, bottom: own model).

As with the cuboid, the spherical debris capture is nearly identical and not only cross-verifies the cube capture results, but also further validates the proposed model.